Graduate Theses and Dissertations

12-2012

Computational Design of the Electrical and Mechanical Performance of Steerable MEMS Antennas

Morgan Andrew Roddy
University of Arkansas, Fayetteville

Computational Design of the Electrical and Mechanical Performance of

Steerable MEMS Antennas

Computational Design of the Electrical and Mechanical Performance of Steerable MEMS Antennas

A thesis submitted in partial fulfillment
of the requirements for the degree of
Master of Science in Microelectronics-Photonics

By

Morgan A Roddy
Rose-Hulman Institute of Technology
Bachelors of Science in Engineering Physics, 2010

December 2012
University of Arkansas

Abstract

This thesis describes the origins, improvements, and variations of a broadband microwave antenna that can be beam-steered by a micro-electromechanical system (MEMS). The steerable MEMS antenna of this work was comprised of a planar antenna on top of a Silicon membrane. The membrane is etched to create a gimbal hinge structure and a platform which supported the antenna and gave it one or two degrees of freedom of rotation. The antennas presented were broadband and fed by a coplanar waveguide (CPW) transmission line which traversed the hinge structure. The antenna's orientation in space was designed to be changed through electrostatic actuation of the antenna platform's hinges.

The goal of this thesis was to improve on the initial design and performance of the prototypic antenna. The best variation of the prototype antenna could rotate ±4.0° in two degrees of freedom under 800 VDC of actuation voltage and had a bandwidth of 1.55. The mechanical and electrical aspects of the device were studied and analyzed concurrently. Three variations of the MEMS antenna platform were design and modeled; Generations 1 – 3 (G1 - G3). The G1 platform was an optimized version of the prototypic MEMS platform. The G2 platform could rotate in two dimensions but had much thinner hinges and a more robust antenna platform. The G3 platform was a one degree of freedom version of the G2 platform. A new antenna shape was selected and optimized for integration with the three generations of antenna platforms; the planar inverted cone antenna (PICA). The G3 platform had the best overall electrical and mechanical performance. Two additional antennas were simulated on the G3 platform; a cylindrical dielectric resonator antenna (C-DRA) and a teardrop dielectric resonator antenna (Td-DRA). The three best antenna variations on the G3 platform were simulated to have maximum actuation

angles ranging from $10 - 13°$ and have bandwidths of 3.62 (PICA), 1.70 (C-DRA), and 1.78 (Td-DRA).

This thesis is approved for recommendation
to the Graduate Council.

Thesis Director:

_____

Dr. Magda El-Shenawee

Thesis Committee:

_____

Dr. Douglas Hutchings

_____

Professor Ken Vickers

The following signatories attest that all software used in this thesis was legally licensed for use by Mr. Morgan A. Roddy for research purposes and publication.

_____   _____
Mr. Morgan A. Roddy, Student   Dr. Magda El-Shenawee, Thesis Director

This thesis was submitted to http://www.turnitin.com for plagiarism review by the TurnItIn company's software. The signatories have examined the report on this thesis that was returned by TurnItIn and attest that, in their opinion, the items highlighted by the software are incidental to common usage and are not plagiarized material.

_____   _____
Professor Ken Vickers, Program Director   Dr. Magda El-Shenawee, Thesis Director

Thesis Duplication Release

I hereby authorize the University of Arkansas Libraries to duplicate this thesis when needed for research and/or scholarship.

Agreed_____

Morgan A Roddy

Refused_____

Morgan A Roddy

Acknowledgements

I would like to acknowledge and thank Dr. El-Shenawee for her support and leadership during my work on this thesis. I would especially like to thank her for helping me accomplish my goals and giving me tools and advice to succeed. I greatly enjoyed working under her direction on this thesis. I greatly respect her work ethic and ability to push me to the extent of my abilities. I have learned an incredible amount from her and am excited to hear about the great work she has yet to be a part of.

I would like to thank Ken Vickers for his mentorship, support, and friendship during my time at the University of Arkansas. His advice and good vibes were always a great encouragement to me through some very difficult years of graduate school. He will always be held in my highest regard.

I must thank Douglas Hutchings for his advice and insight on his previous work. He should be given credit for developing a great idea and doing an outstanding job documenting it in his dissertation. It would have been much more difficult for me if it were not for his attention to detail and hard work. Thanks also go to Ron Foster for his thoughtful insights and good advice on this project. He was an invaluable in resource to me.

Special thanks go to my mates who kept me going when the times got tough. To Cole Deaton, I couldn't have made it without you buddy, hats off to you, good sir. Benjamin del Shreve deserves thanks for being my fellow philosopher and brother. To David Robinson and Trevor Seekamp, I greatly value our friendships.

Thanks go to my family who has supported me through the last nine years of college in every way imaginable. I certainly would have failed without your love and support.

Dedication

This work is dedicated to those who have inspired me and pushed me to achieve more than I ever thought I could as well as encouraged me to stay strong when the going got tough. To my mentors at Olympic College, Dr. Jeff Brown, Linnea Hess, and Karen Hulsebosch, Thank you for instilling good habits of academic professionalism and zest for learning. To Kipp Kraus, thank you for your friendship and wise advice to shoot for the stars; you are a true inspiration. To my mentors at Rose-Hulman who helped me develop my skills as a researcher; Dr. Scott Kirkpatrick, Dr. Elaine Kirkpatrick, Dr. Azad Siahmakoun, Dr. Marijj Syed, and Dr. Charles Joenathan.

Table of Contents

List of Figures

List of Tables

Chapter 1 – Background

This thesis describes in detail the background, optimization, and fabrication of a unique antenna developed at the University of Arkansas by Dr. Douglas Hutchings in Dr. Magda El-Shenawee's Computational Electromagnetics Group; the Steerable MEMS Antenna [1]. Dr. Hutchings developed the antenna to be used for microwave detection of breast cancer and was the focus of his PhD research. The main contributions of this author are design modifications and the optimization of the original design. The design was studied through a combination of closed-form analysis of design parameters as well as numerical simulations of the device's behavior.

The MEMS antennas presented in this thesis are interesting for several reasons. First, the antennas are planar and broadband. This is important for a broad range of possible applications for the antenna. Second, the device can be fabricated using standard micro-fabrication techniques. No new techniques need to be developed to fabricate the antennas. Third, the design utilizes a MEMS platform to support and steer the antenna. The MEMS platform was designed to be micro-machined into Silicon with a monolithic hinge structure to enable rotation of the antenna in two dimensions and is shown in Figure 1.1.1.
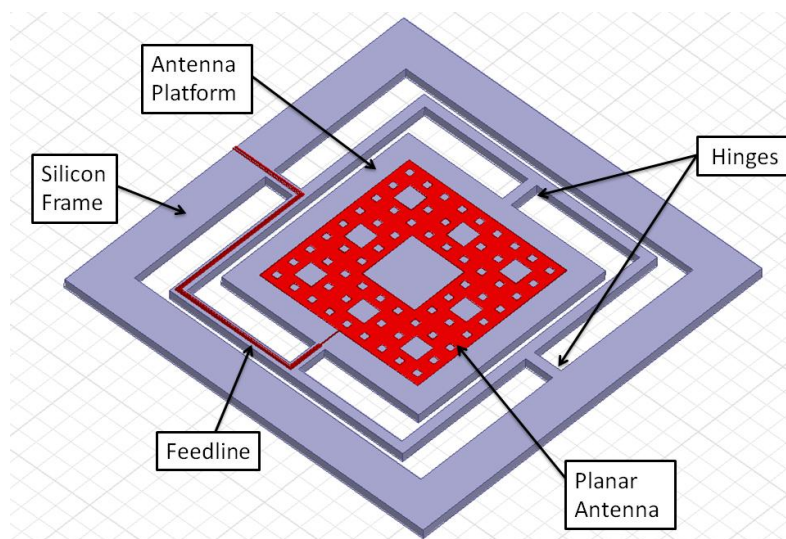
Figure 1.1.1: The Steerable MEMS Antenna

Section 1.1 – Microwaves and Micro Electro-Mechanical Systems

Microwave technology has been developed since the days of Tesla and Edison. The first significant examples of its use in the early 20th century are the telegraph, radio, and radar systems. Today microwave technology is a key technology in the multi-trillion dollar telecommunications and defense industries. The cutting edge technology used to create todays ultra-high density computer processors and ICs have long been adopted to create new devices such as Micro-Electromechanical Systems (MEMS) and Monolithic Microwave Integrated Circuits (MMICs). MEMS find its largest application in sensors and switches. MMICs are at the heart of most modern microwave electronics and systems such as metrology equipment, wireless communications, and radar. The device presented in this thesis has backgrounds in both the MEMS and microwave industries.

MEMS are systems are made up of mechanical and electrical components built onto one or more substrates to create a broad range of devices [2]. MEMS were first developed by mechanical engineers who wanted to capitalize on the advanced processing equipment used by electrical engineers and physicists to create integrated circuits. This design approach is attractive because it can reduce system size and cost while increasing performance for a wide range of applications. Familiar applications of MEMS technology include pressure sensors for atmospheric monitoring, accelerometers for smart phones and airbag deployment, micro-mirrors in DLP™ projectors, and actuators for optical communications fiber alignment. The antenna platform and supporting hinge structure is a good example of how MEMS technology can provide a solution for the actuation of an antenna.

MMICs are a type of integrated circuit designed to work at very high frequencies. They consist of active and passive components built on the same chip and are designed to work in the

RF range of the electromagnetic spectrum (1 GHz – 100 GHz) [3]. At these frequencies device geometry, layout, and materials are very tightly constrained to ensure good device operation. The benefit of putting all circuit elements on one chip is to reduce parasitic losses associated with getting signals to and from semiconductor elements [4]. MMICs use standard micro-fabrication technology to reliably produce the precise geometries and layouts on low loss materials crystalline materials such as Alumina, Quartz, and Gallium Arsenide. In this way, engineers can build devices with passive and active elements on the same substrate. The transmission line and antenna in the steerable MEMS antenna are well known components in MMIC design and analysis.

The merging of MEMS and Microwave technology has created a new field of research and engineering applications known as RF MEMS. The field of RF MEMS was created in 1991 when a team from the Hughes Research Lab created the Micromachined Microwave Actuator, a kind of switch. This was a vast improvement over traditional solid-state switches because the new switches could operate at much higher frequencies with much higher extinction [5, 6]. After the merits of RF MEMS switches were demonstrated, universities and research labs across the globe began to study and improve their performance and marketability. The market share of RF MEMS switches over conventional switches based on PIN diodes or Field Effect Transistors, has been continually growing since their inception [7]. Currently the largest segment of RF MEMS are switches in reconfigurable passive structures such as antennas and filters [8, 9]. The smartphone market is starting to adopt RF MEMS as a viable method of switch between the broadband channels required for today's high speed wireless internet as well. The device presented in this was not a typical RF MEMS device but standard design tools, analysis techniques and fabrication technologies are used to realize this design.

Section 1.2 – Antennas for Imaging

An antenna is a structure that can efficiently couple electromagnetic energy to and from free space. Antennas can be fed electromagnetic energy to transmit a signal or can be arranged to receive radiation from free space. Antennas are the basis of wireless communications, atmospheric and celestial measurements, and imaging and tracking of unknown objects or materials. Antennas are primarily characterized by the center frequency and the bandwidth they operate at. The bandwidth of an antenna is determined by the ratio of the highest and lowest operating frequencies, described by the following equation:

$$Bandwidth = \frac{Upper\ Cutoff\ Frequency}{Lower\ Cutoff\ Frequency} \qquad (1.1)$$

The cutoff frequency exists because antennas cannot efficiently radiate electromagnetic waves at all frequencies. The impedance of an antenna is heavily dependent on frequency. When the antenna impedance does not match the impedance of its driving circuit, reflections occur at the antenna/circuit junction. When this reflection is low, the antenna is said to be impedance matched and will operate. If the reflection gets above -10dB, the antenna is considered to not be operational due to high reflection losses. The challenge of designing a broadband antenna is achieving impedance matching at a wide range of frequencies [10, 11].

Antennas can come in a wide variety of shapes and sizes which are primarily dependent upon their application. This thesis focused on planar antennas because of their ability to be integrated with MEMS and MMIC fabrication techniques. The most basic planar antenna is the resonant patch antenna, which are typically narrow band. The designs presented in this thesis were broadband in nature and did not require a ground plane. Typically a ground plane is present in close proximity to a planar antenna but the ground plane can be eliminated to increase antenna bandwidth. Most communication applications utilize antennas that have a very narrow operating

range to reduce transmission and reception of unwanted signals. Imaging antennas on the other hand, benefit from having a wide operating range to improve the likelihood of accurate detection. The goal for this thesis is to develop an antenna system suitable for use in an imaging system.

Medical imaging with microwaves has been gaining popularity since the 1990s. A great deal of work has been put into analysis of human tissue and the most current results show promising progress in pre, post, and inter-operative analysis of biological tissues. Various systems have been developed to scan tissue samples from 100 MHz to 10 THz. These imaging systems use broadband antennas to improve detection accuracy by scanning samples over a wide range of frequencies [12 – 17].

It is very useful to have a reconfigurable antenna that can alter its radiation characteristics such as operational bandwidth and beam direction or shape in imaging applications. This can be achieved by physically turning or 'steering' the antenna, by tuning the phase of an array of antennas to alter the radiation direction, or switching on or off antennas or other passive elements [18 – 19]. The design presented in this thesis modified its radiation by rotating the platform. This approach is known as mechanical beam steering.

Generally speaking, a planar antenna is one that has been printed or etched onto a dielectric in the proximity of a ground plane. In the case of this thesis, the antenna was designed to be etched out of metal onto a Silicon chip and fed with a grounded transmission line know as a Coplanar Waveguide (CPW). The size of the entire device was no greater than 20 mm in size and less than 500μm in thickness. The antenna geometry used in [1] and in this thesis originated from the same dissertation out of Virginia Tech on new planar wideband antennas [20]. The prototyped design was a modified Fourpoint antenna. The design selected for this paper was a modified Planar Inverted Cone Antenna, and is discussed in Chapters 2 and 4.

Section 1.3 – Micro-Fabrication Technology

Micro-fabrication is used to create all chip based circuits and devices. The semiconductor industry has invested billions of dollars to develop methods to construct microelectronic devices. All devices are realized with three different general steps: pattern transfer, material deposition, and material removal. Together these steps are used for two distinct processes: bulk micromachining and surface micromachining [21]. The driving forces for the development behind micro-fabrication processes is the age old desire for faster, better, cheaper products. Scaling down device size reduces the required materials cost while improving performance. Micro-fabrication is the key to continual reduction in the size and cost of devices from consumer electronics to cutting edge metrology equipment while continually improving performance.

There are three chief methods utilized for pattern transfer: electron beam lithography (EBL), nano-imprint lithography (NIL), and photolithography. NIL and EBL are costly and are only used in applications with the very smallest feature sizes (< 200 nm). Photolithography is the preferred method of pattern transfer because of its high speed and low relative cost to other methods. Photolithography is the process of exposing a photo-sensitive polymer with an image of the desired pattern using light shining through a lithography mask. The polymer is spin-coated onto the substrate and then exposed. Once the exposure has taken place, the polymer is etched by a developer solution to reveal an image of the mask. The polymer is known as photoresist (PR) and comes in two forms; negative and positive image resists. This designation implies that when using positive PR, a positive image of the lithography mask remains after exposure and development. The converse is true for negative PR; the negative image of the lithography mask remains after exposure and development. The patterned PR is then used as a template for selective material deposition or as an etch mask for material removal.

6

There are physical limits to how small of devices engineers can build. Since photolithography is the primary tool for pattern transfer in research and industry, this is where a great deal of the semiconductor industry's innovation has emerged. The minimum feature size is primarily dependent on the wavelength of light used and the type of lithography mask used. A photoplot is a type of lithography mask that has been printed on a clear plastic film with a high resolution printer and can realize features as small as 15 μm. A photomask is the more commonly used lithography mask since it can be used to create features that are < 1 μm. Today, industry can build 22 nm features in production volume manufacturing.

It is the successive material deposition and removal steps between pattern transfer steps that create microelectronic and MEMS devices one layer at a time. There are two major material growth techniques as well as removal methods. The two kinds of deposition are chemical vapor deposition (CVD) and physical vapor deposition (PVD). Each has distinct advantages and limitations that must be weighed based on application. Generally, insulators are usually deposited with CVD and metals are deposited with PVD, although there are exceptions. The kinds of removal are wet etching and dry etching. Again, the best method is application dependent.

Two types of material removal process are required to create steerable MEMS antennas; wet and dry etching. The silicon is etched with both processes while the metals use a wet etch. A wet etch uses a liquid chemical etchant to erode away any layer in a microelectronic or MEMS device. The etch rates of wet etching are primarily controlled by reactive chemical concentration and temperature. The metal and photoresist was etched using off the shelf etchants. Wet etching in Silicon is achieved with Potassium Hydroxide and Tetramethylammonium Hydroxide (TMAH). These chemicals are routinely used to anisotropically etch [100] Silicon. This process

is generally associated with bulk micromachining and is a fundamental step in building the antenna platform in the steerable MEMS antenna.

The second Silicon etching technique was Deep Reactive Ion Etching (DRIE) using the Bosch process. The Bosch is a hybrid process of alternating ballistic ion etching and passivation steps. DRIE can be used to create high aspect ratio structures in addition to being a reliable and controllable etching method ranging from $0.5 - 4$ µm/min [22]. DRIE is the process used to create the hinges by etching through the membrane that is the antenna platform.

Section 1.4 – Finite Element Analysis

The bulk of the work presented in this thesis was computational analysis of all the elements of the steerable MEMS antenna for optimization and performance improvement. The mechanical operation of most design variations of were modeled with closed form expressions. The antenna, feedline, and first generation hinge structure were not modeled with closed form expressions because the complex nature of electromagnetic wave propagation in devices excluded the potential for closed form design equations in many devices such as planar waveguides and antennas. All of the electrical elements of the design were analyzed numerically using Finite Element Analysis (FEA). The tool of choice was Ansys' High Frequency Selective Surface (HFSS) modeling package. COMSOL was the tool of choice to model the first generation hinge structure.

Finite Element Analysis is the method used by both COMSOL and HFSS to solve complex boundary value problems governed by differential equations. FEA was originally developed to solve mechanical stress problems in the aerospace industry. FEA breaks a geometry into many simple small elements called mesh cells for numerical analysis. This method is particularly useful when desired solutions are not easily described by uniform, linear, or

exponential distributions as in complex geometries. In two dimensional problems, the mesh cells are triangles and are tetrahedrons in three dimensional problems. The mesh cells are made small enough so that output variables can be described by uniform, linear, or exponential distributions throughout the cell. This allows complicated geometries to be discretized into many simple shapes which can be easily solved using linear algebra solution techniques or numerically solved using the Euler or Runge-Kutta method. FEA enables engineers to quickly and accurately solve problems that would otherwise be full of solution degrading approximations or simply take too long to solve. Without advanced simulation packages such as HFSS and COMSOL, it would be nearly impossible to keep developing higher and higher frequency devices which is important to numerous fields including, defense, security, medical imaging, and communications

In all of the models created, device geometries were parameterized in a master list. Any aspect of the design could be modified by simply changing the value of a parameter. This allowed for parametric analysis of the designs for optimization and performance enhancement. The advantage of this approach is ease and speed of analysis.

The efficacy of HFSS to accurately simulate antenna performance is demonstrated by a comparison between a simulation and actual measurement. A slotted bowtie antenna was designed and fabricated as a class project by this author in the spring of 2012. The antenna was modeled and optimized in HFSS and then fabricated and tested. The antenna was fabricated in the High Density Electronics Center at the University of Arkansas on April 24th, 2012. A schematic and photograph of the realized antenna is shown in Figure 1.4.1. The values for the geometric parameters in the final antenna design are shown in Table 1.4.1.
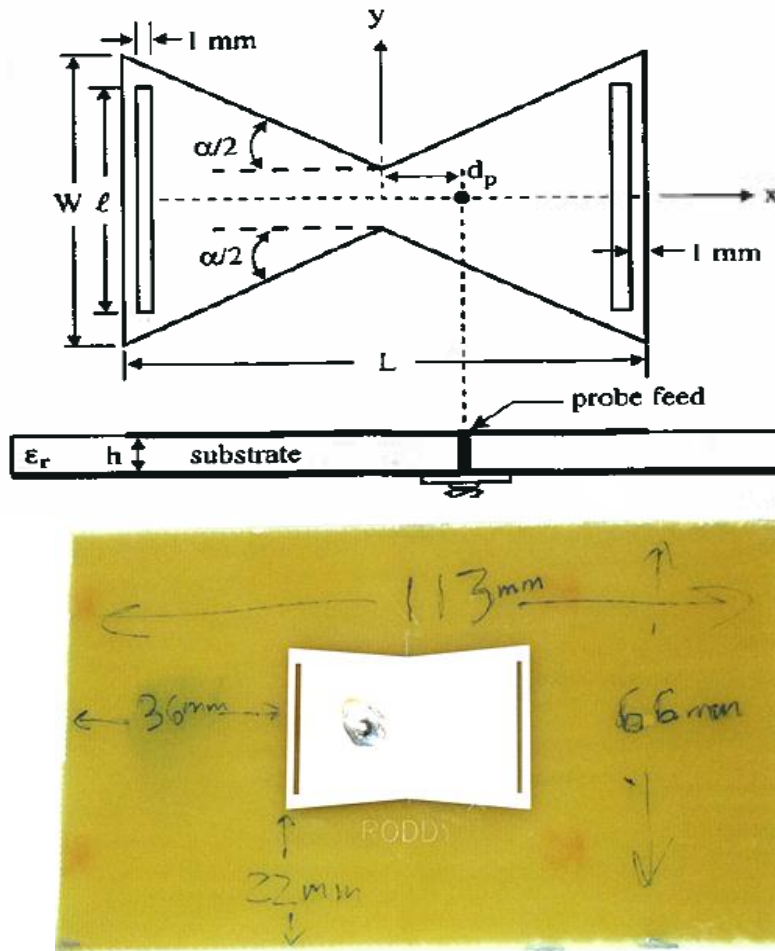
Figure 1.4.1: Schematic and Photograph of the Slotted Bowtie Antenna Designed and Tested by Morgan Roddy for the Antennas Class at the University of Arkansas

W (mm)	L (mm)	L (mm)	α (degrees)	H (mm)	ε_r	D_p (mm)
25.2	37.5	20.7	10	1.5	4.34	6.95

Table 1.4.1: Design Parameters of the Fabricated Slotted Bowtie Antenna

The antenna was measured at the University of Arkansas on May 1, 2012. The measured and theoretical results are shown in Figure 1.4.2. A summary of the predicted and measured locations of the antennas' operational modes and the associated errors are shown in Table 1.4.2.
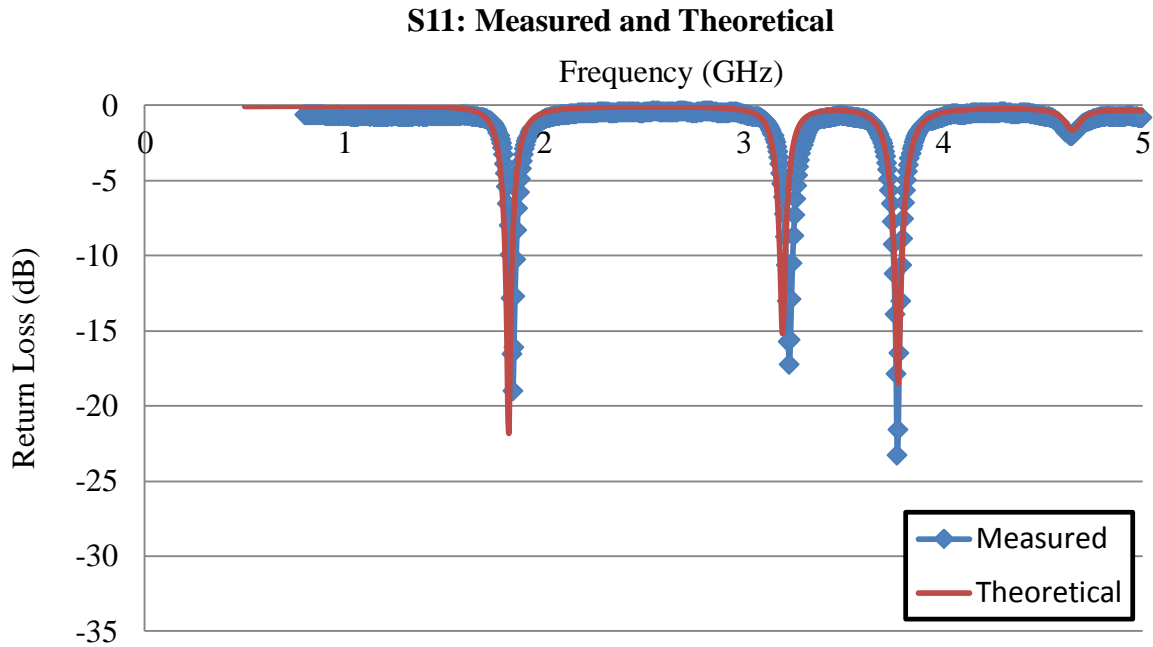
Figure 1.4.2: Theoretical and Measured Return Loss of the Slotted Bowtie Antenna

Operational Mode	Predicted Frequency (GHz)	Measured Frequency (GHz)	Error (%)
1st Peak	1.825	1.8448	-1.10
2nd Peak	3.195	3.2308	-1.10
3rd Peak	3.775	3.7715	0.10

Table 1.4.2: Comparison between the Predicted and Measured Operational Modes of the Slotted Bowtie Antenna

The results presented in Figure 1.4.2 and Table 1.4.2 demonstrate the ability of this author and the HFSS software package to accurately model and predict antenna behavior.

11

Chapter 2: Literature Review and Analysis

A great number of papers and books were searched to develop a sufficient level of understanding to complete this thesis. Topics included MMICs, MEMS, broadband antennas, high-gain antennas, transmission lines, fabrication techniques, millimeter-wave and THz technology and theory, and impedance matching. The most important publication in the creation of this thesis was Dr. Hutchings' dissertation and several of his key references were also used. Other key papers in specific areas were reviewed and were important to support the methods and realization of this thesis.

Section 2.1 – Micro-Actuation with MEMS

Microactuation has become an important technique in reconfigurable microwave devices and compact optical systems, as well as many other applications. A class of MEMS devices whose size and range of motion is in the micrometer range is known as microactuatuators. The massive microwave and communications industries have greatly benefitted from the development of microactuation systems.

Two important methods are used for actuation of MEMS devices; electrostatic actuation and magnetic actuation. Other approaches exist but fail to supply sufficient force for the purpose of this thesis. The best method to use depends heavily on application and based on the required range of motion and actuation force. Electrostatic actuation is relatively weak compared to magnetic actuation but is much easier to incorporate in to device designs. The ease of generating electric fields compared to magnetic fields on MEMS devices makes electrostatic actuation more popular due to its simplicity. The actuation paradigm used for this thesis was electrostatic actuation and is described in further detail in Section 2.4.

The Coulomb force is the basis of electrostatic actuation and is used to apply a force between a stationary and a movable structure through an applied electric field. Movable structures are typically attached to the stationary substrate on micromachined hinges. There are two most common electrostatic actuation methods; parallel plate actuators and comb drives. Actuators used for in-plane motion in MEMS devices are typically electrostatic comb drives while out of plane motion is achieved with parallel plate actuators [23].

The most basic model of an electrostatic actuator consists of a fixed electrode next to an electrode attached to a spring. A voltage is applied to the electrodes. Similar electric potential on each electrode will cause the electrodes to separate. Electrodes will be attracted to one another when they are oppositely charged. A schematic of this setup is shown in Figure 2.1.1.
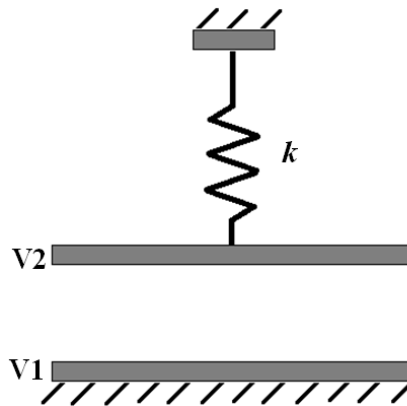
Figure 2.1.1: Schematic of a Basic Parallel Plate Electrostatic Actuator

Electrostatic actuators suffer from a phenomenon known as pull-in or snap-down [24]. This occurs when oppositely charged electrodes get too close to one another and the strength of the attractive Coulomb force overcomes the reactive force in the hinges. As the actuation voltage increases and the electrodes become closer together, the Coulomb force grows as the inverse squared of the distance between electrodes. However, the reactive spring force only grows linearly as spring stretches. The pull-in voltage is the potential at which the Coulomb force becomes greater than the spring force can restore and the two electrodes will snap together. This

13

raises a critical design concern. Unless planned for, pull-in can easily break devices. For the purpose of this thesis it is desirable to operate below the pull-in threshold. An electrostatic switch for RF MEMS is a good example of an application where pull-in is desirable to make good electrical contacts

A comb drive consists of a pair of interdigitated electrodes that are biased according to an actuation paradigm. The force this kind of drive can supply is based on the size of the electrodes, the number of electrodes, and the applied voltage. The number of comb electrodes typically range from 10 − 100, the size of the electrodes are in the micrometer range, and actuation voltages can be in the hundreds of volts range. There are three bias techniques used in comb drives to achieve in-and-out or lateral motion [25].

Magnetic actuation is based on the Lorentz force which uses an external magnetic field to apply a torque on a coil in a portion of a device. This actuation paradigm is attractive because relatively large forces can be generated with low coil currents compared to electrostatic actuation. Magnetic actuation relies on the use of inductive coils in the plane of the device coupled with an external 'control' field. The geometry of how coils and external fields are oriented with respect each other and the rest of the device in question determine how actuation occurs. It is through the clever arrangement of on-chip coils in a device that allows magnetic actuation to be exploited. This fact was exploited to create a micro-mirror for alignment of optical fibers with 3 degrees of freedom using five on-chip magnetic coils and in the presence of a single external magnetic field [26]. The micro-mirror could rotate about the X and Y axis and translate in the Z-direction. By controlling which actuation coils are on, it is possible to achieve the three different ranges of motion with a single external magnetic control field in the X-direction. The micromirror was able to achieve ± 4.2° of rotation about the X-axis, ± 9.2° of

14

rotation about the Y-axis, and ± 42 µm of translation in the Z-direction with actuation voltages < 3.0 V and actuation currents < 120 mA.

In summary, magnetic actuation is complicated to realize but has the advantage of having low actuation voltages and currents. Electrostatic actuation is relatively easier to design but has the disadvantage of having higher actuation voltages.

Section 2.2 – Antennas

The goal of this thesis was to create a broadband antenna and so great care was taken to select the antennas presented in this thesis. A critical requirement was that all designs had to be suitable for integration with the steerable MEMS antenna platform which ruled out a great deal of possibilities. A suitable antenna had to be planar, fed by a planar transmission line, and be compatible with MEMS fabrication techniques. This literature review will focus on the broadband antenna designs investigated.

Antennas have a limit on the range of frequencies they can operate at because their efficiency of transmitting or receiving electromagnetic radiation is geometry dependent. Generally speaking, antennas are more efficient radiators if they are no less than half of a wavelength in size at the frequencies of operation. Reducing the size of an antenna will increase its operational frequency. This effect can be very useful to designers because a good design can be scaled to operate in a wide range of frequency bands based on application [11].

The most basic antenna is the thin monopole antenna and is the basis of many other antennas. The second most basic antenna is the thin dipole antenna which is nothing more than two out of phase monopole antennas next to one another. The shape of the monopole or dipole can be widened to form various other shapes including a disc antenna, cone antenna, and bowtie antenna [20]. Other antennas comprised of multiple monopole and/or dipole elements include the

15

Yagi-Uda antenna [27], modified fourpoint antenna [1, 20] and planar inverted cone antenna [20].

Broadband antennas have been designed and built for over a century starting with the original spark-gap transmitters used by Marconi, Tesla, and others in the pioneering days of radio. There has been a great deal of research into creating broadband antennas. It was discovered in the 1950s that it is possible to create an antenna whose geometry does not significantly affect its operational range. These antennas were known as frequency independent antennas and their geometry could be described by angles alone. These spiral shaped antennas could operate from 10 – 10,000 MHz [11]. A spiral antenna is not good for this work because it requires the antenna to be fed from the center of the antenna and this is not suitable for integration with a steerable MEMS platform. Commercial broadband spiral antennas can operate from 0.5 – 18.0 GHz and have a bandwidth ratio of 36 [28].

Fractal antennas are a relatively new discovery and can achieve high bandwidth and operate at frequencies with wavelengths much larger than their geometries. Fractal antennas were first discovered by amateur radio enthusiasts in an effort to reduce the size of their HAM radio antennas in cities. The first fractal antenna was patented in 2000 and is based on a square loop antenna [29]. Fractal antennas are electrically small and can be broadband or multiband [30, 31]. They also can be wire loop antennas, planar antennas, or resonant patch antennas. A fractal antenna is created by repeating geometric elements or motifs at multiple size scales. The aforementioned antenna in [29] started out as a square loop antenna. The outline was changed with a simple process multiple times. An illustration of the starting square loop and the first two geometric modifications are shown in Figure 2.2.1.
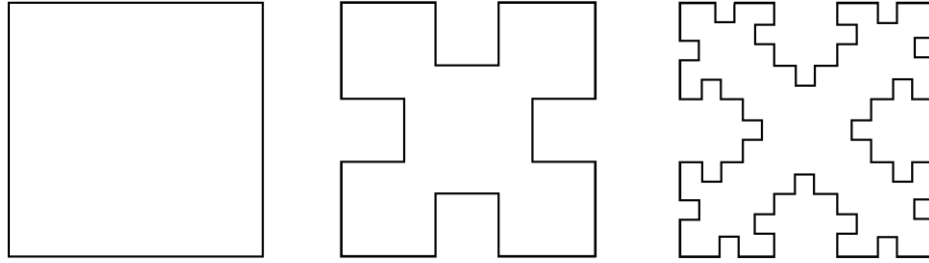
Figure 2.2.1: Illustration of the Iterative Process of Creating a Square Fractal

A resonate patch antenna is comprised of a planar electrical trace in close proximity to ground. Good impedance matching can be achieved at the resonate frequency of the antenna but is poor at all other frequencies making this design narrow band. Fractal patch antennas have been created that had improved bandwidth over similar designs without iterated geometric motifs. The patch antenna was investigated for integration with the steerable MEMS platform but was rejected because it could not achieve sufficient bandwidth for the design goals of this thesis.

The main design investigated in this thesis and the prototypic work [1] was a planar monopole/dipole design. This was very similar to the resonant patch antenna with the exception of the ground plane. There was no ground plane in these designs which improves bandwidth. The design most widely studied in this thesis was the planar inverted cone antenna (PCIA) and is described in great detail in the following section.

It was desirable to attempt to integrate more than one antenna design with the steerable MEMS platform to demonstrate this system's versatility. The PICA was studied on three different variations of the MEMS platform. The best platform design was also studied with two more antennas; a cylindrical dielectric resonator antenna (C-DRA) and a teardrop dielectric resonator antenna (Td-DRA). Both DRAs were very thin (< 1 mm) and the Td-PICA used the same teardrop shaped that was optimized for the Td-PICA

A dielectric resonator antenna (DRA) is an interesting development in antenna technology that was first presented in 1983 [32]. The DRA was developed because traditional

17

metal antennas become lossy at very high frequencies (> 26.5 GHz). A DRA is pumped with electromagnetic energy through a transmission line and then resonates similar to a laser cavity. Losses through the sides of the dielectric material are radiated into free space thus creating an antenna. Typical DRA shapes include square or rectangular boxes and cylinders.

The DRA was relevant to this thesis because dielectrics can be deposited and patterned using MEMS fabrication techniques. This allows for relatively easy integration of the DRA with the steerable MEMS platform. There has also been significant work done in the area of broadband DRAs which supported the goal of this thesis [33, 34]. The two most significant factors that affect DRA performance are the geometry of the antenna and the dielectric constant of the material. Selecting a material with a high permittivity will increase the frequency range over which the antenna operates while lower permittivity will result in lower frequency ranges. Even with low dielectric constants, it is possible to scale DRAs to work at extremely high frequencies into the terahertz regime [35]. The material selected for designs presented in this thesis was Polyimide which has a relative dielectric constant of 3.5 and can be easily processed with standard MEMS fabrication techniques.

Antennas send and receive signals to and from external networks such as signal generators and analyzers through transmission lines (TL). A TL can take many forms such as waveguides, coaxial cables, planar TLs. The prototyped devices that this thesis was based on used a coaxial cable to a SMA connector to send energy to the device. A planar TL brought energy from the connector to the antenna trace. No work was done to study the coaxial line or SMA connector because these are very standard off-the-shelf parts. The planar TL on the other hand had to be studied. There are several common types of planar used in antennas and as well as MMICs. Two common types include the microstrip line and coplanar waveguide.

18

All the antennas presented in this thesis were fed by a Coplanar Waveguide (CPW). The most important parameter of a CPW or any TL for that matter is its characteristic impedance, denoted by Z_o. This parameter is very important to impedance match antennas to external networks. There is no simple expression for the characteristic impedance of the CPW. A full wave analysis of the CPW was studied from literature and was used to determine impedance [36]. A schematic of the CPW is shown in Figure 2.2.2 and the equations used to calculate Z_o are shown and described below.
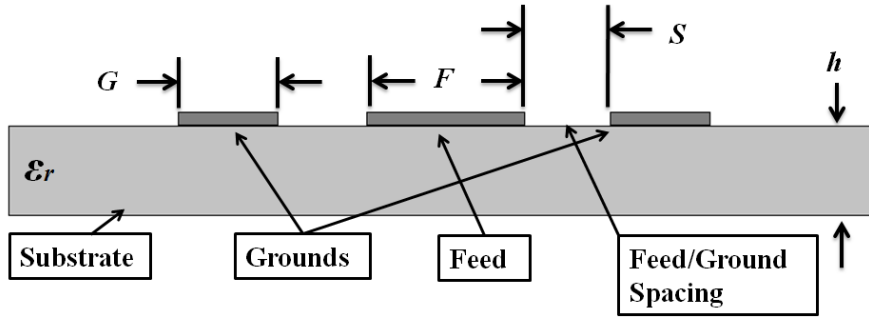
Figure 2.2.2: Schematic of a Coplanar Waveguide (redrawn from [36])

The CPW geometry was transformed from *F*, *S*, and *G* to *a*, *b*, and *c* for this analysis in the manner shown in equations (2.1) – (2.3)

$$a = \frac{F}{2} \qquad (2.1)$$

$$b = \frac{F + 2 * S}{2} \qquad (2.2)$$

$$c = \frac{F + 2 * S + 2 * G}{2} \qquad (2.3)$$

Three intermediate parameters were calculated based on the geometry and are shown in equations (2.4) – (2.6).

$$k_3 = \frac{a}{b} \sqrt{\frac{1 - b^2/c^2}{1 - a^2/c^2}} \qquad (2.4)$$

$$k^{`}{}_3 = \sqrt{1 - k_3^2} \tag{2.5}$$

$$k_4 = \frac{sinh(\frac{\pi a}{2h})}{sinh(\frac{\pi b}{2h})} \sqrt{\frac{1 - sinh^2(\frac{\pi b}{2h})/sinh^2(\frac{\pi c}{2h})}{1 - sinh^2(\frac{\pi a}{2h})/sinh^2(\frac{\pi c}{2h})}} \tag{2.6}$$

The effective permittivity of the CPW was calculated from the intermediate parameters using the complete elliptic integral of the first kind, $K(..)$.

$$K(x) = \int_0^{\frac{\pi}{2}} \frac{d\theta}{\sqrt{1 - x * sin^2(\theta)}} \tag{2.7}$$

$$\varepsilon_{re} = 1 + \frac{\varepsilon_r - 1}{2} \frac{K(k_4)}{K^{`}(k_4)} \frac{K^{`}(k_3)}{K(k_3)} \tag{2.8}$$

Lastly, the characteristic impedance of the CPW were determined.

$$Z_{o\,cpw} = \frac{30\pi}{\sqrt{\varepsilon_{re}}} \frac{K(k^{`}{}_3)}{K(k_3)} \tag{2.9}$$

This analysis was used to develop a Matlab code to determine the characteristic impedance of proposed design variation. This predictive code was used as described in Chapter 4.

Section 2.3 – The Planar Inverted Cone Antenna Background and Optimization

The teardrop planar inverted cone antenna [20] (Td-PICA) was selected for optimization and integration with the MEMS antenna platform. The design originates from the same dissertation that inspired the Modified Fourpoint Antenna used in [1]. The Planar Inverted Cone Antenna (PICA) was introduced in a dissertation from Virginia Tech's Antennas Laboratory in 2002 by Seong-Youp Suh [20]. His dissertation described numerous new antenna designs in great detail. The PICA design was selected for its ultra wideband performance and its planar

geometry. A great deal of time was spent on selecting this design to optimize for integration in the antenna platform. It was selected for satisfying three critical design constraints: wide bandwidth, planar geometry, and omnidirectional radiation pattern. Wide bandwidth was a chief design concern because of it useful potential applications. Planar geometry was a requirement because no other configuration could be integrated with the steerable antenna platform. Omnidirectional radiation pattern was desired for maximum versatility for application.

The base Td-PICA antenna is defined by a polyline running through 16 points on its edge. The length and width are both normalized to 1. A schematic of the normalized Td-PICA and how it is defined is shown in Figure 2.3.1.

	X	Y
p1	0	0
p2	0.133*W*L	0.032*L
p3	0.266*W*L	0.081*L
p4	0.400*W*L	0.161*L
p5	0.433*W*L	0.210*L
p6	0.467*W*L	0.258*L
p7	0.500*W*L	0.323*L
p8	0.500*W*L	0.403*L
p9	0.467*W*L	0.452*L
p10	0.416*W*L	0.516*L
p11	0.334*W*L	0.580*L
p12	0.233*W*L	0.645*L
p13	0.100*W*L	0.774*L
p14	0.050*W*L	0.855*L
p15	0.033*W*L	0.903*L
p16	0	1*L
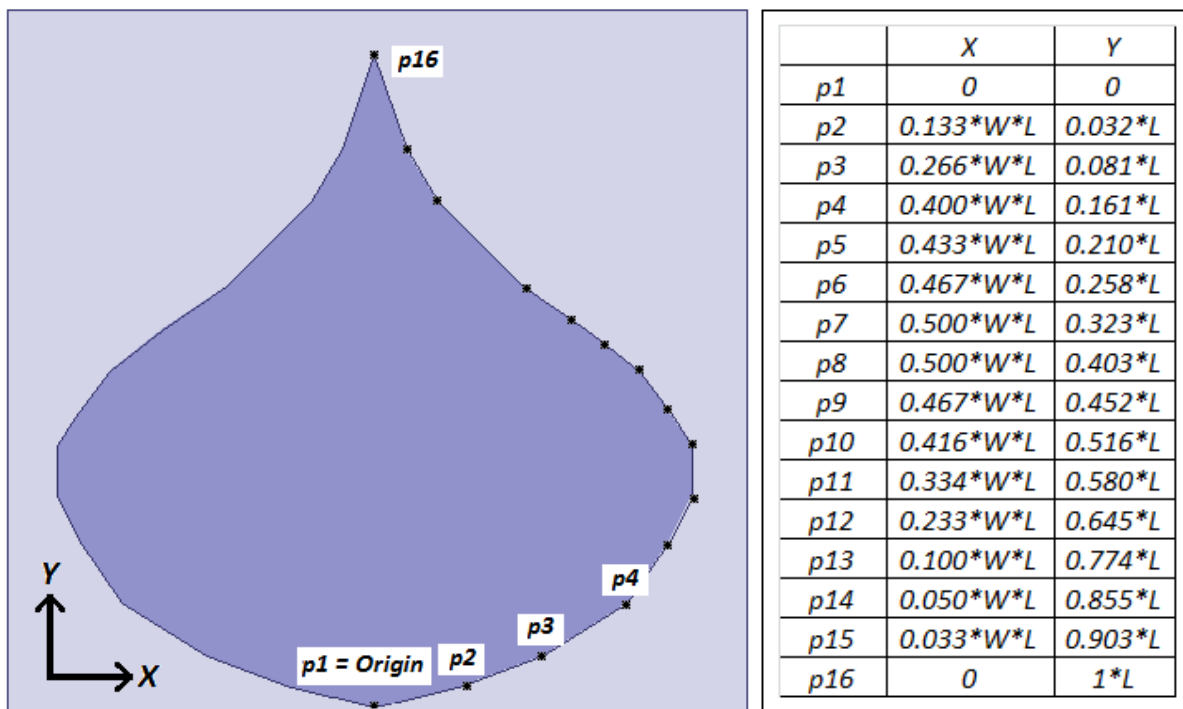
Figure 2.3.1: Normalized Teardrop Planar Inverted Cone Antenna defined by a 16 point polyline

An optimization model of the Td-PICA on Silicon fed by a coplanar waveguide (CPW) was built and studied in Ansys' HFSS. The design was parameterized in six ways; one to control the antenna size, one to control the teardrop aspect ratio, three to define the CPW, and one to

control the silicon thickness. Studies of these variables were undertaken to understand the Td-PICA design and how to best integrate it with the antenna platform.

The size of the antenna was controlled by scaling every point in the polyline defining the antenna by the parameter *L*. The operational frequencies of Td-PICA are determined by the overall size of the antenna. *L* was therefore used to select the operational frequency of the antenna but was held constant at *L = 6.2 mm* for all studies.

The aspect ratio of the antenna was controlled by scaling all of the X-coordinates in the polyline defining the antenna by the parameter *W*. The feed width of the CPW was designated *F*. The width of the symmetric ground of the CPW was designated *G*. The spacing between CPW feed and grounds was designated *S*. The thickness of the silicon membrane upon which the antenna and CPW are built on was designated *h*.

The fundamental way to achieve good impedance bandwidth is to ensure the antenna, transmission line, and source, all have equal impedance. The parameter *W* was used to control antenna impedance. The CPW variables *F, S,* and *G* were used to match the transmission line impedance to the antenna and the input/output port. The thickness of the antenna platform can affect antenna performance by introducing losses so *h* was also used to facilitate impedance matching in the design. Together, these parameters effectively were tuned until a broadband antenna was realized. The experimental range of the Td-PICA design parameters presented in this thesis are shown in Table 2.3.1.

Parameter	Range of Values
L	6.2 mm
W	0.25 - 1.5
F	7.5 – 20 μm
G	7.5 - 26 μm
S	5 - 26 μm
h	60 - 240 μm

Table 2.3.1: Experimental Domain of the
Teardrop Planar Inverted Cone Antenna
Design Parameters

The Td-PICA presented in Suh's dissertation [20] was modeled in HFSS to compare to

the published performance. The literature presented the voltage standing wave ratio (VSWR) as a

performance metric instead of the return loss. A comparison between the published results of the

antenna and this author's own model are shown in Figure 2.3.2.
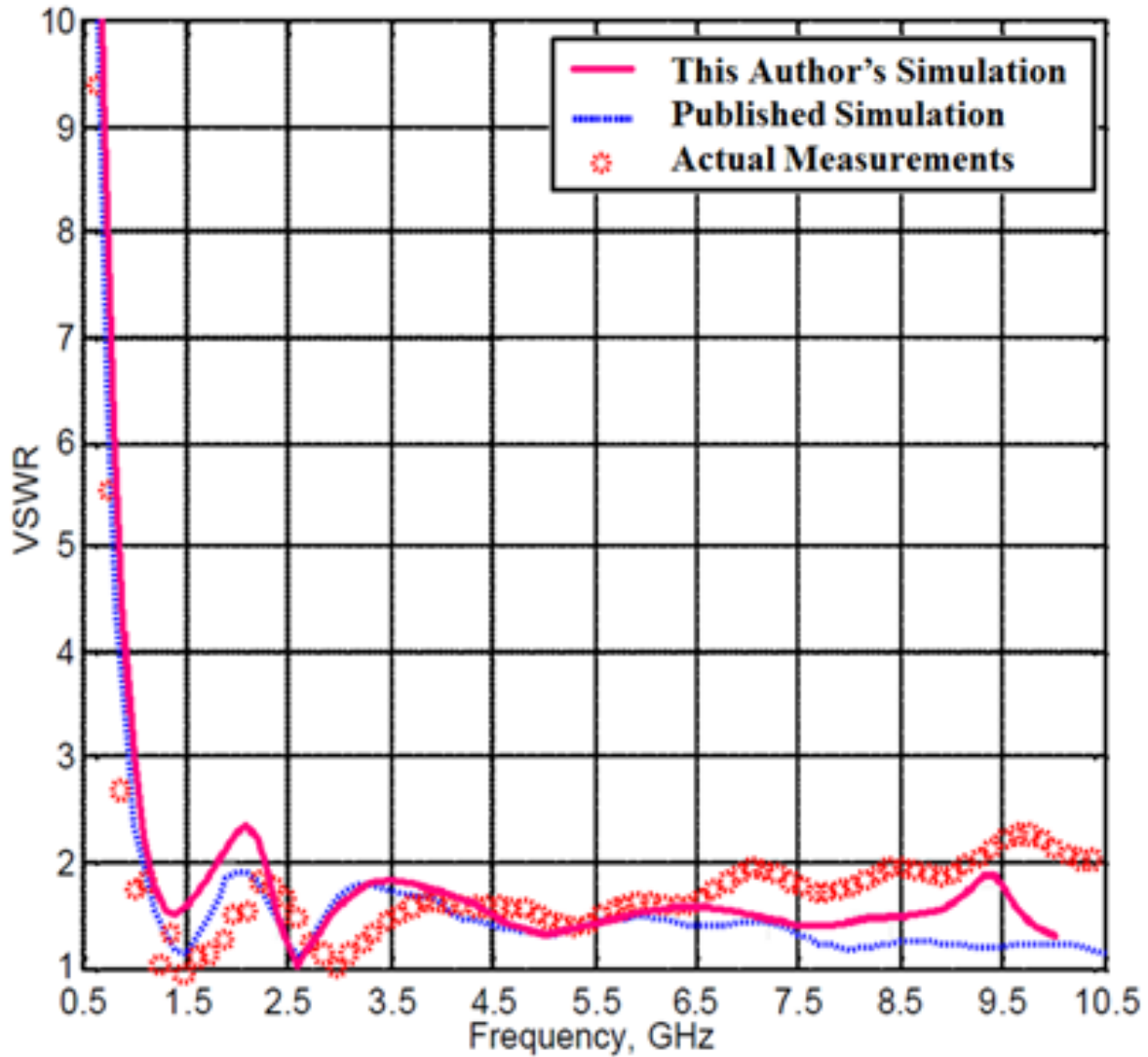
Figure 2.3.2: Comparison Between This Author's Simulations and the Published Theoretical and Measured Performance of a Teardrop Planar Inverted Cone Antenna [20]

The results presented in Figure 2.3.2 demonstrated the ability of this author and the HFSS software package to accurately model and predict antenna behavior. The difference in the two computational results can be attributed variations in simulation techniques. The differences between the measured result and both simulations were the fact that there is no electrical noise accounted for in the simulations.

Section 2.4 – The Steerable MEMS Antenna Modeling and Performance

The basis for this thesis was the design developed by Dr. Hutchings in his dissertation at the University of Arkansas under the guidance of the same major processor as this thesis, Dr. Magda El-Shenawee. Dr. Hutchings drew inspiration, in part, from several publications presented in this literature review. His final design consisted of six major components; the device frame, intermediate frame, torsion hinges, antenna platform, feedline, and antenna. A diagram with the basic elements of the steerable MEMS antenna is shown in Figure 2.4.1 with a generic square fractal antenna.
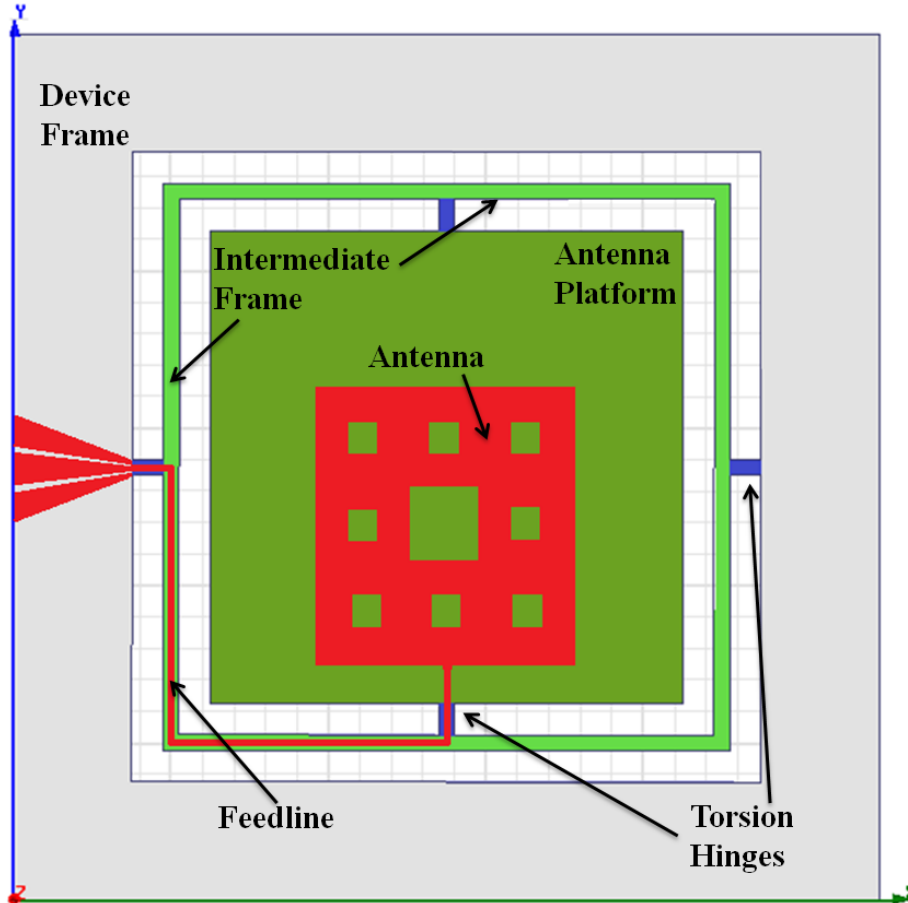
Figure 2.4.1: Parts of a Steerable MEMS Antenna

A schematic of the steerable MEMS antenna is shown in Figure 2.4.2.

25
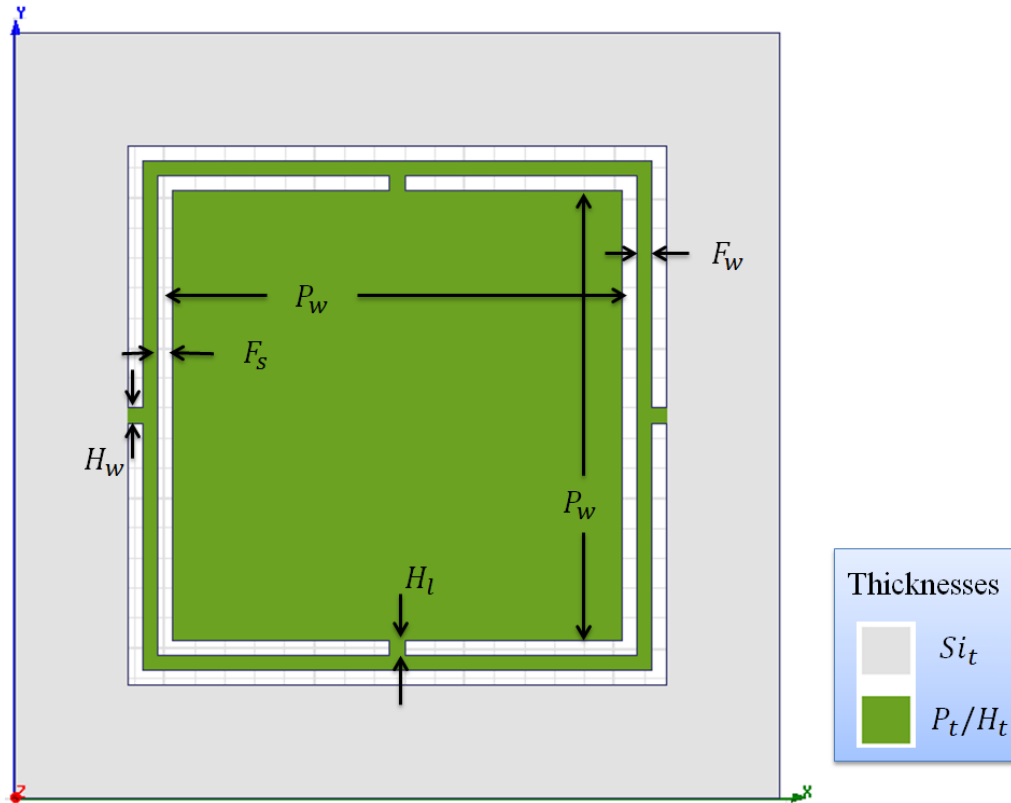
Figure 2.4.2: Parameterized Geometry of the Prototypic G1 Antenna Platform

Prototype devices were fabricated at the University of Arkansas' High Density Electronics Center (HiDEC). A detailed description of the fabrication process and the challenges encountered in realizing working devices is presented in [1]. The prototype was built by first creating thin silicon membranes through a backside anisotropic etch. Both KOH and TMAH were tested and TMAH had the best results. The antenna and feedline were added by depositing and then patterning metal on the top of the device. The metal was a three layer stack of 500 nm Titanium, 2.00 μm Copper, and 500 nm Titanium. The antenna platforms were released in the last step and the hinge structure created by selectively etching through the silicon membrane with DRIE.

The prototypic steerable MEMS antenna used an electrostatic actuation paradigm. The antenna platform was rotated by placing a high voltage conductor under one edge of the platform

resulting in a capacitive force. The electrostatic force is relatively weak compared to other forces such as the magnetomotive force and voltages as high as 800 V were required to rotate the antenna platform. The electrostatic force is a function of electric potential, platform/conductor area, and the platform/conductor gap. The opposing forces are the torques in the torsion hinges which are a function of the hinge material, cross section, length, and the angle of deflection. A free body diagram of the antenna platform in operation is shown in Figure 2.4.3.
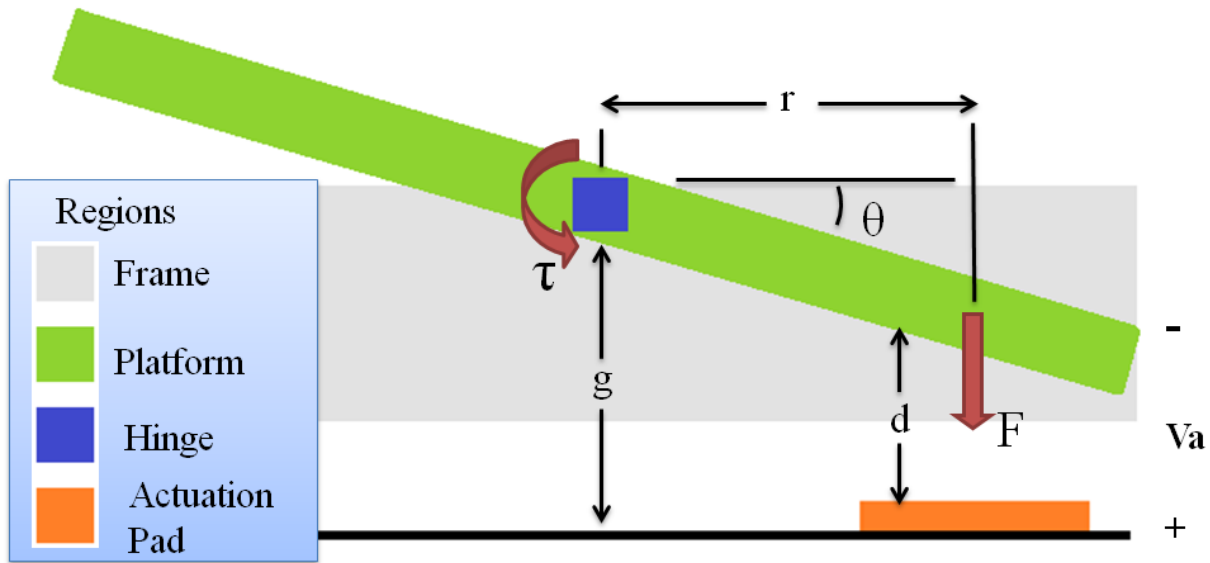
Figure 2.4.3: Free-Body Diagram of Electrostatic Action of the Steerable MEMS Antenna

A model of the operation of the steerable MEMS antenna platform was developed to help understand the device's behavior. This model was compared to the performance of devices reported by [1] for fabricated prototype devices. At static equilibrium, Equation 2.10 must be true where F is the applied capacitive force, τ is the torque in one hinge and the actuation radius r is the distance from the axis of rotation to the effective applied force.

$$F = \frac{2 * \tau}{r} \tag{2.10}$$

The expressions for capacitive force and torsion in a rectangular beam are as follows.

$$\tau = \frac{G * \theta * J}{l} \tag{2.11}$$

$$F = \frac{\varepsilon_0 * A * V^2}{2 * d^2} \tag{2.12}$$

For the torque, G is the sheer modulus of the hinge, J is the second moment of area of the hinge cross section, l is the hinge length, and θ is defined in the free-body diagram. The value of G for silicon used in this model was 79.4 GPa [37]. For the capacitive force, ε_0 is the permittivity of free space, A is the area of the actuation pad, V is the applied electric potential, and d is defined in the free-body diagram. It is desirable to know the operation angle θ as a function of the input voltage, V. The second moment of area and operation angle can be described from the geometry as follows.

$$J = \frac{H_t * H_w * (H_t^2 + H_w^2)}{12} \tag{2.13}$$

$$d = g - r * \tan(\theta) \tag{2.14}$$

For the second moment of area, t and w are the hinge thickness and hinge width respectively. For the operation angle, g, d, and r, are defined in the free-body diagram. Solving for actuation voltage as a function of the materials and geometry yields the Equation 2.15. This equation is referred to as the base actuation model which is a function of device geometry and actuation setup.

$$V = \sqrt{\frac{4 * G * J * \theta}{\varepsilon_0 * l * A * r} (g - r * \tan(\theta))^2} \tag{2.15}$$

The actuation area A was unknown for the actual measurements taken in [1] so this parameter was a logical choice to use as a fitting variable. Based on information in [1], a reasonable value for A was chosen as 25% of the area of the antenna platform. The value for g was given in [1] for measured devices. The value for r was not given either because it did not

have a fixed value so this was also used as a fitting variable. The rest of the variables in the actuation model were known or were defined. An effective actuation area and radius was used in the final expression for the actuation model and is shown below. The estimated actuation area and radius and their effective definitions are shown below. The actuation model is solved with the actuation voltage as a function of device geometry and actuation angle and is also shown below.

$$A = 0.25 * P_w^2 \tag{2.16}$$

$$r = 0.35 * P_w \tag{2.17}$$

$$A_{eff} = k_A * A \tag{2.18}$$

$$r_{eff} = k_r * r \tag{2.19}$$

$$V = \sqrt{\frac{4 * G * J * \theta}{\varepsilon_0 * H_l * A_{eff} * r_{eff}} \left(g - r_{eff} * \tan(\theta)\right)^2} \tag{2.20}$$

It was more convenient to solve for actuation voltage instead operation angle even though the goal of modeling this system was to be able to predict operation angle. This approach also was numerically more accurate. Equation (2.20) was numerically solved by selecting input values of θ ranging from $0 - 1.2°$ and then solving for the required actuation voltage. The fitting variables k_A and k_r were used to fit the model to a specific device that was measured and reported in [1].

The fitting variables were parametrically swept to find matched pairs that resulted in a prediction in accordance with the reported device performance. Equation (2.20) was numerically solved to find a range fitting variables that would satisfy the following relationship.

$$V(k_A, k_r, \theta = 1.2°) = 800 \, V \tag{2.21}$$

29

A range scatter plot of a range fitting variables that satisfy Equation (2.21) is shown in Figure 2.4.4.
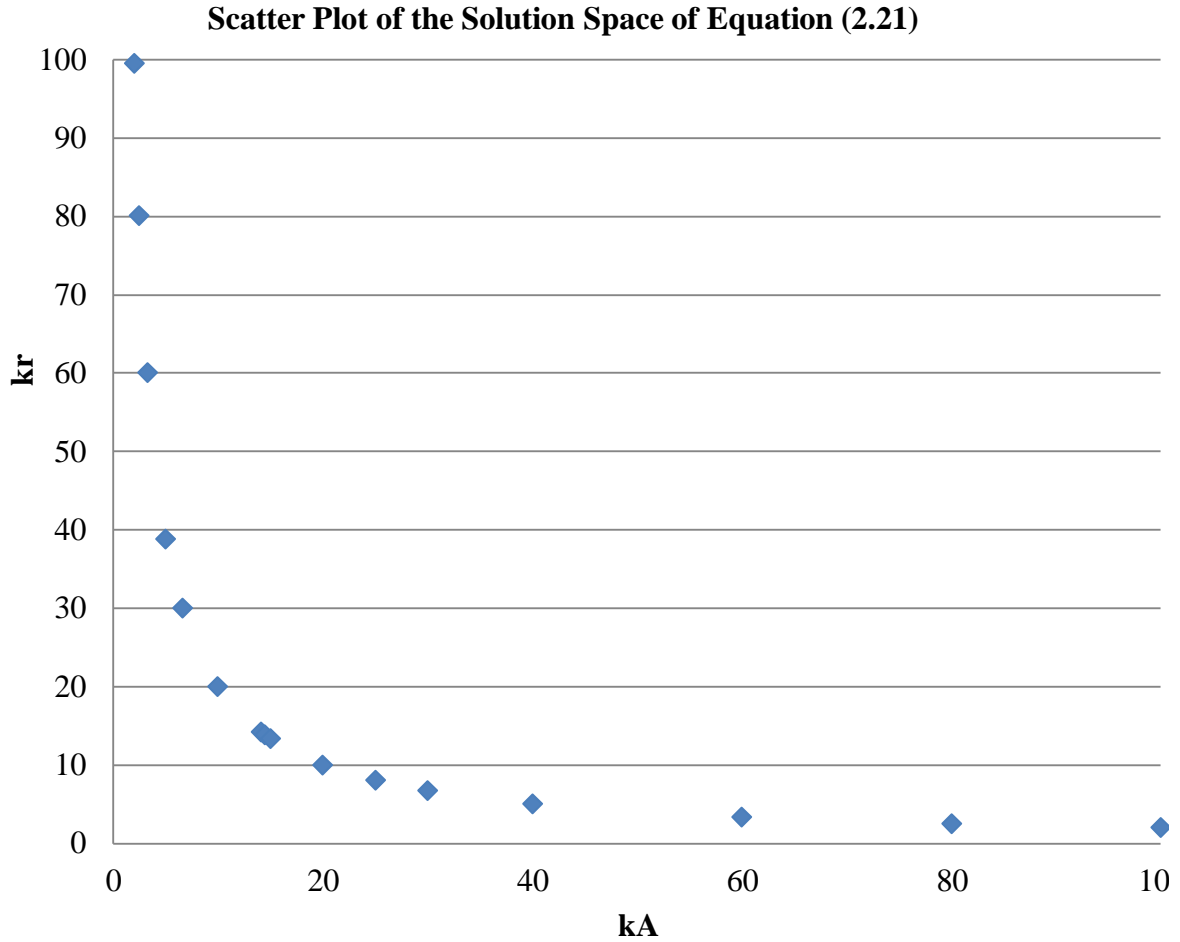
Figure 2.4.4: Scatter plot of Solution Space of Equation 2.21

The fitting variables should ideally be unity. The actuation model however, does not predict what was measured without the use of the fitting variables. For this reason the fitting variables were simultaneously minimized. Due to nature of the relationship between the two fitting variables, the minimum was found when they were equal to each other which occured for the following condition.

$$k_A = k_r = 14.11 \tag{2.21}$$

The measured and predicted operation of a prototype steerable MEMS antenna platform reported by [1] is compared to the new model developed in this thesis in Figure 2.4.5. The values used for the fixed parameters and fitting variables in the actuation model are shown in Table 2.4.1
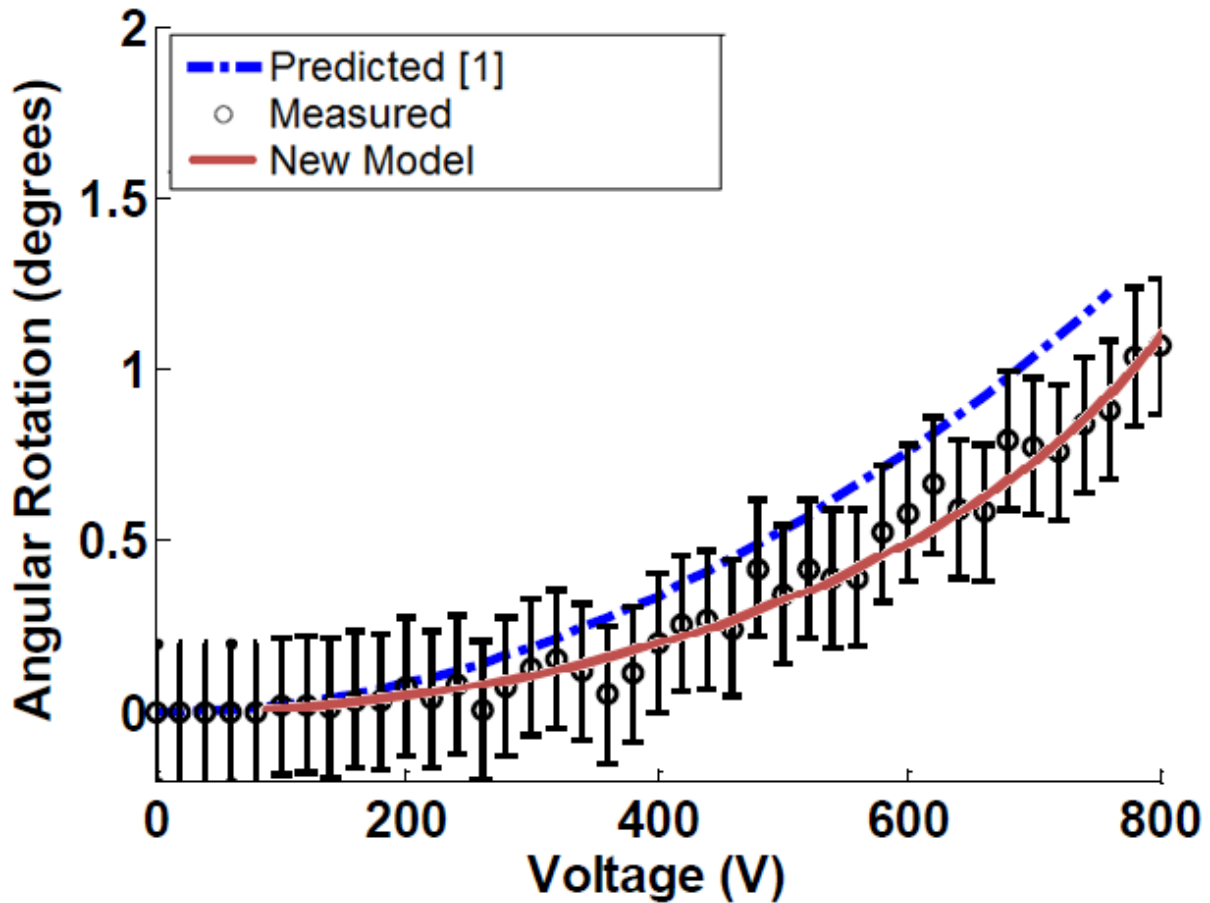
Figure 2.4.5: Measured and Predicted Operation of a Prototypic Steerable MEMS Platform

Variable	Description	Value	Source
A	Estimated Actuation Area (mm^2)	20.3	Estimated
A_{eff}	Effective Actuation Area (mm^2)	546.8	Calculated
Si_t	Thickness of Silicon Wafer (mm)	0.300	Design
ε_0	Vacuum Permittivity (F/m)	8.85E-12	Literature
F_s	Frame Spacing (mm)	1.000	Design
F_w	Internal Frame Width (mm)	0.100	Design
g	Actuation Pad Offset (mm)	0.550	Design
G	Sheer modulus of Si (GPa)	7.94E+10	Literature
H_l	Hinge Length (mm)	0.100	Design
H_s	Hinge Spacing (mm)	0.100	Design
H_w	Hinge Width (mm)	0.100	Design
J	Area Moment of Hinges (mm^4)	5.21E-06	Calculated
k_A	Actuation Area Fitting Coefficient	14.11	Fitted
k_r	Actuation Radius Fitting Coefficient	14.11	Fitted
P_t / H_t	Platform/ Hinge Thickness (mm)	0.050	Design
P_w	Antenna Platform Width (mm)	9.000	Design
r	Estimated Actuation Radius (mm)	3.150	Estimated
r_{eff}	Effective Actuation Radius (mm)	25.200	Calculated

Table 2.4.1: Values of Actuation Model Parameters for the Prototypic Steerable MEMS Antenna

A Modified Fourpoint antenna was used for prototype devices [1]. The design originated from a dissertation on new broadband antennas [20]. The fourpoint antenna described by [20] was modified to improve broadband impedance matching [1]. This antenna was selected because of its broadband impedance matching as well is its compact planar shape. The goal of [1] was to realize a broadband, high gain, steerable antenna. This was achieved by arraying together multiple omnidirectional Modified Fourpoint antennas.

Section 2.5 – Millimeter-Wave and THz Antennas

Until recently, the millimeter-wave (mm-wave) (30 – 100 GHz) and terahertz (THz) (0.1 – 100 THz) regions of the electromagnetic spectrum were only used for radio astronomy and military applications [4]. Otherwise, there was very little technology or research done in this area

to the point that it was referred to as the 'terahertz gap'. In recent years, a great deal of work has gone into developing technologies and applications to bridge the terahertz gap between microwaves and infrared regimes. The field is now too large to adequately summarize in this thesis so this literature review will focus on the antennas developed for the mm-wave and THz frequency regimes respectively.

One mm-wave frequency band has received significant attention in recent years for next generation wireless communications. The 57 − 66 GHz band is of global interest for broadband wireless communications and a great deal of work is being done in these areas. Ever increasing data transfer requirements for multimedia connectivity are making the IEEE802.11 wireless local area networks standards from 2.4 − 5 GHz obsolete. Multi-gigabit data transmission speeds can be achieved at mm-wave frequencies so this is of great interest to academia and industry. Developing the next generation of Wi-Fi is critical to keep up with modern optical high speed communication networks and user demand.

There is a demand for millimeter-wave antennas fabricated with CMOS processes to reduce hardware costs for use in consumer electronics such as Wi-Fi routers. At 60 GHz, the free space wavelength is 5 mm and the wavelength on a silicon chip is 2.5 mm due to the permittivity of silicon. This small size facilitates the integration of antennas with other RF subsystems and components onto a single chip. However, there are large amounts of substrate loss and inductive losses so that antennas have low efficiency (<10%) and negative gain. It is difficult to achieve high gain with on chip antennas and so the Yagi-Uda atenna is a common choice for 60 GHz antennas [38]. The Yagi-Uda antenna consists of a dipole in the proximity of parasitic elements; the reflector and directors. Standing waves between the driven and parasitic elements result in a directional antenna that can achieve high gain. Such a high-gain design is required to overcome

the losses in silicon. Work is currently being done to achieve -10.0 – 0.0 dB of gain at 60 GHz with CMOS processes [39, 40]. The noteworthy characteristic of these antennas is that their size can be scaled to achieve higher frequency operation as more mm-wave and THz sources, systems, and applications are developed in the future.

Another technique that is being developed for mm-wave applications is the reflectarray antenna which was first described in 1963 [41]. This antenna operates by reflecting an open-open air feed such as a horn antenna against a frequency selective surface (FSS). The FSS is made up of small unit cells that are electrically smaller than the incident wavelength. The unit cells are tuned to control the phase of the reflected radiation. By careful tuning of the entire FSS, the reflected wave can be controlled to have very high gain and any desired polarization. The element phase schematic and gain characteristics of a reflectarray antenna whose elements are tuned rectangular dielectric resonator antennas are shown in Figure 2.5.3 [42]. The reflectarray is very useful because high gain performance can be achieved at any frequency by scaling the reflecting elements. Another benefit is that the antenna is 'air-fed' meaning it is driven by a wave in space and not from a transmission line. This means that no impedance matching is necessary.

The THz spectrum has been shown to be excellent for molecular spectroscopy because the absorption energies correspond to transitions in rotational and vibrational modes of molecules. The radiation does not have enough energy to promote valence electrons and is therefore non-ionizing. The current and developing applications include explosives detection, toxic gas detection, mail and personnel screening, in-line pharmaceutical manufacturing inspection, semiconductor test and inspection, molecular spectroscopy, medical imaging, and cancer detection.

Antennas are very challenging to create at THz frequencies. Many designs used for RF antennas can be scaled down to operate in the THz regime where wavelength is on the order of microns. However, the materials must often be changed because losses are very high in traditional semiconductor substrate materials and metals. These losses get worse as frequency increases, which poses another challenge in creating efficient THz antennas. Dielectrics have low loss at high frequencies and are a common substrate choice. Sophisticated techniques must be used for generate and propagate THz radiation as well as to fabricate the hardware.

A cutting edge example of how the use of novel materials and fabrication techniques are used to achieve is the reconfigurable dipole array on graphene [43]. This design was studied numerically at 1 THz. Graphene, a single atomic layer of carbon, has many useful and unique properties. On such property is that its resistivity can be controlled by a gate voltage. With no applied field, graphene at room temperature has an incredible mobility of $200,000\frac{cm^2}{V*s}$ but its resistivity greatly increases as gate voltage increases above 10 V. The proposed antennas were dipole antennas made of 1 µm of gold on a single layer of graphene on a 300 nm of SiO_2 on a silicon substrate. By applying a gate voltage under an antenna, the resistivity of the substrate changed which in turn affected the radiation characteristics of the antenna. Simulations predicted > 40 dB of isolation between the ON and OFF states of the antenna. It was shown that selectively turning antennas in an array ON and OFF, it was possible to reconfigure the array characteristics without the need for complex current or phase control.

The CMOS Yagi-Uda antennas, DRA reflectarray antenna, and theTHz dipole on graphene antenna are just a few example of a growing field filled with complex problems and innovative solutions. The usefulness of the mm-wave THz spectrums will ensure this as a large area of research and growth for the next several decades.

Chapter 3: Mechanical Optimization

The main goal of mechanical optimization was to improve the ability of the steerable MEMS antenna platform to rotate. Three important metrics were used to characterize the mechanical performance of devices. The first metric was the maximum angle that can be achieved by actuation, hereafter referred to as actuation angle. The second metric was the electric potential required to achieve maximum actuation angle, hereafter referred to as actuation voltage. The last metric was the maximum angle that can be achieved before mechanical failure, hereafter referred to as failure angle. In this mechanical optimization study, the actuation angle and failure angle were maximized while the actuation voltage was minimized.

Four design variations were fabricated in [1] in an attempt to verify theoretical calculations and to help determine optimum device geometry. The performance of these devices serves as a benchmark for performance improvement in this thesis. It was theorized that 50 µm thick hinges would yield the best device performance. The hypothesis was verified with respect to the maximum failure angle but not with respect to the actuation angle. The measured performance of the four design variations are shown in Table 3.1.

Hinge Thickness	Max Actuation Angle	Max Actuation Voltage	Failure Angle
30 µm	4.0° ± 0.2°	800 V	7.5° ± 0.4°
50 µm	1.1° ± 0.2°	800 V	9.1° ± 0.4°
80 µm	0.6° ± 0.2°	800 V	8.4° ± 0.4°
100 µm	0.2° ± 0.2°	800 V	7.8° ± 0.4°

Table 3.1: Measured Mechanical Performance of Prototypic Devices

The antenna platform presented in [1] was studied and optimized, and is referred to in this thesis as the Generation 1 antenna platform (G1 platform). COMSOL was the chief tool used to study the mechanical performance of this device due to its complex behavior. This approach

yielded theoretical gains in mechanical performance. However, upon integrating the selected broadband antenna and feedline designs with the G1 platform, the designs were shown to be incompatible with each other (shown in Chapter 4). The broadband performance of the antenna was completely degraded after integration so the G1 design had to be reworked. There were additional issues with the mechanical operation of the G1 platform pertaining to device actuation which spurned its redesign.

Two additional generations of the steerable MEMS antenna platform were developed and optimized (Generations 2 and 3). The new designs were shown to integrate much better with broadband antenna designs. The updated designs also simplified the mechanical structure such that a closed form actuation prediction model was able to be developed to predict G2 and G3 platform performance. This simplification eliminated the need study the design with COMSOL which was desirable for greater confidence in theoretical results.

Section 3.1 – Generation 1 Antenna Platform

The initial efforts to optimize mechanical performance entailed modifying prototypic designs [1] and use numerical analysis to predict performance gains. The versions that are direct variations of the antenna platform design in [1] are referred to as the Generation 1 Antenna Platform.

Upon investigating the design equations presented in Section 2.6, it was determined that the simplest way to improve maximum rotation angle was to increase the torsion hinge length. A FEA model was created and parameterized with the major independent variables in the design. A schematic of the way the G1 platform was parameterized is shown in Figure 3.1.1. A table of the design parameters' descriptions and the range of values is shown in Table 3.1.1.
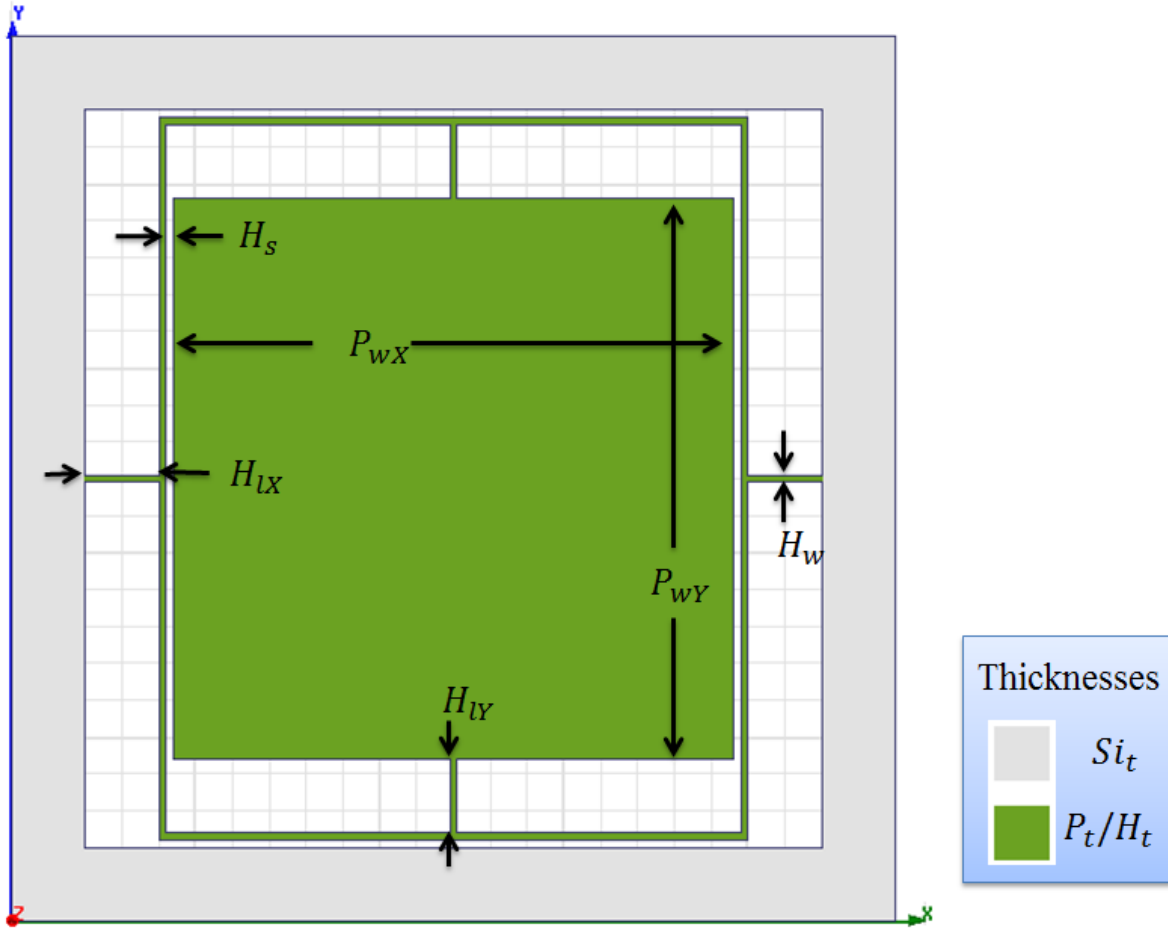
Figure 3.1.1: Schematic of the Generation 1 Steerable MEMS Antenna Platform

Parameter	Description	Values
H_{lX}	X Hinge Length	400 μm
H_{lY}	Y Hinge Length	10 mm
H_s	Hinge Spacing	10 mm
H_w	Hinge Width	100 μm
P_t/H_t	Platform / Hinge Thickness	100 - 2000 μm
P_{wX}	Platform Width in the X direction	100 - 2000 μm
P_{wY}	Platform Width in the Y direction	100 μm
Si_t	Silicon Substrate Thickness	0.300 mm

Table 3.1.1: Experimental Range of Values of Geometry Parameters for the
Generation 1 Antenna Platform

A FEA model was developed in COMSOL to study the behavior of the G1 antenna

platform. A closed form study was not developed because of the complex behavior of the

38

intermediate frame. To test actuation performance, the model rotated the antenna platform by setting a fixed displacement to the edges of the platform. The model was used to measure the stress in the torsion hinges as a function of rotation angle. A screenshot of the FEA model is shown in Figure 3.1.2.
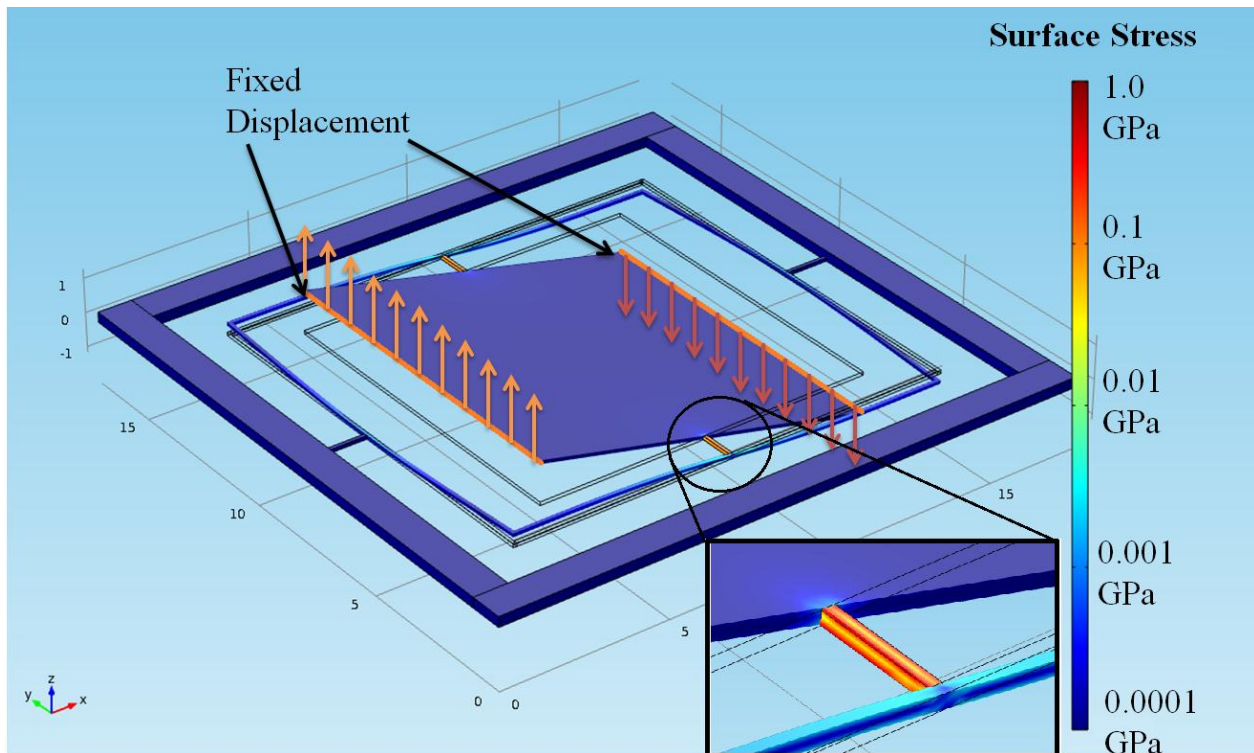
Figure 3.1.2: FEA Simulation of the Steerable MEMS Antenna Platform Showing Y-Axis Rotation and Stress in the Torsion Hinges

The FEA model was studied and its results confirmed by what was known from the closed descriptions of torsion hinge behavior. The torsion hinge length was inversely related to hinge stiffness. It was observed however that there was significant difference in performance under X-axis rotation versus Y-axis rotation. The model predicted that the Y-axis hinges were significantly stiffer than the X-axis hinges. The stress was measured in the hinges for 45° of rotation along the X and Y axis respectively for a range of hinge lengths and the results are shown in Figure 3.1.3.

39
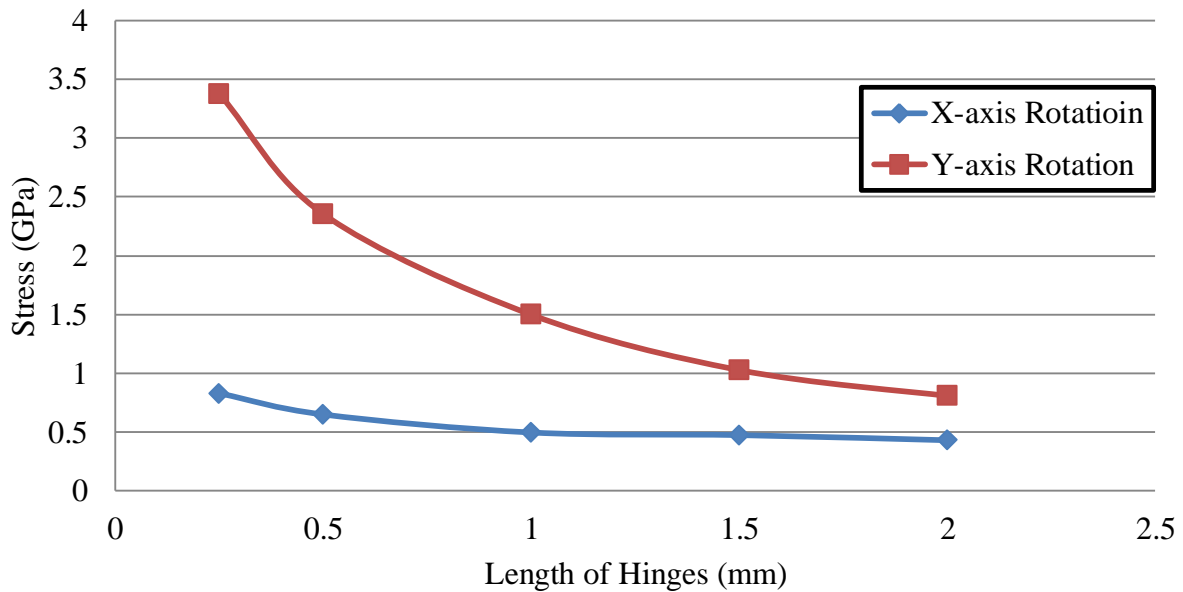
Figure 3.1.3: Stress in Unbalanced Hinges for 45° of Rotation about the X and Y axis for a Range of Hinge Lengths

The FEA model clearly predicted two to four times higher stress in the Y hinges over the X hinges. This was because the hinge structure and intermediate frame were not symmetric. This was undesirable for a practical device. It would be best if each hinge was of equal stiffness so that equal rotation could be achieved in about each axis. This was achieved by making the two hinge lengths asymmetric to compensate for the difference in stiffness of the two hinges.

The Y hinge was fixed at 2mm and the length of the X hinge was swept from $0.5 - 2.0$ mm. For each geometry variation, the model evaluated the stress in the hinges for $\pm 22.5°$ of rotation. This angle was selected as a target maximum achievable angle so that the device would be able to rotate through a 45° range of angles. The difference in the stress in the X and Y hinges respectively was evaluated. It was desirable that there was no difference in the hinge stress. This metric was evaluated as a function of the hinge length ratio, defined by the following expression.

$$Stress\ Missmatch = Sress\ in\ Y\ Hinges - Stress\ in\ X\ Hinges \qquad (3.1)$$

$$Hinge\ Length\ Ratio = \frac{H_{lX}}{H_{lY}} \tag{3.2}$$

The stress mismatch was calculated when the hinge length ratio was swept from $0.125 -$ 2.0 with a 0.125 step size, is shown in Figure 3.1.4 when $H_{lY} = 2\ mm$.
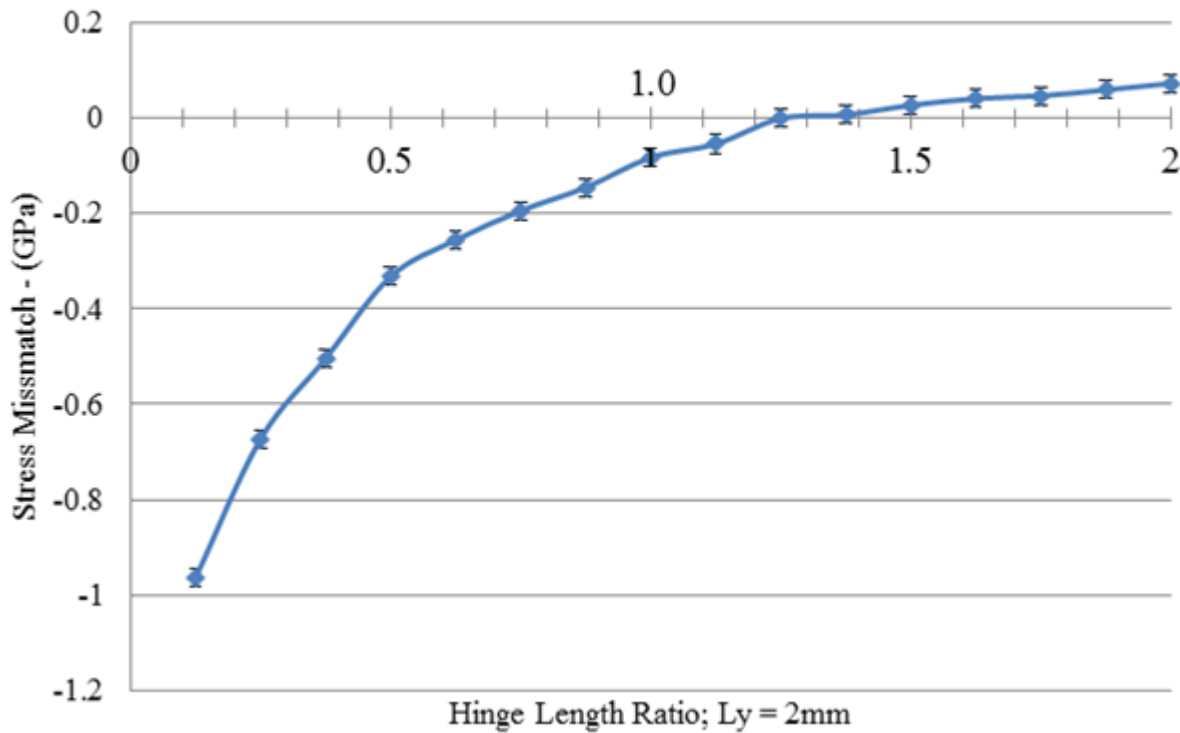
Figure 3.1.4: Maximum Strain in Hinges for Rotation about the Y-axis for Different Hinge Lengths

It was determined that the optimal hinge ratio for hinge balancing was 1.25. To verify this, the same analysis of the two hinges under rotation shown in Figure 3.1.3 was undertaken with the ideal hinge length ratio to verify equal hinge performance and is shown in Figure 3.1.5.
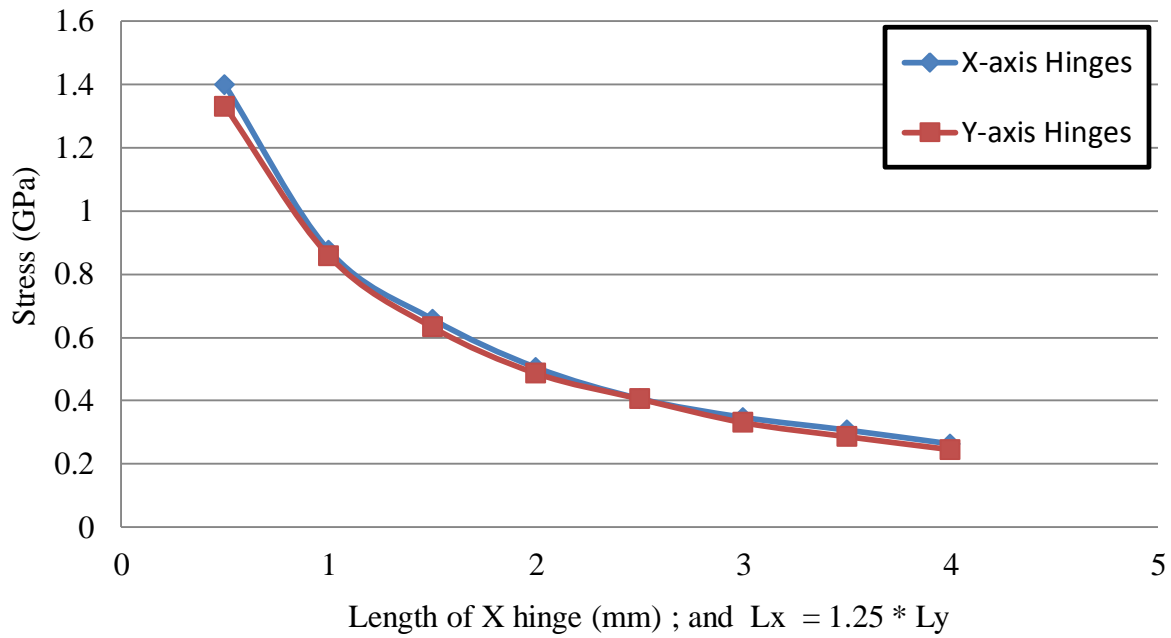
Figure 3.1.5: Strain in Balanced Hinges for 22.5° of Rotation about the X and Y axis for a Range of Hinge Lengths

In order to understand the stresses that devices were likely experience at mechanical failure, a study was undertaken to simulate the stress in prototypic devices at the point of mechanical failure. Four design variations were reported with different hinge thicknesses and their measured fracture angles [1]. Stress at fracture was calculated and the results are shown in Figure 3.1.6.
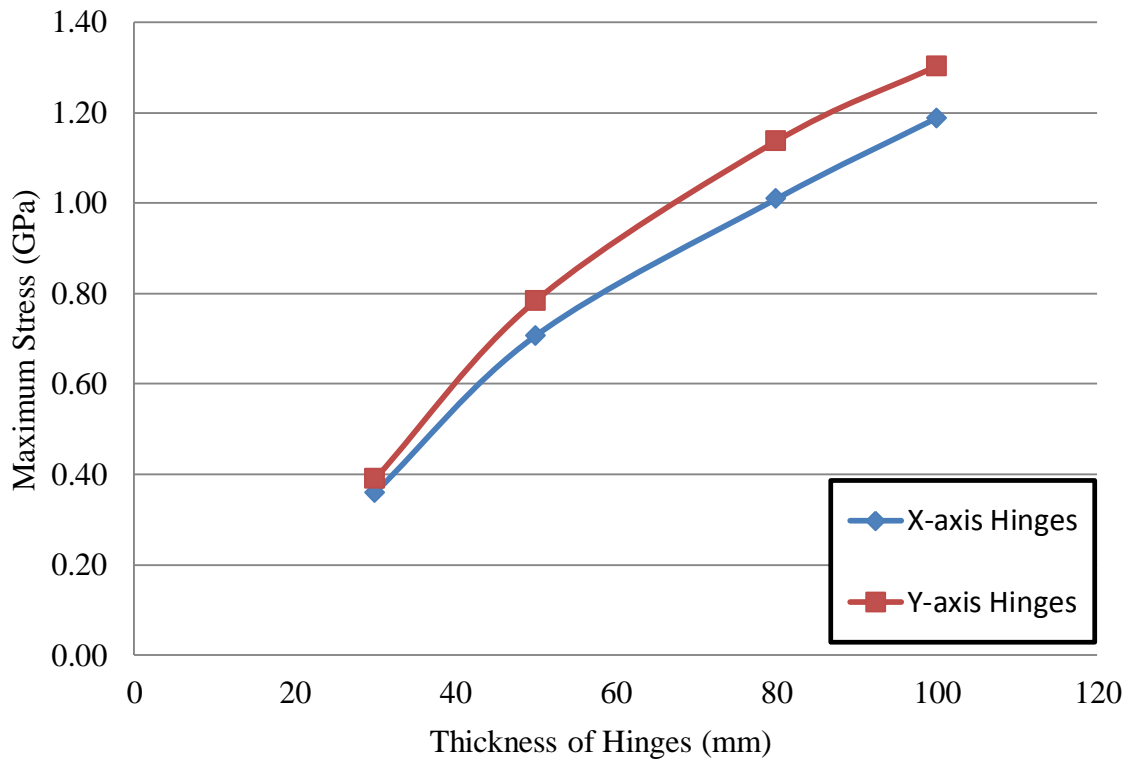
Figure 3.1.6: Stress in Hinges at Mechanical Failure Angles Reported by [1]

Failed devices tended to fracture where the hinges met the body of the device. This is predictable because this is where the stress concentration factor is highest. As shown by Figure 3.1.6, the fracture stress of silicon is dependent on device geometry and not just the materials used. The ultimate sheer strength of single crystal silicon is $1.0 - 1.3$ GPa [37, 44]. The fabricated devise with thicker (80 and 100 μm) hinges had lower stress concentrations than the thinner designs and were able to able to withstand more stress. The best performing device (100 μm thick hinges) had a square cross section and the smallest area moment, indicating that it should withstand the greatest stress due to symmetry.

From this analysis it was determined that for design purposes, stress should not exceed 1 GPa in practice to ensure good device operation and to avoid mechanical failure. It was

determined that the X hinges should be no less than 0.9 mm and a hinge length ratio of 1.25 observed for operation up to 22.5° in the G1 antenna platform.

Despite all the effort of balancing the hinges, the G1 antenna platform was found to be inadequate for final integration with an antenna. The reasons for this are described in the next section as well as Section 4.3.

Section 3.2 – Generation 2 Antenna Platform

The G1 antenna platform was redesigned for five reasons which are outlined in Figure 3.2.1. First, simulations predicted high return loss of the antenna during electrical simulations. This was attributed to the sharp right angle turns that the feedline had to make when crossing the hinges and intermediate frame. It is well known that sharp bends result in reflections in the transmission line. The G1 platform's intermediate frame was too narrow to accommodate 45° bends or swept bends. A requirement of the new G2 platform was to have more area to allow incorporation of 45° bends.
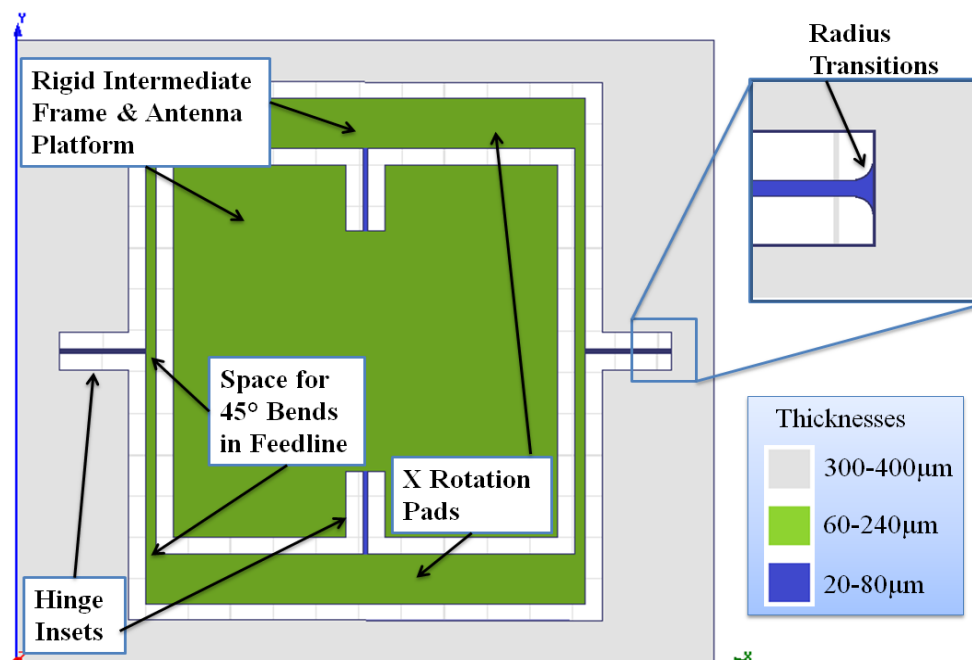
Figure 3.2.1: Top View of Generation 2 Steerable MEMS Antenna Platform with Design Updates

The second shortcoming of the G1 platform was its need for numerical analysis. When in operation, the hinges and intermediate frame were mechanically indeterminate. This meant that no closed form solution for how they deformed could be derived. This was a result of the fact that the intermediate frame and antenna platform were not rigid with respect to the hinges. A general design rule is that structures that are not designed to bend (intermediate frame and antenna platform) should be at least three times thick as structures that are engineered to flex or deform (hinges). A requirement of the G2 platform was that the antenna platform and intermediate frame had to be significantly more rigid than the hinges. By doing this, it was possible to assume all deformation took place as torsion in the hinges and thereby allowed for a closed form approximation to be developed.

The third motivation for redesigning the G1 platform was that the electrostatic actuation method was not equally efficient for all directions of rotation. It was shown in the previous section that unequal hinge lengths for rotation about the X and Y axis were necessary to have equal rotatability in each direction. Even with this design update, the electrostatic actuation pads were unable to pull on antenna platform with equal efficiency. For rotation about the Y axis, a capacitive force was applied to one side of the antenna platform. The reaction force to this stimulus was a torque in the Y axis hinges. This torque caused torsion in the Y hinges and thus a rotation of the antenna platform about the Y axis. For rotation about the X axis, a capacitive force was applied to the top or bottom of the antenna platform. The reaction forces must be transferred through the intermediate frame to the X hinges. The intermediate frame then became a secondary hinge in parallel with the X hinges. It would be much better for X actuation to be able to apply a force on the intermediate frame so that the reaction forces were only the torque in

45

the X hinges. For these reasons, a wide area was created in the intermediate frame for electrostatic action in the X direction. This extra region is referred to as the X Rotation Pad.

The fourth design update was to reduce the overall chip size by creating insets in the antenna platform and frame to accommodate the longer hinges required to achieve high operation angles. Additionally this reduced the required actuation voltage but decreased the necessary gap between device and actuation pads.

The last redesign was to improve maximum rotation of the platform before device failure. The transition between the frame and hinges in the prototypic devices were 90° corners. These sharp corners led to stress concentrations at the ends of the hinges. The stress concentration factor in silicon for 90° corners has been reported as high as 33 in literature and these areas were also the most common area for prototypic devices to fail. To reduce this design flaw, radius transitions between the frame and hinges were introduced.

The design updates required the addition of a second processing step and lithography mask in the prototypic process flow. In order to create hinges that are thinner than the antenna platform, a backside etch process is added to the fabrication. After the creation of the membrane through the anisotropic backside, the backside is patterned again with PR and a DRIE of the backside is performed. The areas between the frame, intermediate frame, and antenna platform, as well as the area under the hinges are etched to be 1/3 the thickness of the other elements. After the final DRIE release step, the hinges will be thinner than the antenna platform. This creates a rigid platform and intermediate frame with respect to the hinges to improve the predictability of the device.

A numerical experiment was undertaken to evaluate different hinge designs. A model of the hinge's behavior was constructed and studied. A schematic of how the G2 antenna platform's geometry was defined is shown in Figure 3.2.2.
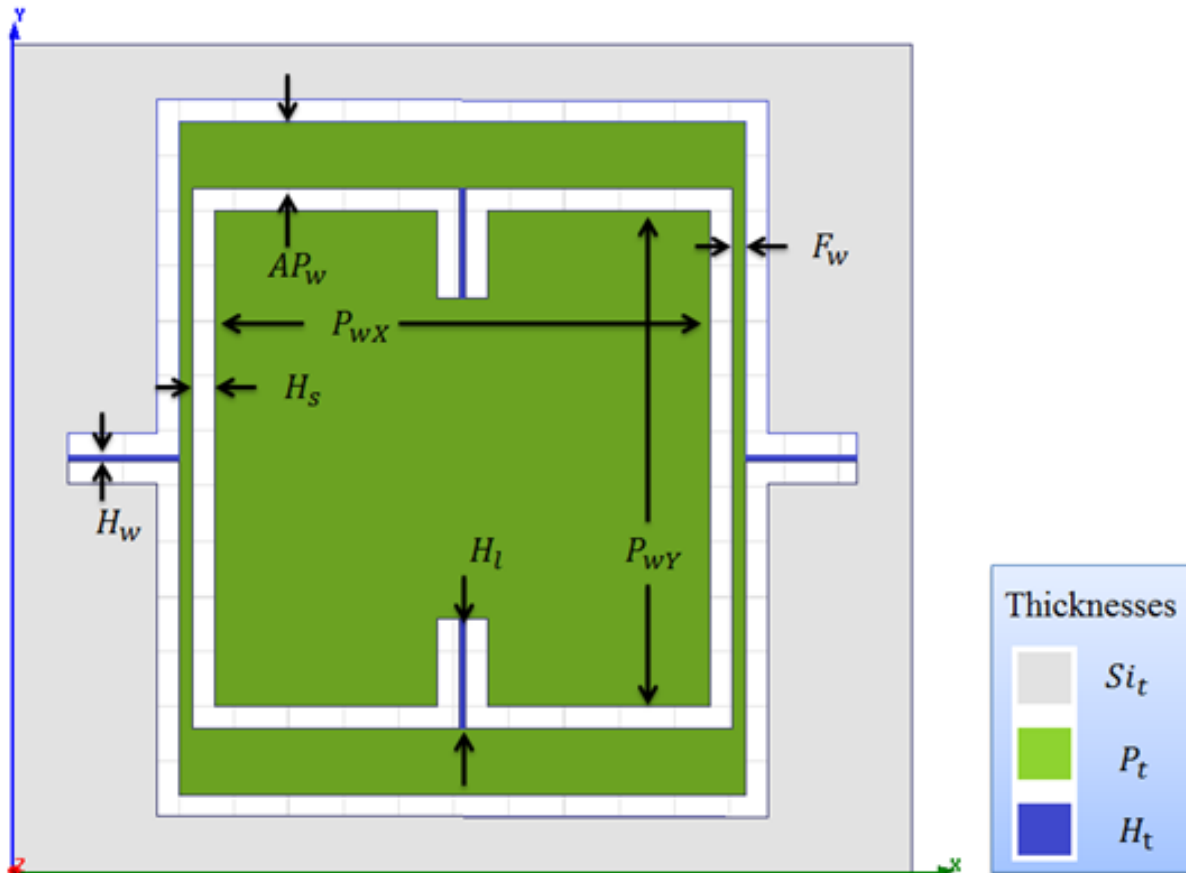
Figure 3.2.2: Schematic of the Generation 2 Steerable MEMS Antenna Platform

The effect of the thickness and length of hinges in the G2 MEMS antenna platform was studied for 16 hinge configurations. The effect of designs on the fracture angle as well as the critical voltage was studied. The fracture angle is self-explanatory; the angle at which hinges will mechanically fail. The critical voltage was calculated to be the voltage required to rotate the platform to its fracture angle with an appropriate actuation pad offset (this was also the pull in angle).

The hinges were treated as a rectangular torsion bar. The torque, T, in the hinges is related to the total angular twist by the Equation 3.1 where J is the second area moment of inertia of the hinge, G is the sheer modulus, θ is the amount of twist in radians, and H_l is the hinge length. This is the rotational equivalent of the Hooke's law.

$$T = \frac{J * G * \theta}{H_l} \tag{3.1}$$

The maximum sheer stress in the hinge is given by the following equation.

$$\tau = \frac{T * \sqrt{\left(\frac{H_w}{2}\right)^2 + \left(\frac{H_t}{2}\right)^2}}{J} \tag{3.2}$$

The two equations were equated by the torque, T and the resulting expression was derived.

$$\theta_{fracture} = \frac{\tau_u * H_l}{G * \sqrt{\left(\frac{H_w}{2}\right)^2 + \left(\frac{H_t}{2}\right)^2}} \tag{3.3}$$

$$\tau_u = 1.2 \pm 0.2 \ GPa \tag{3.4}$$

This expression was used to predict how far hinges could rotate before reaching a critical stress level. The value of G for silicon used in this model was 79.4 GPa [37]. The maximum allowable stress, or the ultimate sheer stress, τ_u, was reported in Section 3.1 as $1.0 - 1.3$ GPa [40] and this was the value used in this thesis. The average of this range was used in the model resulting in a maximum sheer stress of 1.15 ± 0.15 GPa. The angle at which this stress is reached is referred to as the fracture angle.

A 4 x 4 full factorial design of simulations was constructed to investigate the effect of hinge length and thickness upon the angle at which maximum sheer stress is reached as well as the voltage required to do this. The hinge length was parameterized from $500 - 2000$ μm in 500 μm steps. The hinge thickness was parameterized from $20 - 80$ μm in 20 μm steps. For this

48

design, an actuation model similar to that in Section 2.4 was developed to predict the voltage required to rotate the antenna platform to the fracture angle as well as the pull in angle. This voltage is referred to as the critical voltage. It was found by using Equation 2.15 with different values for the actuation area, radius, angle, and actuation pad offset. The area and radius were calculated in the following way.

$$A = [P_{wX} + 2 * (H_s + F_w)] * AP_w \tag{3.5}$$

$$r = \frac{P_{wY} - AP_w}{2} + H_s \tag{3.6}$$

An effective actuation area term was again used in the actuation model but the effective actuation radius is omitted since it was defined in the design. The value for k_A was the ideal value found in Section 2.4.

$$A_{eff} = k_A * A \tag{3.6}$$

The value for the actuation pad offset, g, was based on the fracture angle. Under electrostatic actuation, a device can travel 1/3 of g. This is known as the snap in point or pull-in angle. For each of the 16 hinge designs considered, the appropriate value of g was calculated so that the pull in angle was equal to the fracture angle and was referred to as the actuation pad offset for maximum rotation.

$$g_{MR} = 3 * r * \tan(\theta_{fracture}) \tag{3.8}$$

The final expression used to determine the voltage at the simultaneous fracture and pull-in angles in all 16 hinge design variations is shown in Equation 3.9.

$$V_{critical} = \sqrt{\frac{4 * G * J * \theta_{fracture}}{\varepsilon_0 * H_l * A_{eff} * r} \left(g_{MR} - r * \tan(\theta_{fracture})\right)^2} \tag{3.9}$$

The critical voltage is the theoretical voltage required to rotate the antenna platform to its fracture angle if the device was packaged such that pull-in would not occur. This was calculated

to give future designers an idea of the magnitude of voltage required to achieve maximum rotation.

The design of experiments and resulting fracture angles, actuation pad offsets for maximum rotation, and critical voltages for each of the sixteen hinge variations is shown in Table 3.2.1. The effect of hinge length and thickness on fracture angle is shown in Figure 3.2.3 and Figure 3.2.4 respectively. The effect of hinge length and thickness on critical voltage angle is shown in Figure 3.2.5 and Figure 3.2.6 respectively. The values of the parameter used in the predictive models are shown in Table 3.2.2.

Thinner hinges were shown to be desirable for large fracture angles. This effect was weak however and the data suggested that there were other significant factors in achieving high fracture angles. Longer hinges were shown to be desirable for large fracture angles. This effect was strong and the data suggested long hinges were critical in achieving high fracture angles. Thinner hinges were shown to be desirable for low critical voltages. This effect was strong and the data suggested thin hinges were critical in achieving low critical voltages. Shorter hinges were shown to be desirable for low critical voltages. The data also suggested that there were other significant factors in achieving low critical voltages.

Iteration Number	Hinge Length (μm)	Hinge Thickness (μm)	Fracture Angle (°)	Actuation Pad Offset for Max Rotation (mm)	Critical Voltage (V)
1	500	20	3.2 ± 0.4	1.2	159.3 ± 0.2
2	1000	20	6.4 ± 0.8	2.5	332 ± 1
3	1500	20	9.6 ± 1.3	3.9	536 ± 3
4	2000	20	12.9 ± 1.7	5.7	800 ± 9
5	500	40	2.9 ± 0.4	1.1	392.9 ± 0.3
6	1000	40	5.9 ± 0.8	2.3	814 ± 2
7	1500	40	8.8 ± 1.2	3.5	1297 ± 7
8	2000	40	11.8 ± 1.5	5.0	1890 ± 20
9	500	60	2.6 ± 0.3	1.0	601.2 ± 0.4
10	1000	60	5.2 ± 0.7	2.0	1236 ± 3
11	1500	60	7.8 ± 1.0	3.1	1943 ± 8
12	2000	60	10.4 ± 1.4	4.3	278 ± 20
13	500	80	2.3 ± 0.3	0.9	759.2 ± 0.5
14	1000	80	4.6 ± 0.6	1.7	1550 ± 3
15	1500	80	6.9 ± 0.9	2.7	2411 ± 8
16	2000	80	9.2 ± 1.2	3.7	3390 ± 20

Table 3.2.1: Design of Experiments and Predicted Fracture Angle for 16 Hinge Variations of the G2 MEMS Antenna Platform
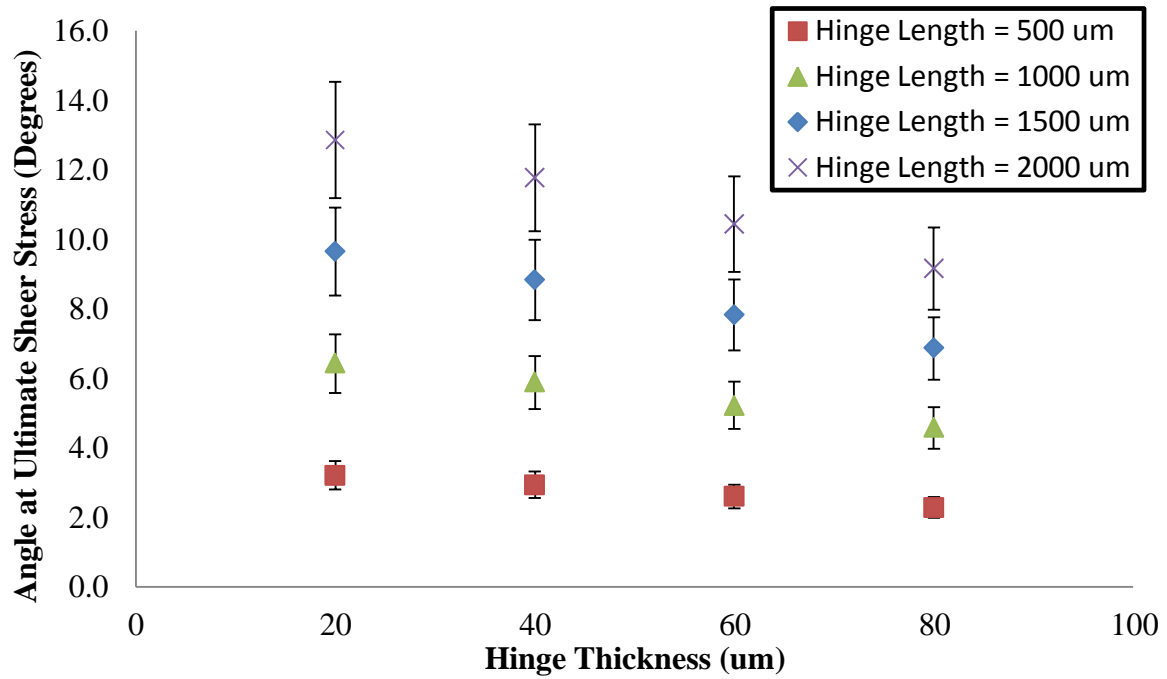
Figure 3.2.3: Hinge Rotation as a Function of Hinge Thickness for the G2 Hinges
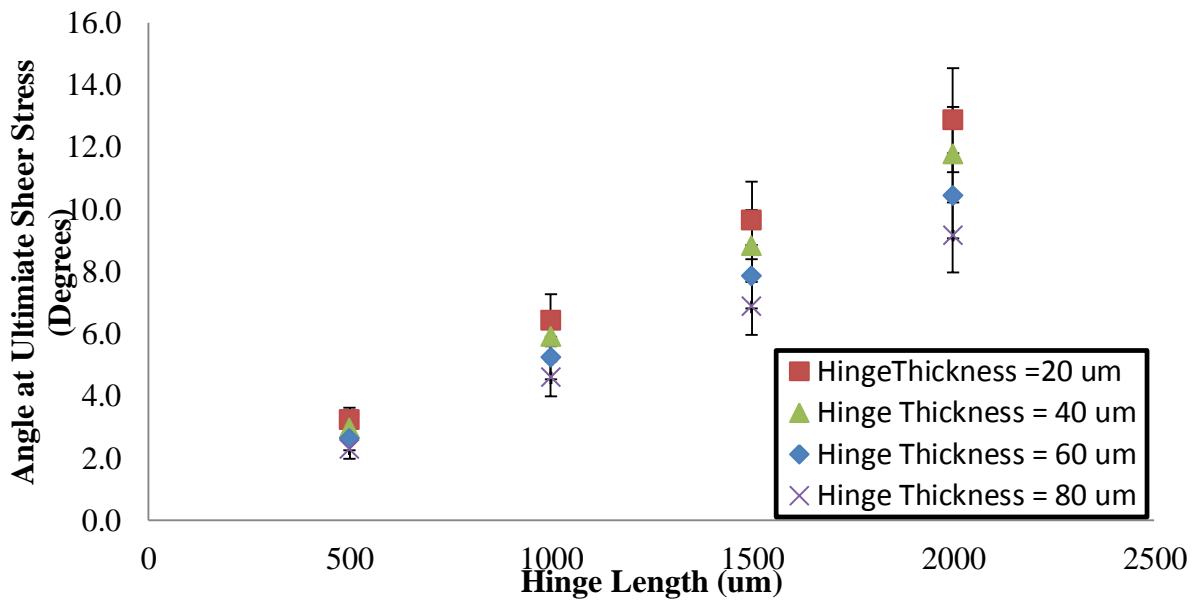
Figure 3.2.4: Hinge Rotation as a Function of Hinge Length for the G2 Hinges

52
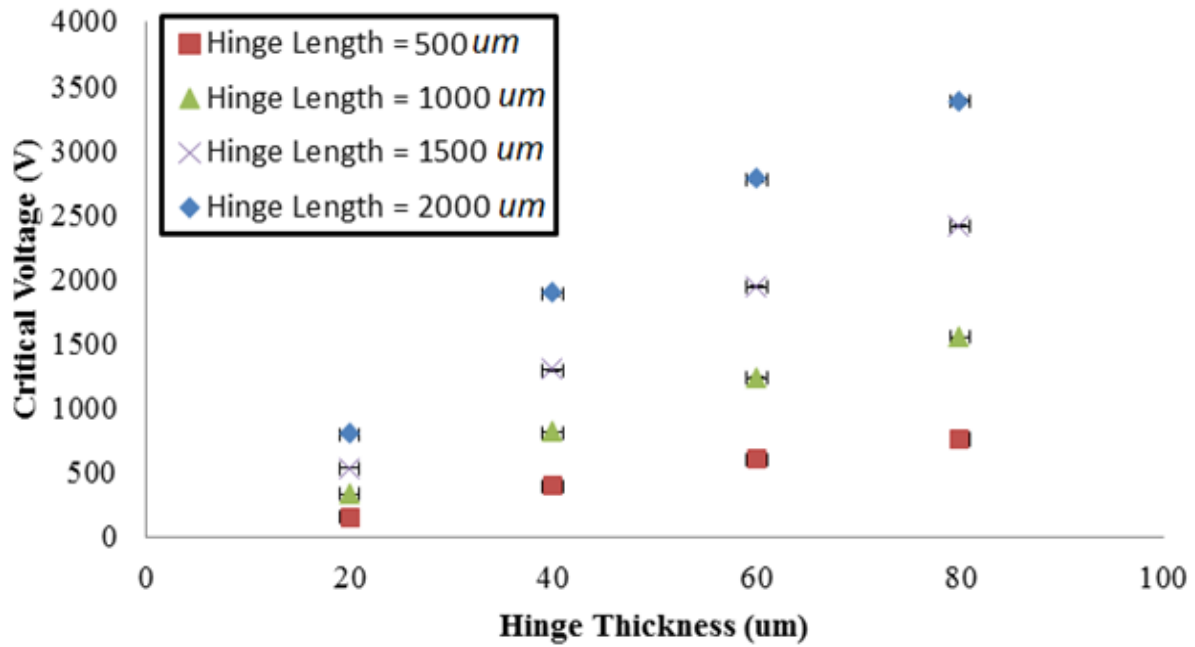
Figure 3.2.5: Critical Voltage as a Function of Hinge Thickness for the G2 Hinges

Figure 3.2.6: Critical Voltage as a Function of Hinge Length G2 Antenna Platform

Variable	Description	Value	Source
A	Actuation Area (mm^2)	52.0	Calculated
A_{eff}	Effective Actuation Area (mm^2)	733.72	Calculated
AP_w	Actuation Paddle Width (mm)	4.000	Design
ε_0	Vacuum Permittivity (F/m)	8.85E-12	Literature
F_w	Internal Frame Width (mm)	0.250	Design
G	Sheer modulus of Si (Pa)	7.94E+10	Literature
H_s	Hinge Spacing (mm)	0.100	Design
H_w	Hinge Width (mm)	0.076	Design
k_A	Fitting variable for Actuation Area	14.110	Fitted
P_t	Platform Thickness (mm)	0,06	Design
P_{wX}	Platform Width in X (mm)	1.30E+01	Design
P_{wY}	Platform Width in Y (mm)	10.000	Design
r	Actuation Radius (mm)	7.100	Calculated
Si_t	Thickness of Silicon Substrate (mm)	0.300	Design

Table 3.2.2: Parameters for the Generation 2 Antenna Platform and Actuation Model

The G2 designs presented have predicted max operating angles ranging from 2.3 – 13° with operating voltages ranging from 160 – 3390 V. Multiple design variations of the G2 antenna platform were simulated presented because there was no 'best case device' without an application. To determine the 'best' design would require a specific application to provide specific design goals. It is unlikely that maximum operating angle or voltage will be the only design metrics that are important for any one application so the cost and benefit of achieving an operation angle must be carefully weighed. In general, the greater the maximum operating angle, the less mechanically robust the design becomes.

Section 3.3 – Generation 3 Antenna Platform

The G2 antenna platform turned out to still have its limitations for being able to integrate an antenna and feedline. The resulting antennas that were studied still suffered because of the

multiple turns the feedline had to navigate as well as multiple times it had to traverse a hinge. For this reason, a third antenna platform was developed to accommodate this issue. The Generation 3 antenna platform was different from all the others because it was only able to rotate in one dimension. This reduction in mechanical performance turned out to be very helpful in designing a good antenna for integration with the antenna platform. A schematic of the G3 antenna platform and how it was parameterized is shown in Figure 3.3.1.
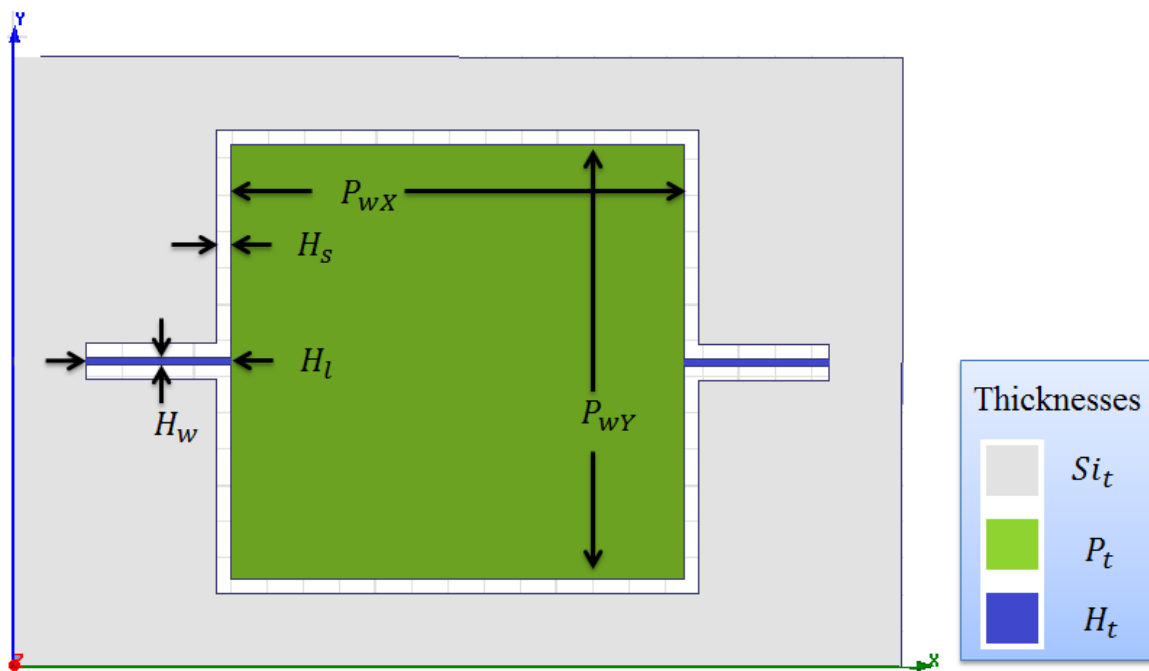
Figure 3.3.1: Schematic of the Generation 3 Steerable MEMS Antenna Platform

The model used in Section 3.2 had to be modified slightly. The G3 MEMS antenna platform had different actuation widths and radii than previous G2 designs. The new expressions for these variables are shown in Equation s 3.10 and 3.11.

$$A = \frac{P_{wY} * P_{wY}}{2} \tag{3.10}$$

$$r = \frac{P_{wY}}{2} \tag{3.11}$$

An effective actuation area term was again used in the actuation model but the effective actuation radius was omitted since it was defined in the design. The value for k_A was the ideal value found in Section 2.4.

$$A_{eff} = k_A * A \tag{3.12}$$

These expressions were used with Equations (3.3), (3.8), and (3.9) to predict the fracture angles and critical voltages for the G3 hinges. The same 4X4 design of experiments was undertaken to simulate the effect of hinge length and thickness on these two output variables.

The design of experiments and resulting fracture angles, actuation pad offsets for maximum rotation, and critical voltages for each of the sixteen hinge variations is shown in Table 3.3.1. The effect of hinge length and thickness on fracture angle is shown in Figure 3.3.2 and Figure 3.3.3 respectively. The effect of hinge length and thickness on critical voltage angle is shown in Figure 3.3.4 and Figure 3.3.5 respectively. The values of the parameter used in the predictive models are shown in Table 3.3.2.

Thinner hinges were shown to be desirable for large fracture angles. This effect was weak however and the data suggested that there were other significant factors in achieving high fracture angles. Longer hinges were shown to be desirable for large fracture angles. This effect was strong and the data suggested long hinges were critical in achieving high fracture angles. Thinner hinges were shown to be desirable for low critical voltages. This effect was strong and the data suggested thin hinges were critical in achieving low critical voltages. Shorter hinges were shown to be desirable for low critical voltages. The data also suggested that there were other significant factors in achieving low critical voltages.

Iteration Number	Hinge Length (μm)	Hinge Thickness (μm)	Fracture Angle (°)	Actuation Pad Offset for Max Rotation (mm)	Critical Voltage (V)
1	500	20	3.2 ± 0.4	0.7	229 ± 5
2	1000	20	6.4 ± 0.8	1.4	480 ± 10
3	1500	20	9.6 ± 1.3	2.2	760 ± 20
4	2000	20	12.9 ± 1.7	3.2	1120 ± 30
5	500	40	2.9 ± 0.4	0.6	560 ± 10
6	1000	40	5.9 ± 0.8	1.3	1160 ± 30
7	1500	40	8.8 ± 1.2	2.0	1840 ± 50
8	2000	40	11.8 ± 1.5	2.8	2700 ± 100
9	500	60	2.6 ± 0.3	0.6	860 ± 20
10	1000	60	5.2 ± 0.7	1.1	1770 ± 40
11	1500	60	7.8 ± 1.0	1.7	2800 ± 100
12	2000	60	10.4 ± 1.4	2.4	2900 ± 100
13	500	80	2.3 ± 0.3	0.5	1090 ± 20
14	1000	80	4.6 ± 0.6	1.0	2200 ± 100
15	1500	80	6.9 ± 0.9	1.5	3400 ± 100
16	2000	80	9.2 ± 1.2	2.1	4800 ± 100

Table 3.3.1: Design of Experiments and Predicted Fracture Angle for 16 Hinge Variations of the G3 MEMS Antenna Platform
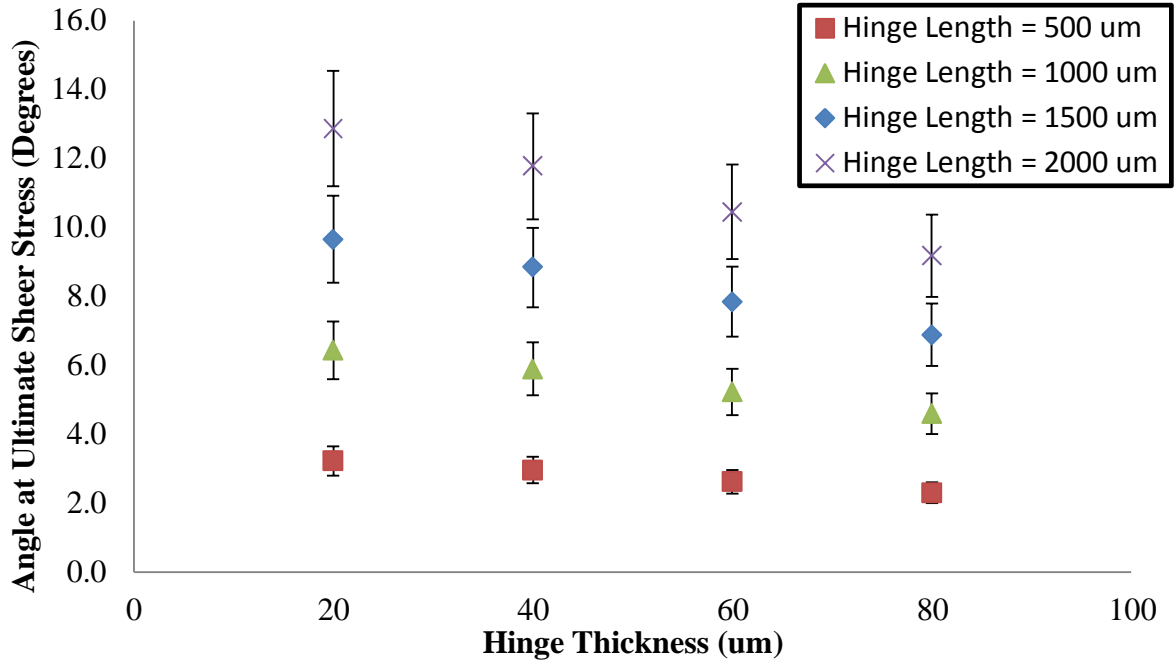
Figure 3.3.2: Hinge Rotation as a Function of Hinge Thickness for the G3 Hinges
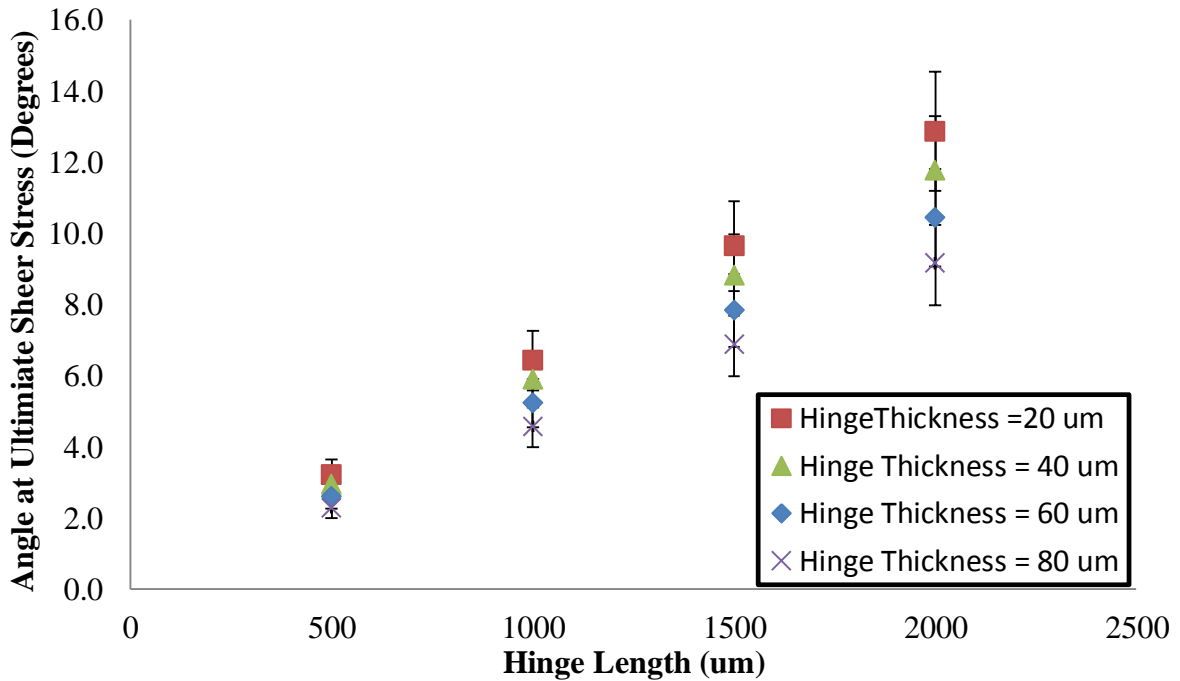
Figure 3.3.3: Hinge Rotation as a Function of Hinge Length for the G3 Hinges
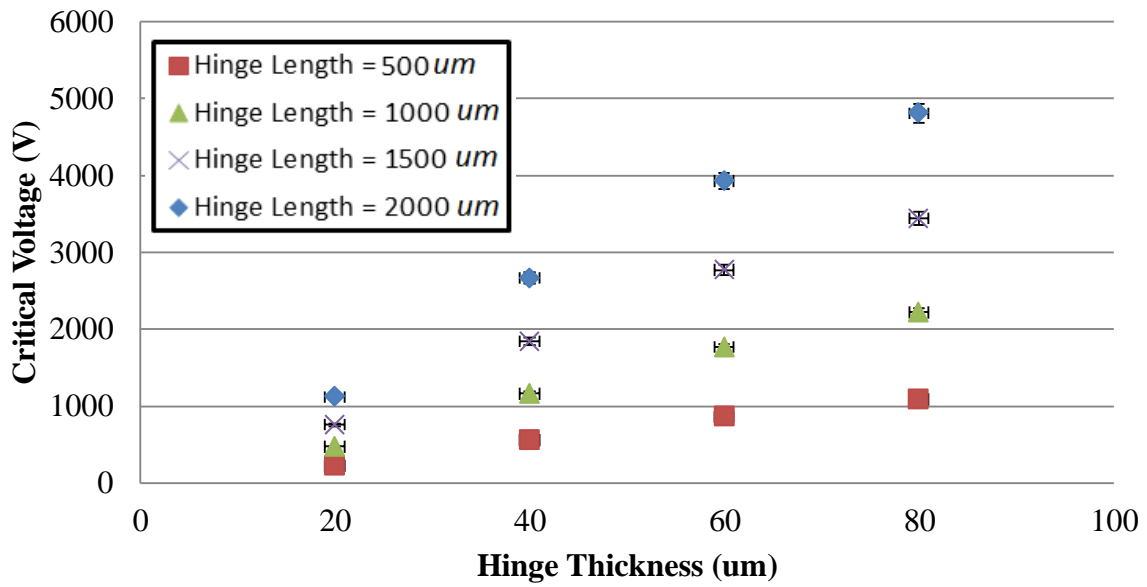
Figure 3.3.4: Critical Voltage as a Function of Hinge Thickness for the G3 Hinges
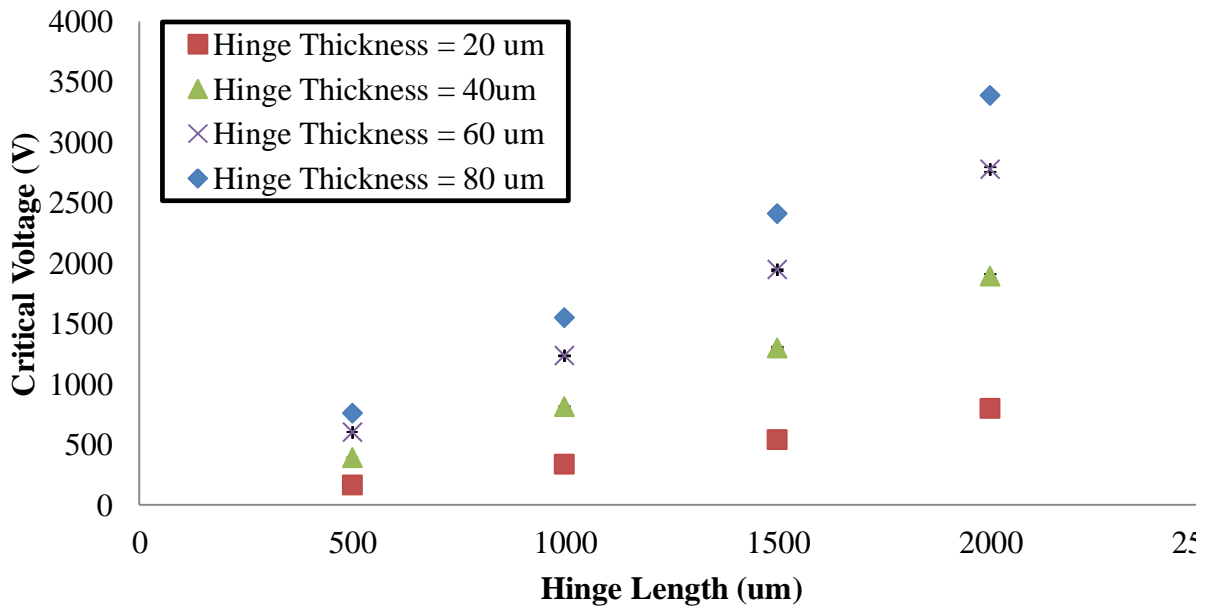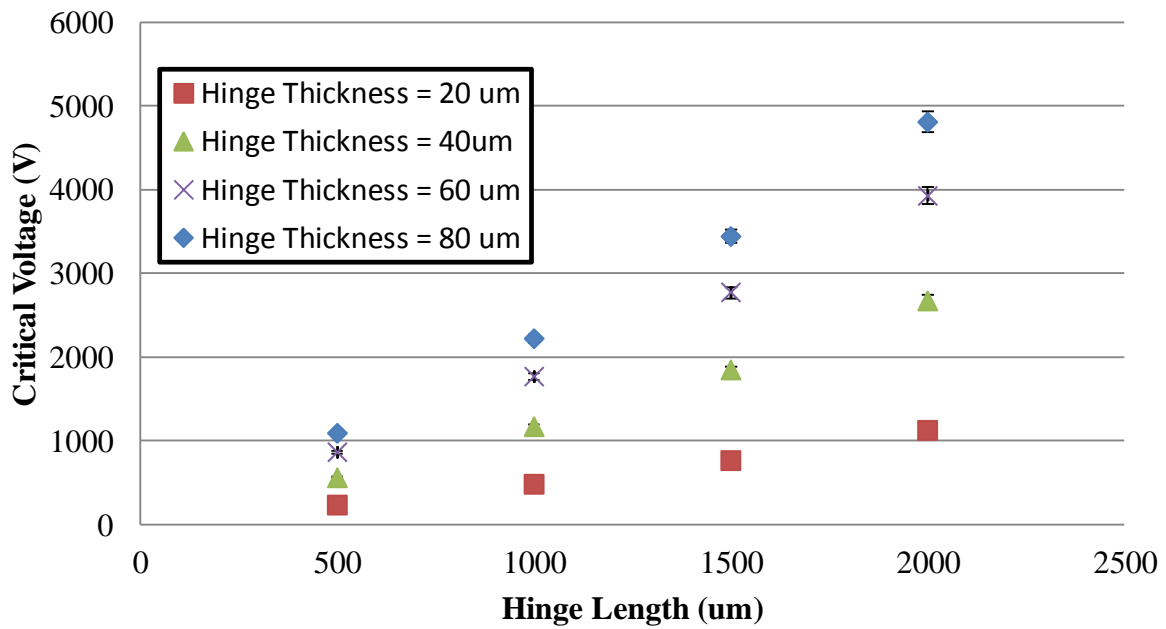

Figure 3.3.5: Critical Voltage as a Function of Hinge Length for the G3 Hinges

Variable	Description	Value	Source
A	Actuation Area (mm^2)	24.000	Calculated
A_{eff}	Effective Actuation Area (mm^2)	338.640	Calculated
ε_0	Vacuum Permittivity (F/m)	8.85e-12	Literature
G	Sheer modulus of Si (Pa)	7.94e10	Literature
H_s	Hinge Spacing (mm)	0.100	Design
H_w	Hinge Width (mm)	0.076	Design
k_A	Fitting variable for Actuation Area	14.110	Fitted
P_{wX}	Platform Width in X (mm)	8.000	Design
P_{wY}	Platform Width in Y (mm)	8.000	Design
r	Actuation Radius (mm)	3.000	Calculated
Si_t	Thickness of Silicon Substrate (mm)	0.300	Design

Table 3.3.2: Parameters for the Generation 3 Antenna Platform and Actuation Model

The G3 designs presented have predicted max operating angles ranging from 2.3 – 13° with operating voltages ranging from 229 – 4800 V. Multiple design iterations of the G3 antenna platform were simulated as in the preceding section because there is no 'best case device' without an application. The major drawback of the G3 platform over the G2 platform is its limitation of only one direction of rotation. The advantage of lower actuation voltages and ease of integration with an antenna make this design attractive.

Chapter 4: Electrical Optimization

The chief goal of electrical optimization was to make performance gains in the useable bandwidth of the steerable MEMS antenna. The prototype device built by [1] had a bandwidth of $1.55 \pm .02$, which is the benchmark for improvement. Three conditions must be met for an antenna to be considered operational at a specific frequency; beam shape (application dependent), antenna gain (application dependent), and impedance matching, which is demonstrated by a low return loss (< -10 dB). Since no application was considered, beam shape and antenna gain were reported but not used in the optimization of designs. The goal of this work was to design antennas that can be integrated with the steerable antenna platform and have the largest bandwidth possible. An antenna is considered 'broadband' when the bandwidth is greater than 2. An antenna was selected and optimized by itself without an antenna platform and hinge structure. The impedance bandwidth was maximized during optimization and the resulting antenna also showed good gain bandwidth and beam pattern bandwidth. A 1600% reduction in antenna performance was observed upon initial integration so antennas were integrated with multiple antenna platforms (G1 − G3). Additionally, two dielectric resonator antennas were integrated with the G3.

Section 4.1 – Teardrop Planar Inverted Cone Antenna Optimization

It was necessary to optimize the shape, feed lines, and substrate of the Td-PICA before integration with the antenna platform. Bandwidth was expected to be decreased from an ideally optimized antenna to the final steerable MEMS antenna. This was due to two chief factors: the addition of the meandering path transmission line introducing signal reflections and the variations in silicon substrate thickness between the die edge, hinges, and antenna platform changing the transmission line's behavior. Optimization was important not only to achieve an

optimized antenna shape but also to provide the necessary constraints to fully specify the antenna platform.

This study is best described as a variational analysis for performance enhancement. This form of optimization involves maximizing or minimizing a performance metric as a function of N input parameters. The performance metric was the operational bandwidth of the antenna. Five input parameters were selected in this thesis for antenna optimization. The parameters were iterated and the bandwidth performance evaluated for each case. Upon sweeping one variable, the best case was adopted into the design so that the gains made in the variational analysis were preserved and built upon. It was understood this would not ensure a global maximum in performance but would provide a good local optimization with minimal computation resources.

To optimize the Td-PICA, a fully parameterized model was constructed in HFSS that was studied extensively. More data was collected than is presented in this thesis. The optimizations shown represent the most successful and useful results obtained. Excluded investigations include introduction of self-similar slots as in fractal patch antennas, introduction of various ground planes, and introduction of passive elements. None of these investigations produced gains in performance. The results shown here were the steps taken to increase antenna performance over previous designs.

The five antenna parameters, W, F, G, S, and AWZ, were broken into three groups which described the following design features: antenna shape, transmission line, and substrate. As described above, W described antenna shape and this was the first parameter to be studied. The design with the best case was then used as the basis for the next study which was to optimize the transmission line. For this study F, G, and S were concurrently varied. The third study re-optimized the antenna shape and lastly the substrate was optimized.

The first parameter *W* was parametrically swept and the return loss was analyzed. The return losses of four representative cases are shown in Figure 4.1.1.

Figure 4.1.1: Return Loss of the Teardrop Planar Inverted Cone Antenna referenced to 100 Ω after the First Parametric Sweep of W; *L = 6.2mm, F = 25μm, G = 100 μm, S = 5 μm, AWZ*

Only minor gains in bandwidth were seen in the first sweep of *W*. The *W = 1.0* case was the unmodified shape presented by Suh [20] and had a bandwidth ratio of 6.62 ± 0.01, which was the lowest bandwidth of the four cases shown in Figure 4.1.1. This bandwidth was considered the benchmark for antenna improvement. The *W = 0.5* case was selected as the best case because it had the best return loss since it has the lowest return loss over the widest range of frequencies. The *W = 0.25* case had similar bandwidth but did not have as low of return loss over a wide range of frequencies. The *W = 0.75* case was rejected for the same reason. The bandwidth of the

best case in the first parametric sweep of *W* was 7.9 ± 0.1 which is a 20% increase from the initial Td-PICA shape.

The second study concurrently optimized all three transmission line design variables in a full factorial experimental design. The ranges were selected based on the geometric constraints from the antenna platform design and the calculated characteristic impedance of the resulting transmission lines. The full factorial experimental design is shown in Table 4.1.1.

Expt	F (μm)	S (μm)	G (μm)	Z_o (Ω)	Bandwidth
1	7.5	10	7.5	73.4	6.9
2	10.0	10	7.5	68.3	7.2
3	12.5	10	7.5	64.7	7.5
4	7.5	15	7.5	84.0	5.8
5	10.0	15	7.5	78.5	7.6
6	12.5	15	7.5	74.5	7.0
7	7.5	20	7.5	92.1	8.1
8	10.0	20	7.5	86.3	11.1
9	12.5	20	7.5	82.1	7.9
10	7.5	26	7.5	99.8	7.5
11	10.0	26	7.5	93.9	6.5
12	12.5	26	7.5	89.4	10.8
13	7.5	10	17.5	69.2	4.2
14	10.0	10	17.5	63.9	7.7
15	12.5	10	17.5	60.0	8.2
16	7.5	15	17.5	78.9	5.6
17	10.0	15	17.5	73.2	7.4
18	12.5	15	17.5	69.0	7.7
19	7.5	20	17.5	86.3	7.2
20	10.0	20	17.5	80.3	8.0
21	12.5	20	17.5	75.9	8.0
22	7.5	26	17.5	93.4	7.6
23	10.0	26	17.5	87.3	6.8
24	12.5	26	17.5	82.7	12.0

Table 4.1.1: Experimental design for parametric study of
Transmission line geometries

It was expected that there would be ideal transmission line impedance for good bandwidth but this was not observed. There was also no correlation observed between calculated transmission line impedance and observed impedance bandwidth. The results for all 24 cases simulated are shown in Figure 4.1.2.
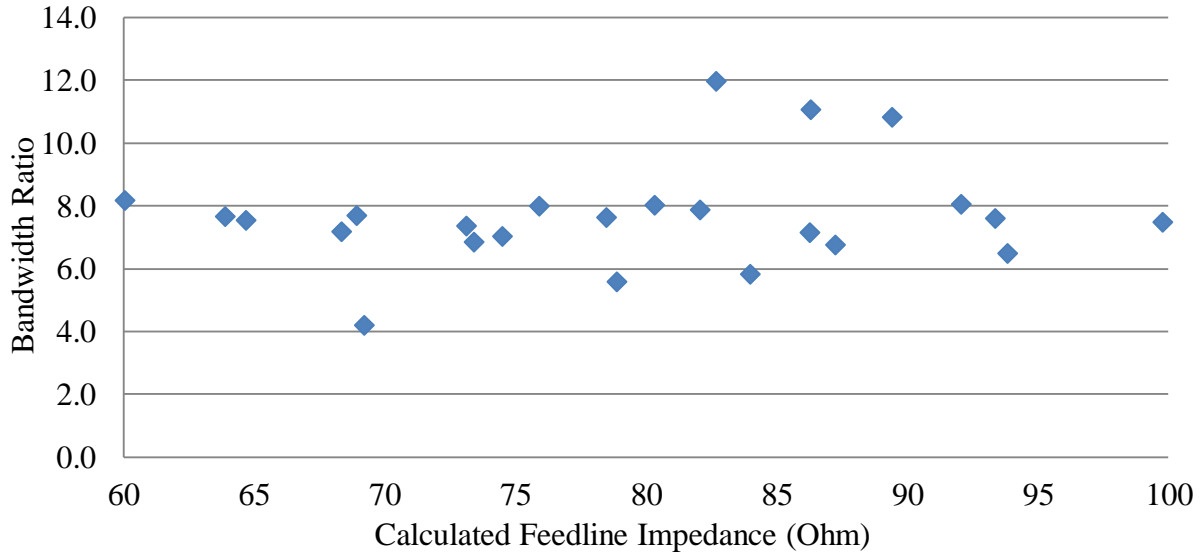
Figure 4.1.2: Bandwidth Ratio of Teardrop Planar Inverted Cone Antenna without Antenna Platform as a function of Transmission Line Impedance – Note: error is smaller than point markers

Experiment number 8 was selected as the best case result because of its high bandwidth as well as its narrow size. While experiment 24 had better performance, its width was deemed too great to integrate with the antenna platform design which required a narrow transmission line. The resulting bandwidth after the transmission line optimization was 10.4 ± 0.2 which was a 31% increase from before optimization and a 57% increase from the initial Td-PICA shape.

There was a great deal of variance in the results obtained in the first sweep of W study. After the transmission line was optimized it was decided to reinvestigate the validity of the first sweep of W since the system was not behaving in a stable manner. A very small change in the

value of *W* resulted in significantly different plots of return loss, the primary dependent variable in these studies.

A second sweep of *W* was conducted and the gains made in the transmission line optimization were obvious. The resulting antenna behaved much more stably as is shown in the parametric sweep results shown in Figure 4.1.3
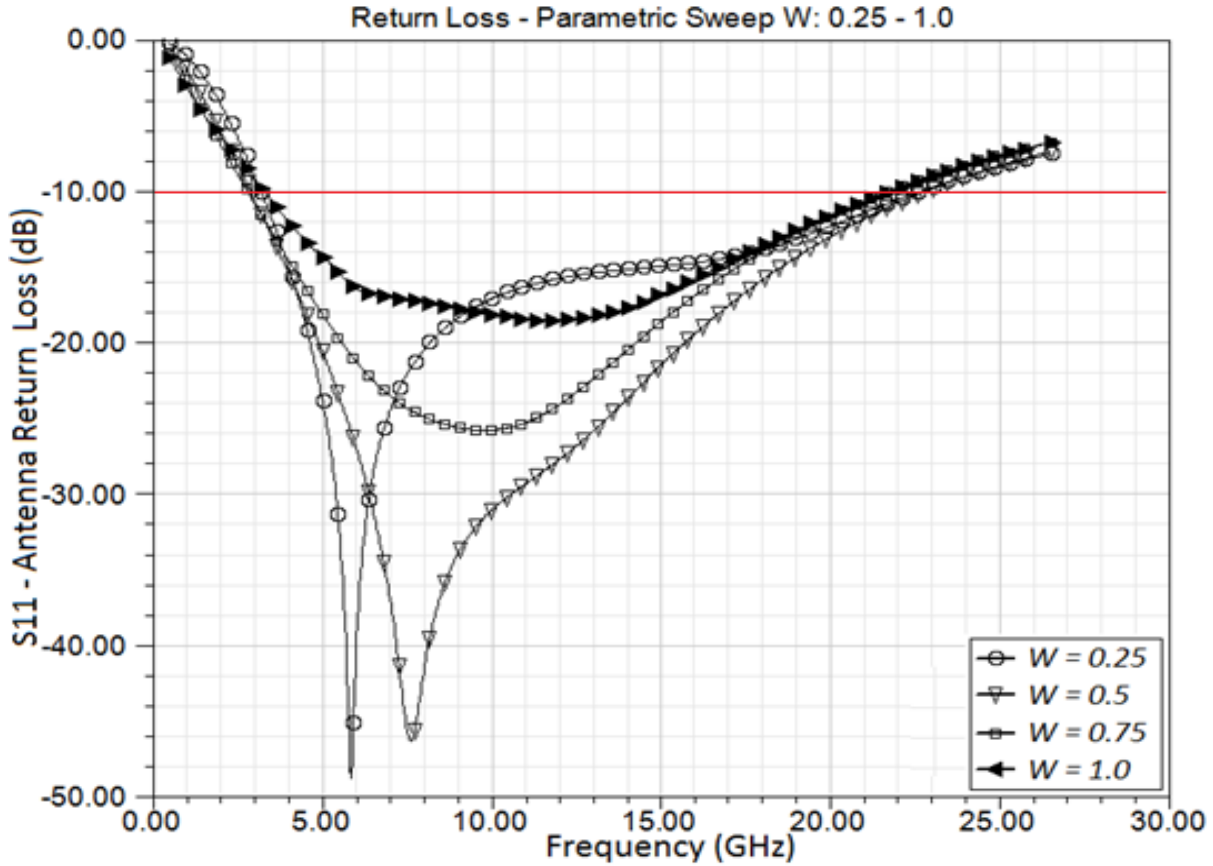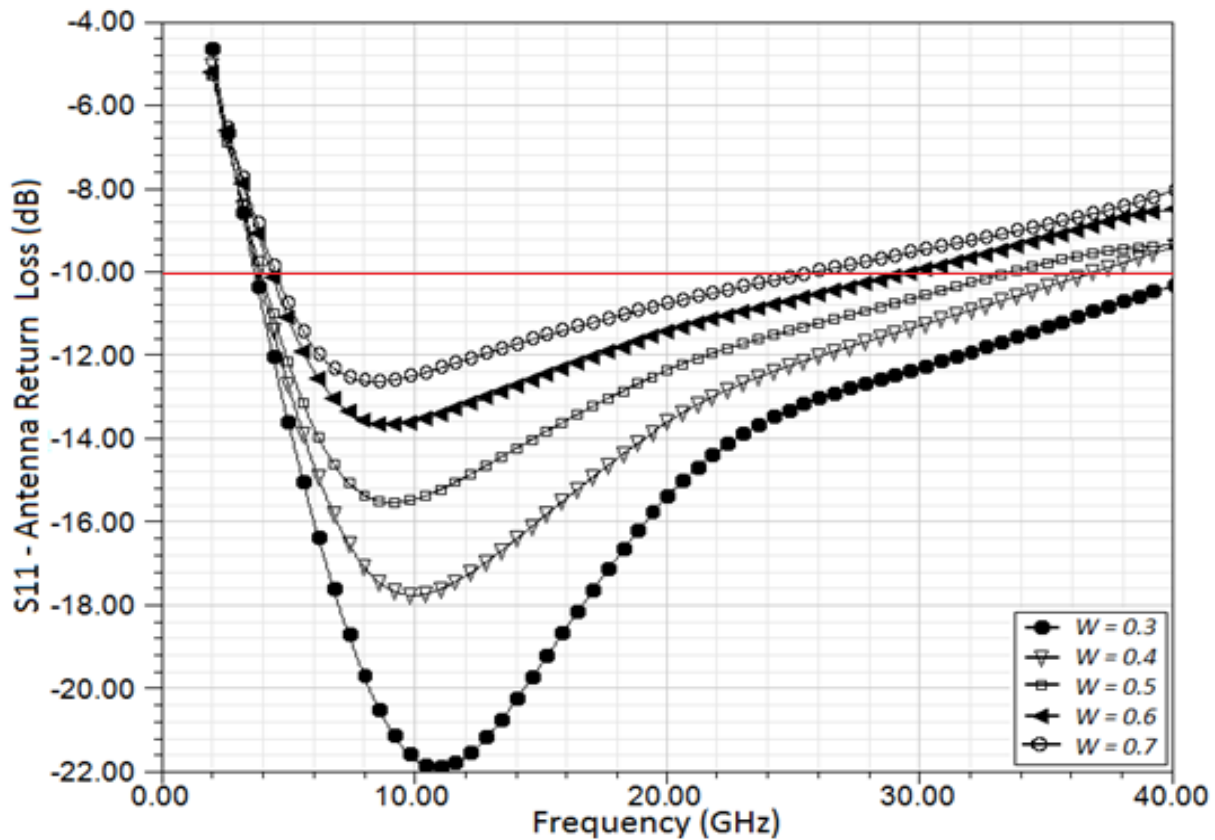

Figure 4.1.3: Return Loss of the Teardrop Planar Inverted Cone Antenna referenced to 100 Ω after the Second Parametric Sweep of W; *L = 6.2 mm, F = 10μm, G = 7.5 μm, S = 20 μm,*

The second parametric sweep of *W* was important to demonstrate that the antenna behaved in a more stable manner after the transmission line optimization and to validate the design decision to narrow the antenna shape. The best case was observed when *W = 0.3*, which resulted in a bandwidth of 11.4 ± 0.1. This bandwidth represented a 10% gain from the previous transmission line optimization and 70% gain from the initial Td-PICA shape.

66

The last optimization was to sweep the variable *AWZ* to achieve final tuning of the antenna. The feasible range of this variable was a determinate of the materials used for fabrication as well as the antenna platform design. For this study, the range of 70 – 100 μm was explored. As in the second sweep of *W,* the resulting return loss curves had only minor variations from case to case which indicated a stable operational system. The return loss for this sweep is shown in Figure 4.1.4.
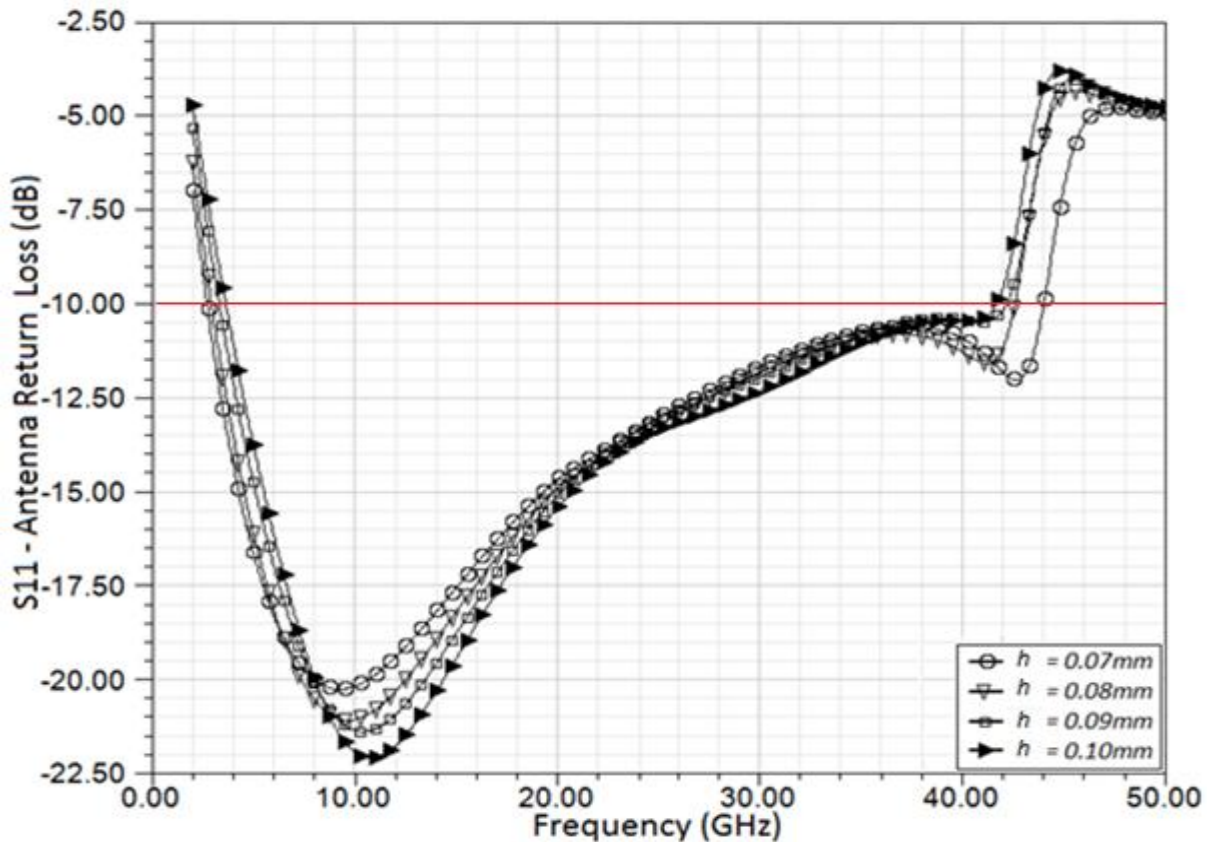
Figure 4.1.4; Return Loss of the Teardrop Planar Inverted Cone Antenna referenced to 100 Ω after a Parametric Sweep of Platform Thickness; *L = 6.2mm, W = 0.3, F = 10μm, G = 7.5 μm, S = 20 μm*

There was not much difference in the four cases in the *AWZ* sweep in the middle of the operational band, but there was a clear gain seen at the outside. The *AWZ = 100 μm* case was the same as the *W = 0.3* case in Figure 4.2.3 for reference. The *AWZ = 70 μm* case was best case observed in the final optimization sweep with a bandwidth of 16.2 ± 0.1. This bandwidth

represented a 40% gain from the previous second *W* optimization and 145% gain from the initial Td-PICA shape.

The final design was simulated at much higher levels of accuracy than the models used in the optimization to verify the validity of the results. The design parameters used in the final design are shown in Table 4.1.2. Two convergent curves for the real and imaginary impedance as well as the return loss of the Td-PICA after optimization are shown in Figure 4.1.5 and Figure 4.1.6 respectively.

Parameter	Values
L	6.2 mm
W	0.3
F	10.0 μm
G	7.5 μm
S	20.0 μm
AWZ	70.0 μm

Table 4.1.2: Optimized Teardrop Planar Inverted Cone Antenna Design Parameters
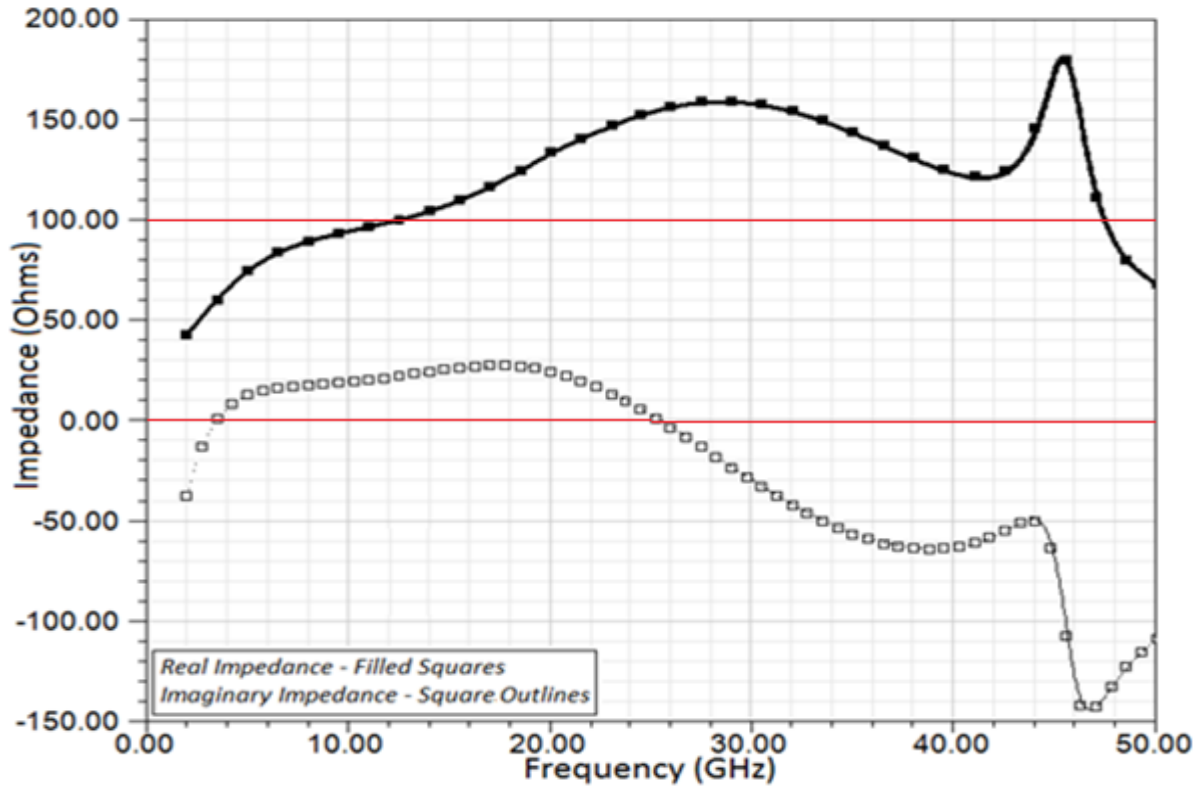
Figure 4.1.5: Real and Imaginary Impedance of the Optimized Teardrop Planar Inverted Cone Antenna
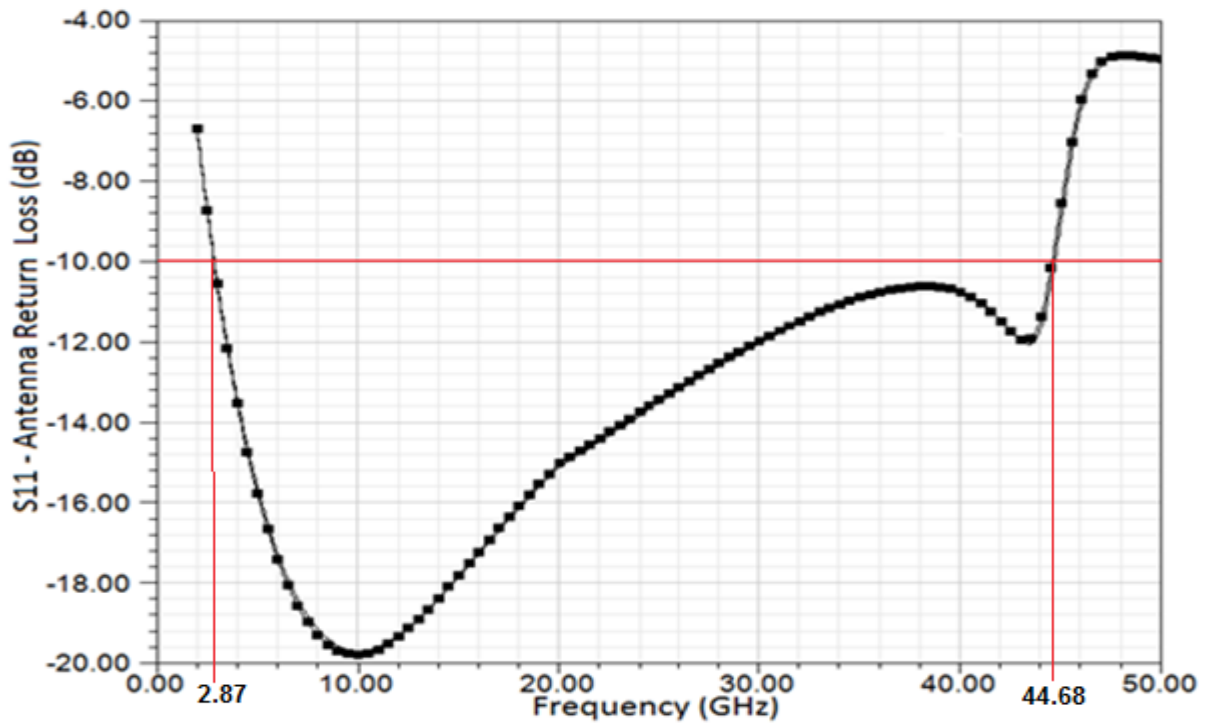
Figure 4.1.6: Return Loss of the Optimized Teardrop Planar Inverted Cone Antenna Referenced to 100 Ω

69

Not surprisingly there was a small error between the optimization results to the convergent result. Optimization results were considered to be intermediate results so they were not simulated to the highest level of accuracy. For this reason, differences were expected to appear between the convergent result and the optimization results. The final bandwidth for the optimized Td-PICA was found to be 15.6 ± 0.2. This bandwidth represented a 4% loss from the final optimization result but was still a 135% gain from the initial Td-PICA shape.

The gain patterns over the operational bandwidth were investigated to establish a range of frequencies which had useable beam shape. Gain patterns from 2 – 8 GHz are shown in Figure 4.1.7 and gain patterns from 10 – 40 GHz are show in Figure 4.1.8.
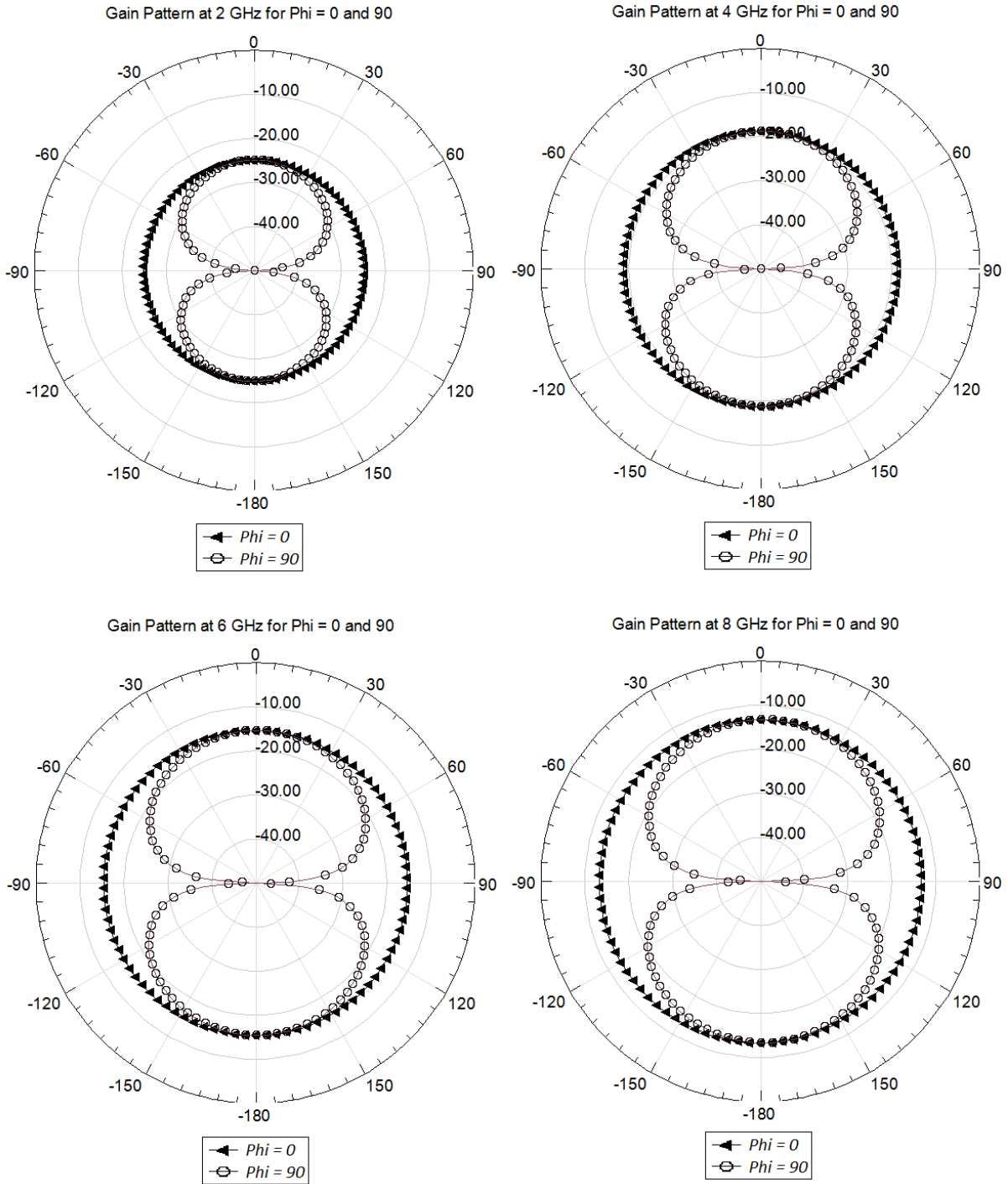
Figure 4.1.7: Gain Patterns for the Optimized Teardrop Planar Inverted Cone Antenna from 2 − 8 GHz
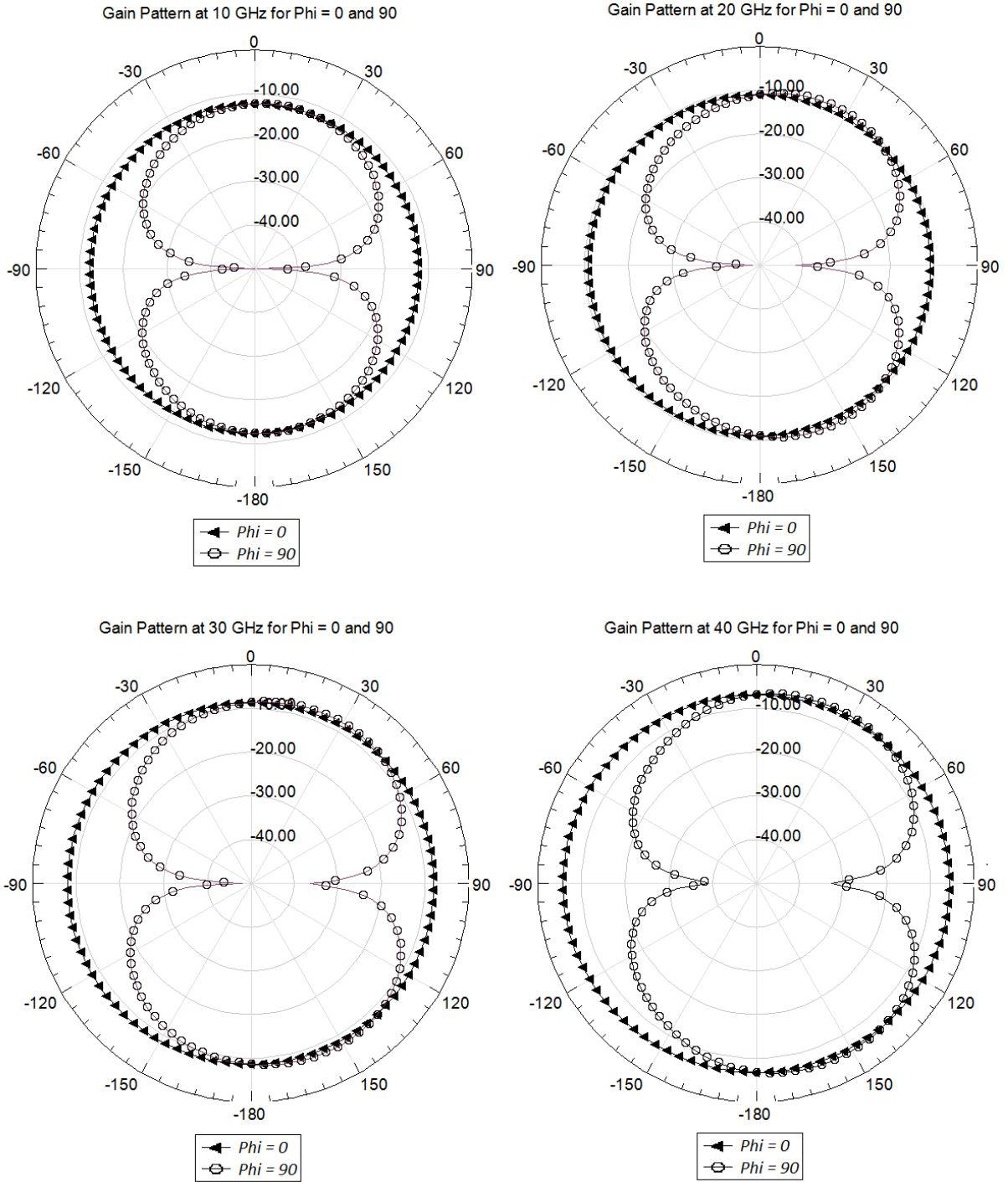
Figure 4.1.8: Gain Patterns for the Optimized Teardrop Planar Inverted Cone Antenna from $10 - 40$ GHz

The gain pattern was stable across the entire operating band of the Td-PICA and behaved like a monopole with an omnidirectional beam shape. In the simulation setups the antenna was

oriented along the Y-axis so uniform radiation was expected in the X-Z plane which was equivalent to the *Phi = 0°* plane in spherical coordinates. This was observed for all cases at all frequencies. Additionally, there should have been no gain along the Y-axis which is equivalent to *Phi = 0°* and *Theta = ± 90°* in spherical coordinates. This is observed for all cases at all frequencies.

Section 4.2 – Teardrop Planar Inverted Cone Antenna on G1 Platform

The optimized Teardrop Planar Inverted Cone Antenna was integrated with the Generation 1 (G1) antenna platform in monopole configuration and the resulting antenna simulated in HFSS. It was expected that a reduction in bandwidth would be observed when the Td-PICA was integrated but the results were more dramatic than expected. A scale rendering of the integrated antenna on the G1 platform is shown in Figure 4.2.1. The converged real and imaginary impedance are shown in Figure 4.2.2, the return loss is shown in Figure 4.2.3, and the gain patterns are shown in Figure 4.2.4. The CPW dimensions obtained in optimization were used for the entire length of the CPW in the antenna model.
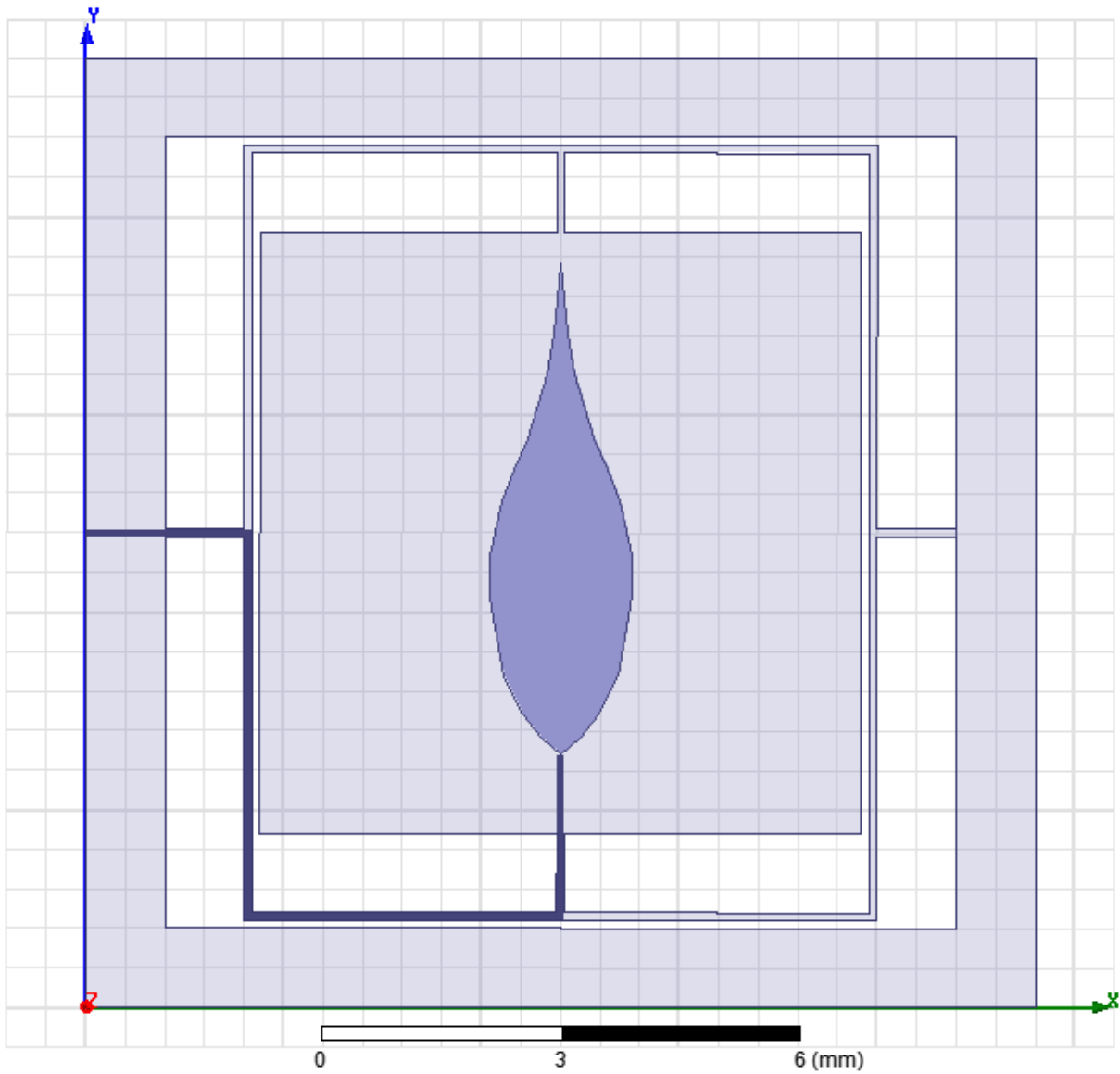
Figure 4.2.1: Rendering of the Optimized Teardrop Planar Inverted Cone Antenna on the G1
Antenna Platform

Figure 4.2.2: Real and Imaginary Impedance of the Optimized Teardrop Planar Inverted Cone Antenna on the G1 Antenna Platform in Monopole Configuration

Figure 4.2.3: Return Loss of the Optimized Teardrop Planar Inverted Cone Antenna on the G1 Antenna Platform in Monopole Configuration, Referenced to 50 Ω

Figure 4.2.4: Gain Patterns for Optimized Teardrop Planar Inverted Cone Antenna on the G1
Antenna Platform in Monopole Configuration from 4 – 32 GHz

76

After integration with the G1 platform the antenna was no longer broadband but rather a muti-notch band antenna. In this operational mode, an antenna has multiple narrow operational bands equally space by 3.2 GHz. The bandwidth of the first operational mode was 1.08 ± 0.01 or put another way, the first mode was centered at 6.6 GHz with a width of 0.48 GHz. It was unknown how high in frequency these operational modes lased but it was likely to be around the cutoff frequency of the optimized Td-PICA at 42 GHz. This could possibly be useful for multiband communications networks but was not desirable for a versatile broadband antenna. The antenna behavior was attributed to the addition of the three 90° turns the CPW has to make to cross the hinge structure suspending the G1 platform. As far as the stated goal of this thesis, this antenna had terrible bandwidth of less than 1.1 for every operational mode which was a loss in performance over prototypic antennas. This antenna however could be interesting if an application requiring a broad range of multi band operation was discovered. The radiation pattern weakly behaved like a monopole and an isotropic radiator with low gain.

Section 4.3 – Teardrop Planar Inverted Cone Antenna on G2 Platform

The antenna platform was redesigned to be more practical for antenna integration. The narrow hinges that the transmission lines had to follow introduced signal reflections and numerous unwanted resonances. The Generation 2 (G2) antenna platform had more area so that the three 90° bends in the transmission line could be replaced by six 45° bends in an effort to reduce reflections and thus return loss.

Two configurations were integrated with the G2 platform and simulated: a monopole and a dipole Td-PICA. Each configuration had a custom G2 designed to best fit the antenna while minimizing chip size. The dipole naturally had to have a longer antenna platform to realize this design. The monopole was CPW center fed as in all prior simulations but the dipole was slightly

different. One teardrop of the dipole was fed by the CPW center feed while the second teardrop was connected to one of the CPW grounds. This resulted in a folded dipole type configuration. Scale renderings of the integrated antenna on the G2 platform in dipole and monopole configuration is shown in Figure 4.3.1 and Figure 4.3.2 respectively. The converged real and imaginary impedances of both antenna configurations are shown in Figure 4.3.3, the converged return losses of both configurations are shown in Figure 4.3.4, the gain patterns of the monopole are shown in Figure 4.3.5, and the gain patterns of the dipole are shown in Figure 4.3.6
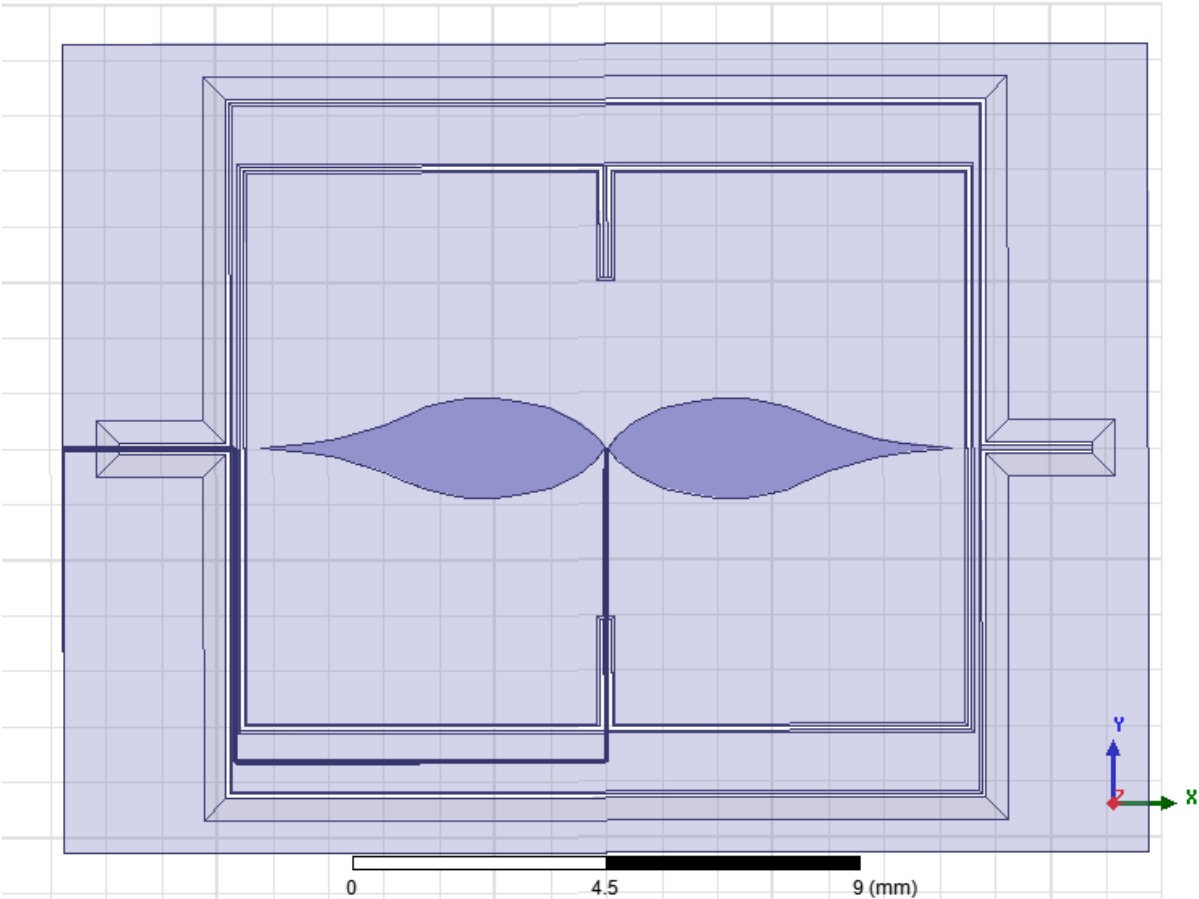
Figure 4.3.1: Rendering of the Optimized Teardrop Planar Inverted Cone Antenna on the G2 Antenna Platform in Dipole Configuration

78

Figure 4.3.2: Rendering of the Optimized Teardrop Planar Inverted Cone Antenna on the G2
Antenna Platform in Monopole Configuration
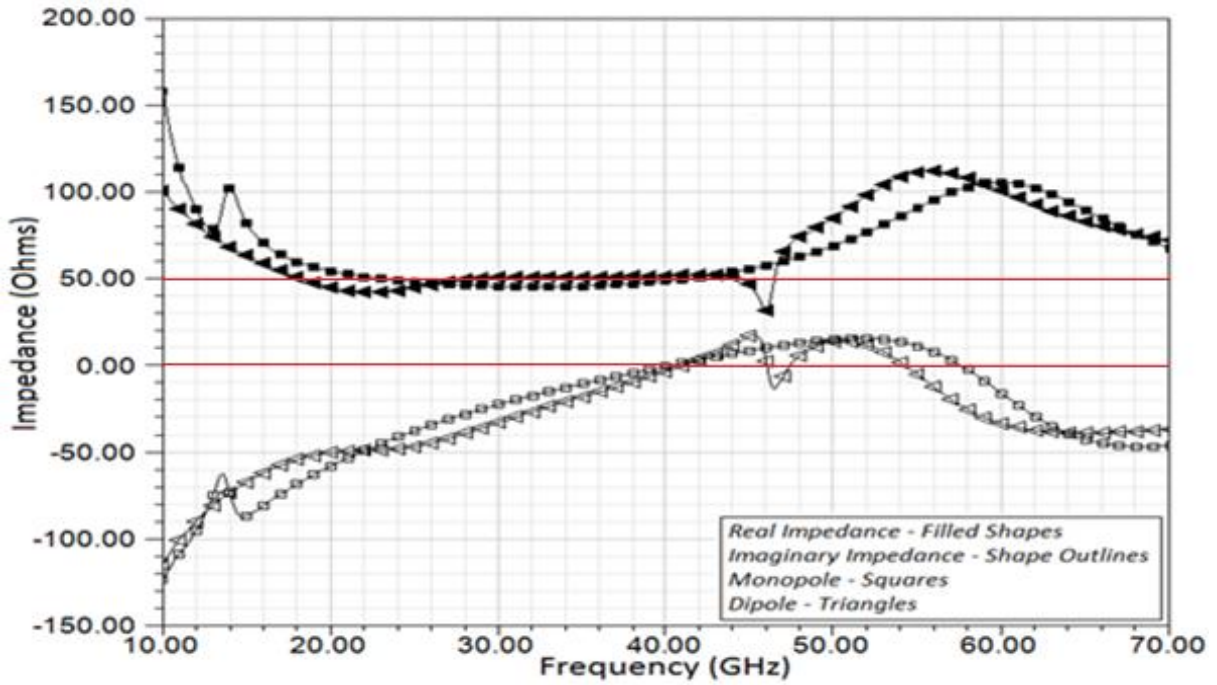
Figure 4.3.3: Real and Imaginary Impedance of the Optimized Teardrop Planar Inverted Cone Antenna on the G2 Antenna Platform in Monopole and Dipole Configurations
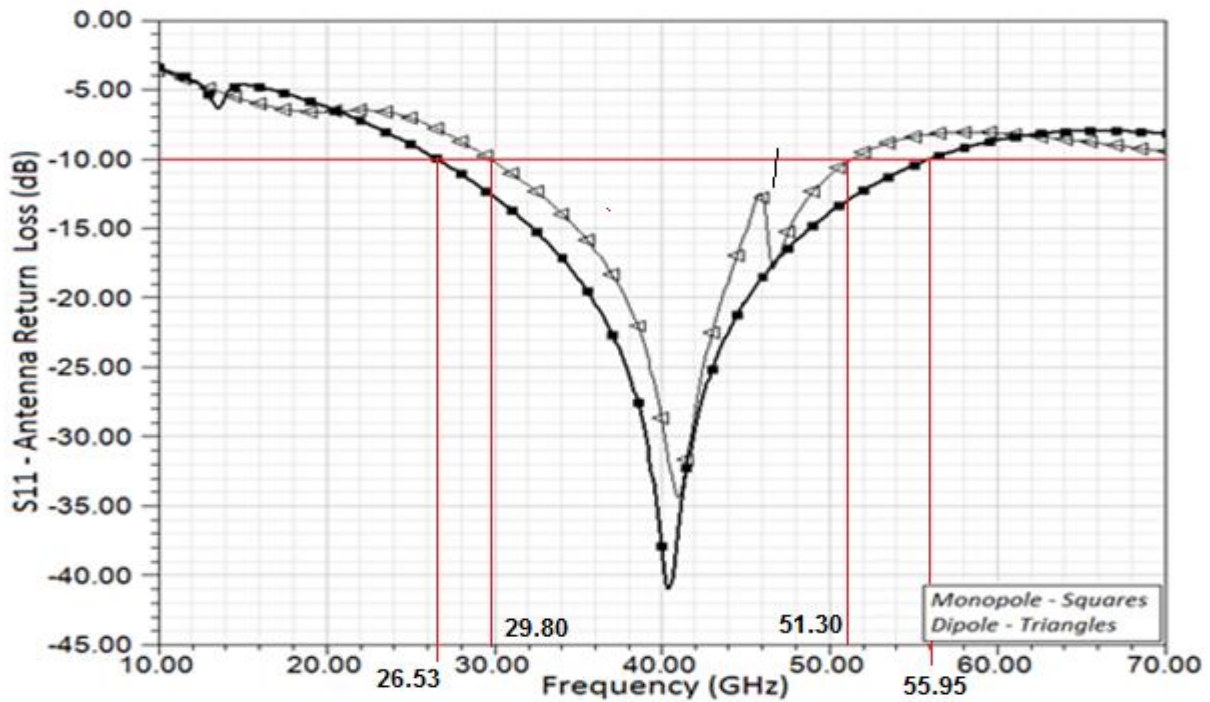
Figure 4.3.4: Return Loss of the Optimized Teardrop Planar Inverted Cone Antenna Referenced to 50 Ω on the G2 Antenna Platform in Monopole and Dipole Configurations
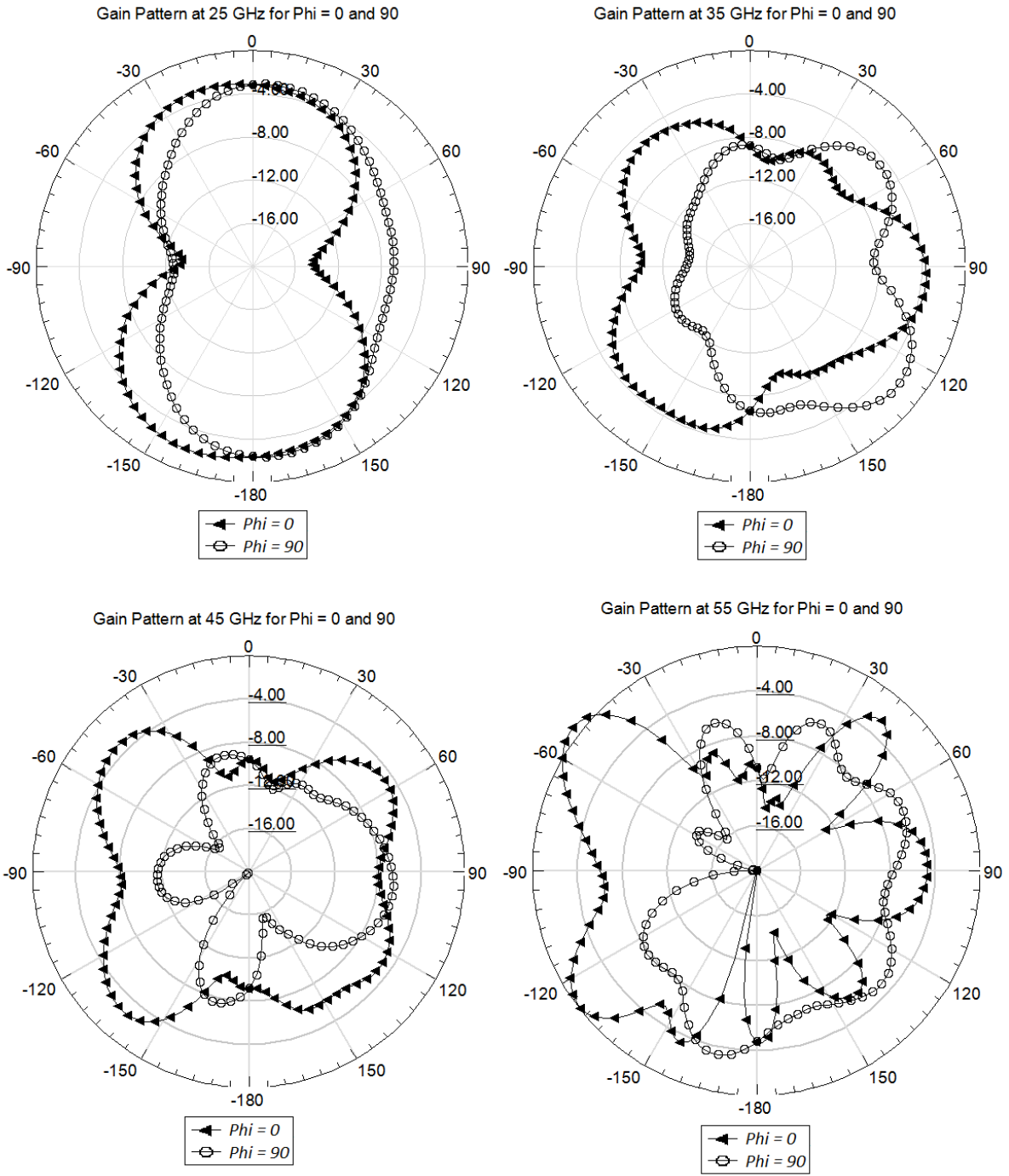
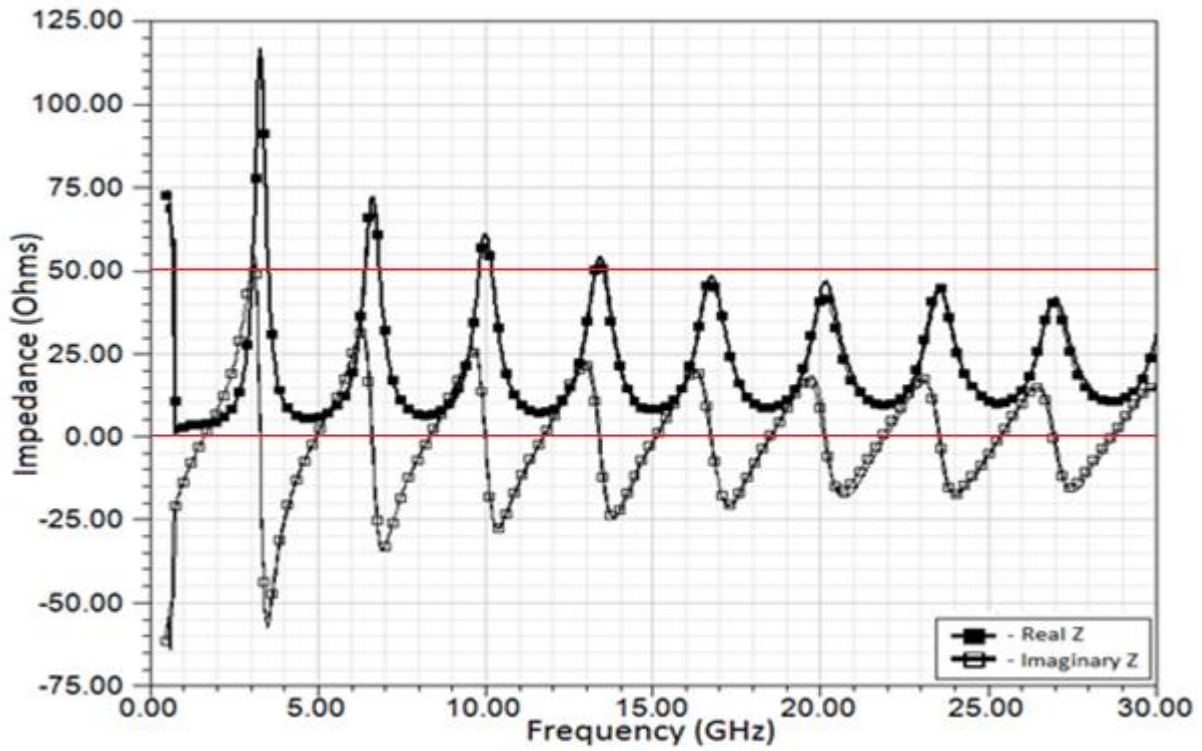Figure 4.3.5: Gain Patterns of the Optimized Teardrop Planar Inverted Cone Antenna on the G2 Antenna Platform in Monopole Configuration from 25 – 55 GHz
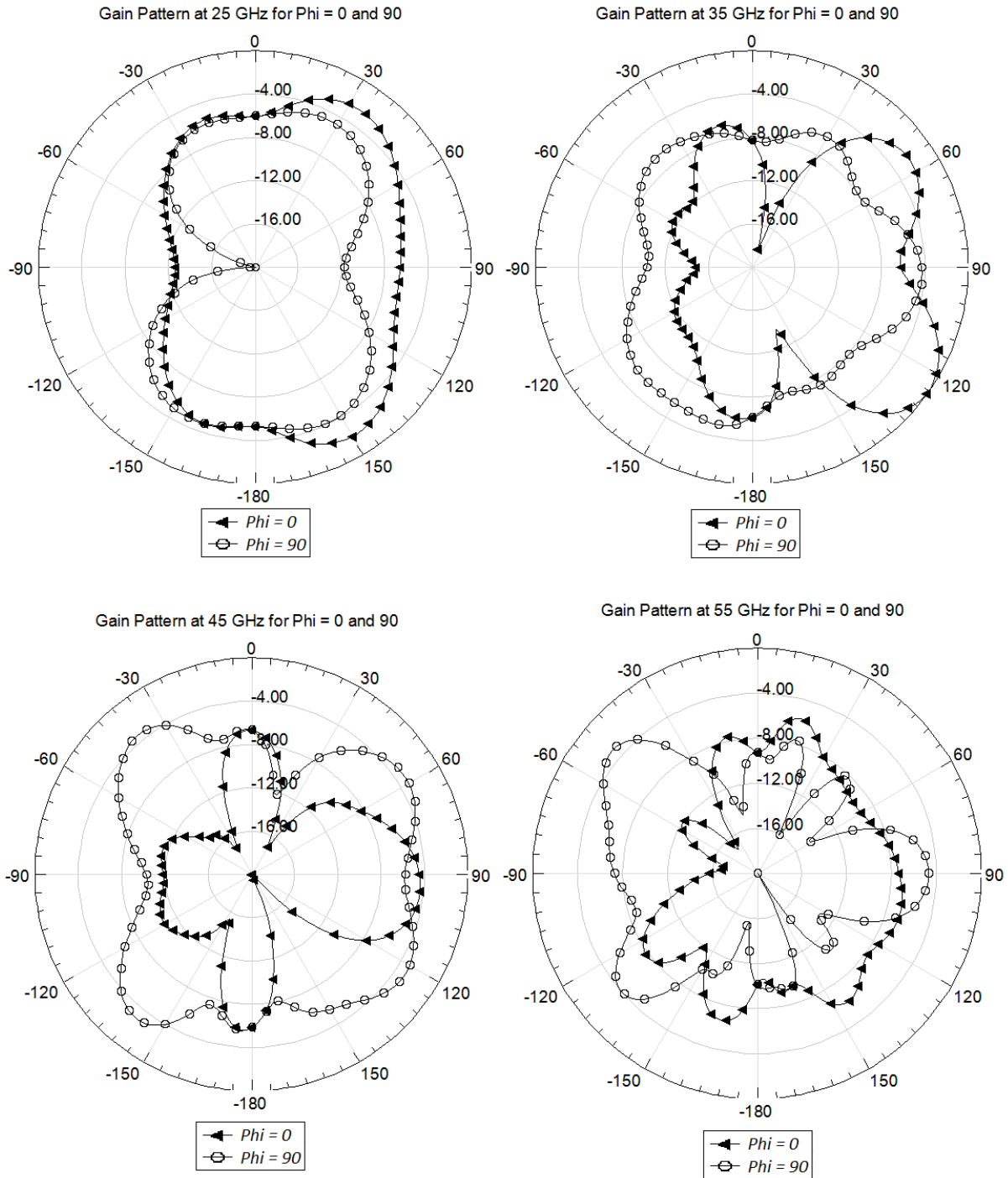
Figure 4.3.6: Gain Patterns of the Optimized Teardrop Planar Inverted Cone Antenna on the
G2 Antenna Platform in Dipole Configuration from 25 – 55 GHz

Both the monopole and dipole had much better impedance bandwidth on the G2 platform

than was observed with the G1 platform. Both antennas operated over a wide enough range of

frequencies to be considered a broadband antenna. The bandwidth of the monopole and dipole were $2.11 \pm .01$ and $1.72 \pm .01$ respectively, which represented a 36% increase and an 11% increase over [1]. Alternately, the monopole's bandwidth was centered at 40.6 GHz with a width of 29.4 GHz and the dipole's bandwidth was centered at 41.2 GHz with a width of 21.5 GHz. Omnidirectional beam shape was only seen at the lowest frequencies simulated for both antenna configurations. At higher frequencies, the beam shape had numerous side lobes. This effect was due to the feedline structure radiating and thus changing the over radiation pattern.

Section 4.4 – Teardrop Planar Inverted Cone Antenna on G3 Platform

The G3 antenna platform was developed to completely eliminate bends in the CPW transmission line because it was believed that the turns were leading to losses in bandwidth. The G3 platform achieved the goal of improving bandwidth and having satisfactory gain and beam patterns but sacrificed one degree of freedom for rotation of the steerable antenna platform. Only a single monopole configuration was studied on the G3 platform. A scale rendering of the integrated antenna on the G3 platform is shown in Figure 4.4.1. The converged real and imaginary impedances are shown in Figure 4.4.2, the return loss is shown in Figure 4.4.3, and the gain patterns are shown in Figure 4.4.4.
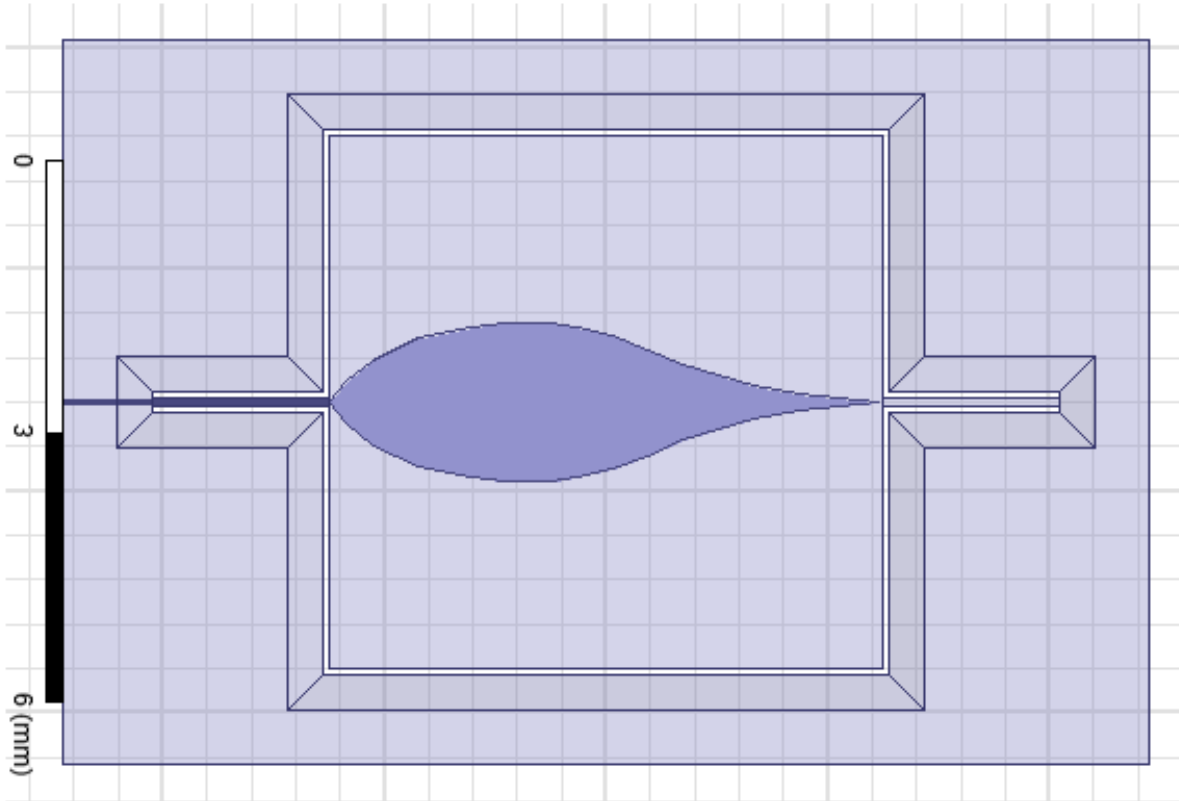
Figure 4.4.1: Rendering of the Optimized Teardrop Planar Inverted Cone Antenna on the G3 Antenna Platform
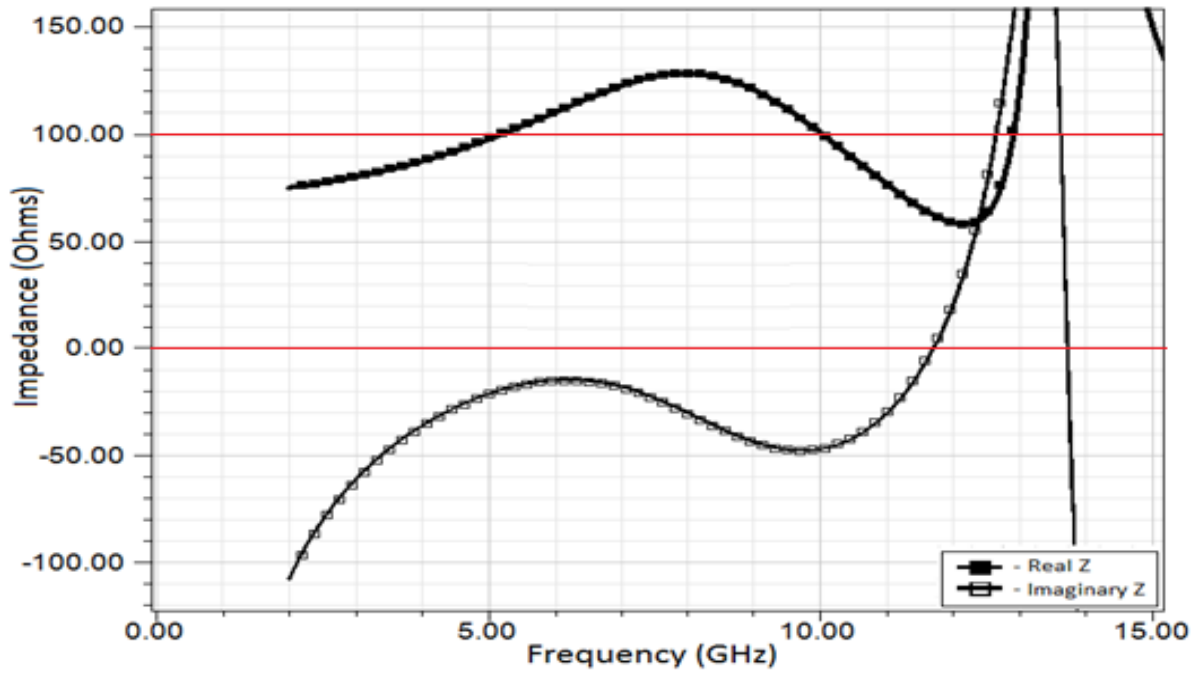
Figure 4.4.2: Real and Imaginary Impedance of the Optimized Teardrop Planar Inverted Cone Antenna on the G3 Antenna Platform in Monopole Configuration
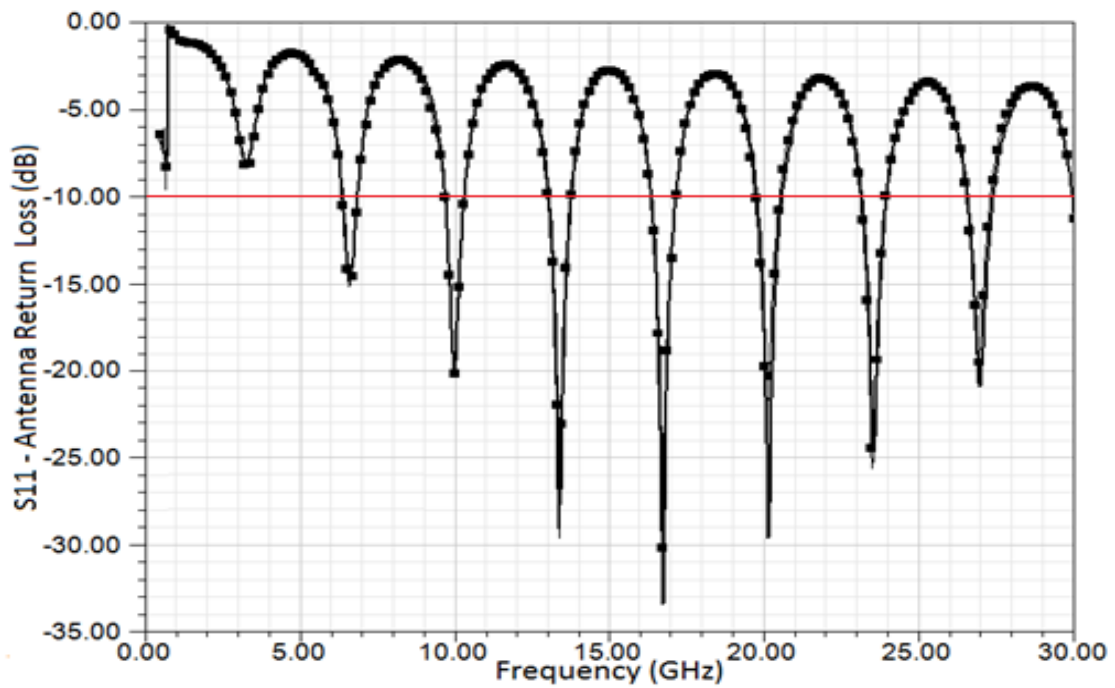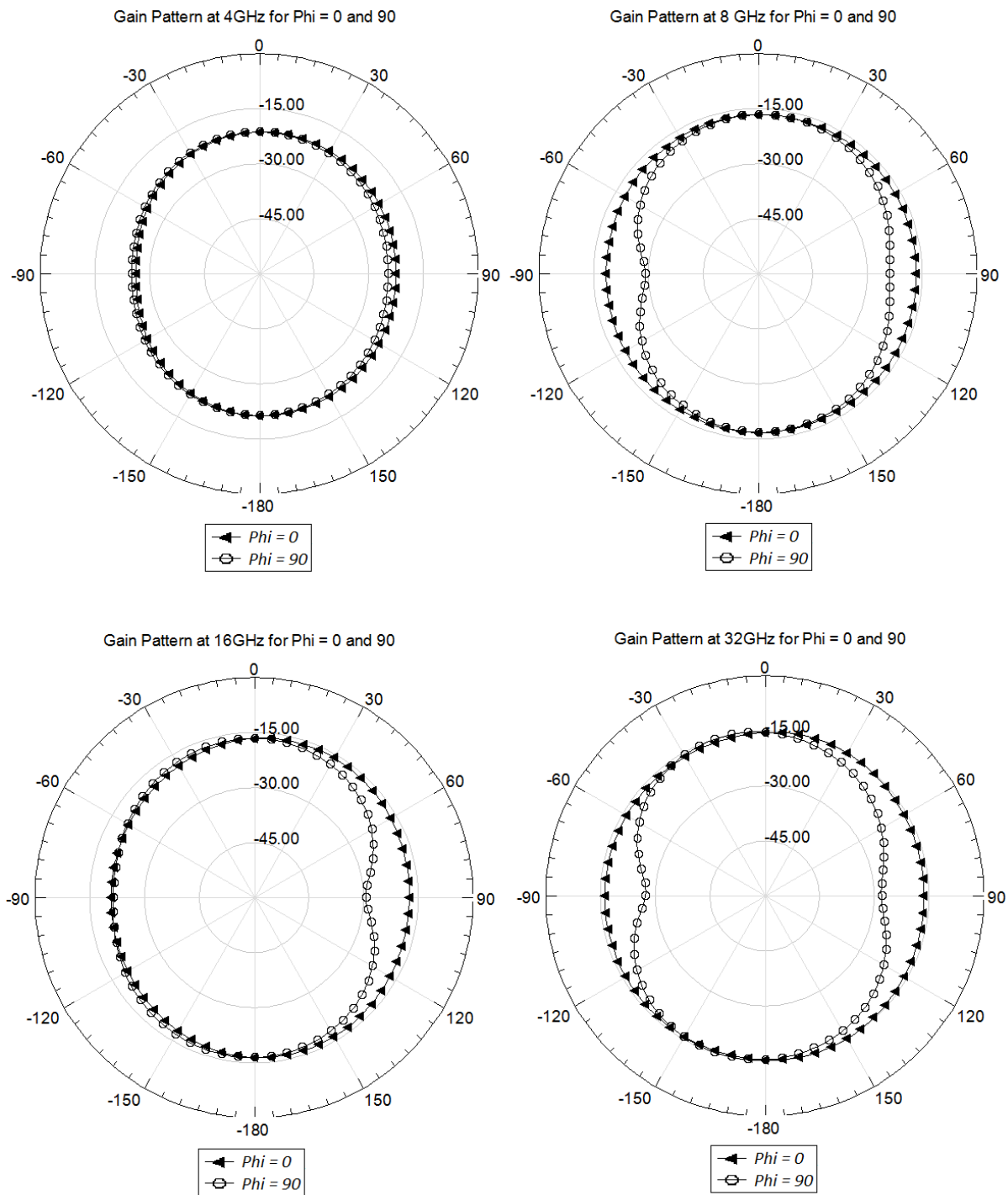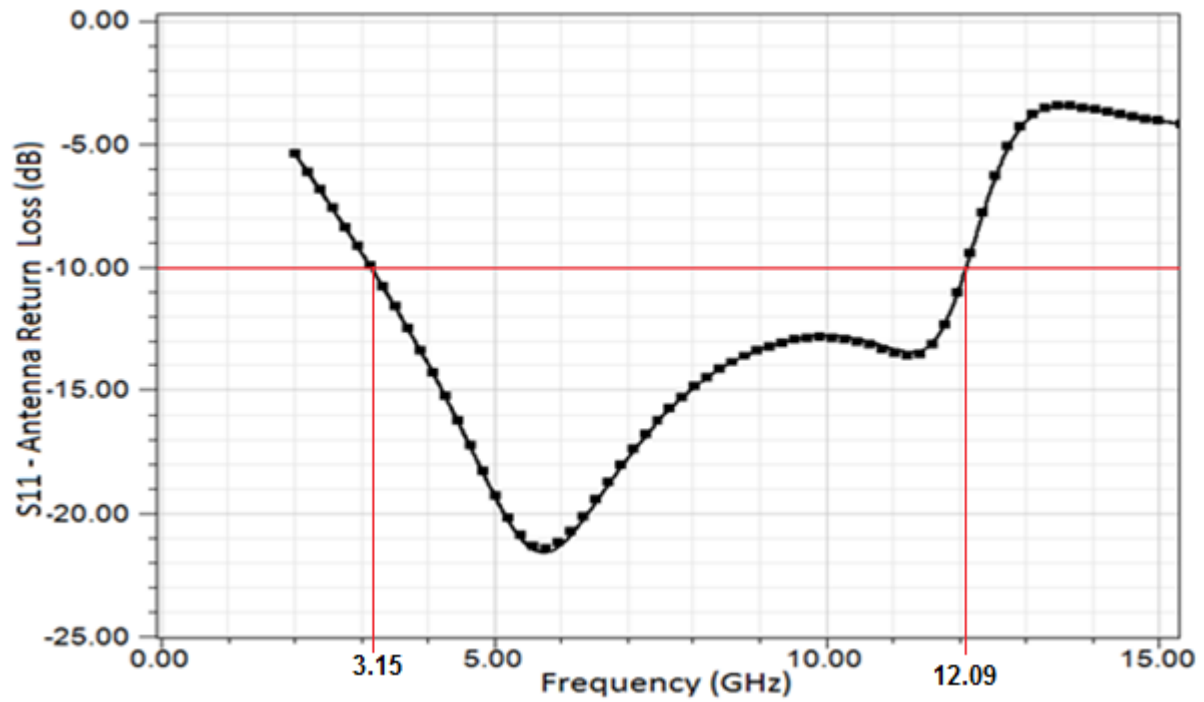

Figure 4.4.3: Return Loss of the Optimized Teardrop Planar Inverted Cone Antenna Referenced to 100 Ω on the G3 Antenna Platform in Monopole Configuration

85

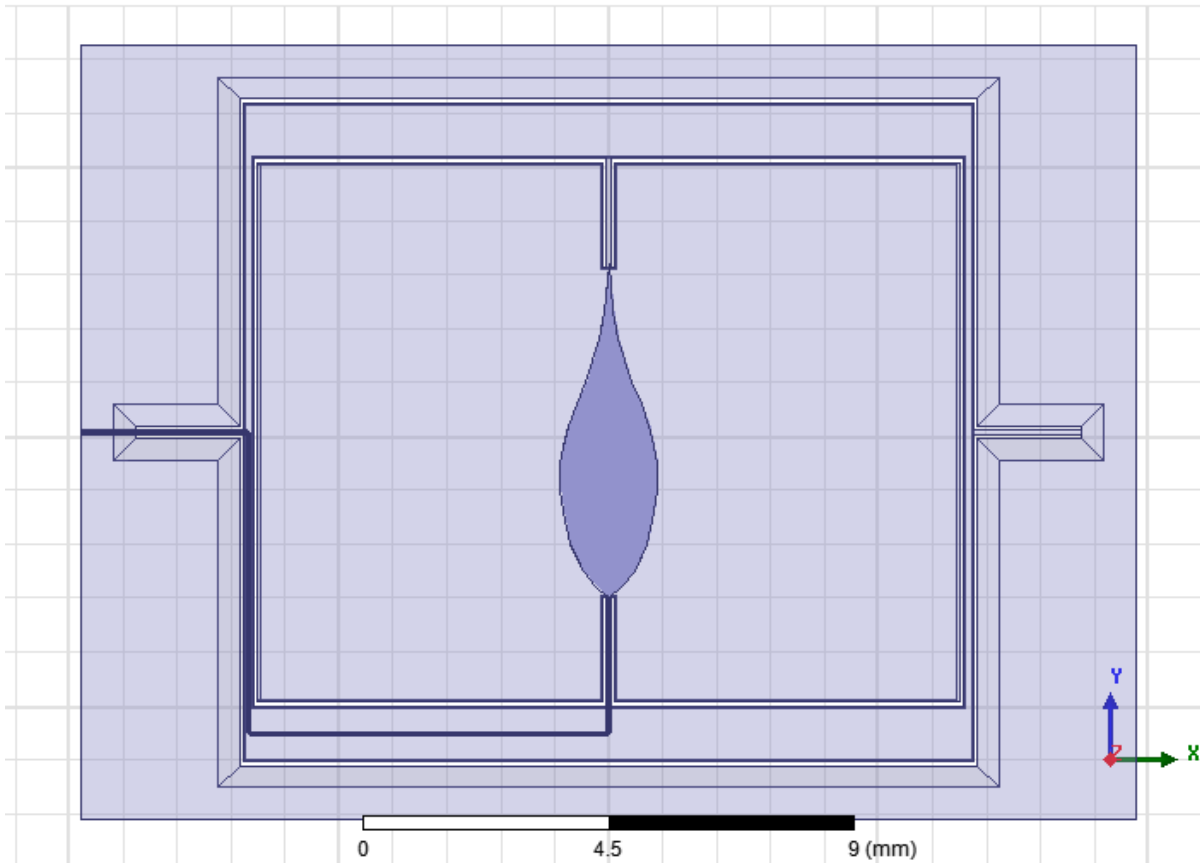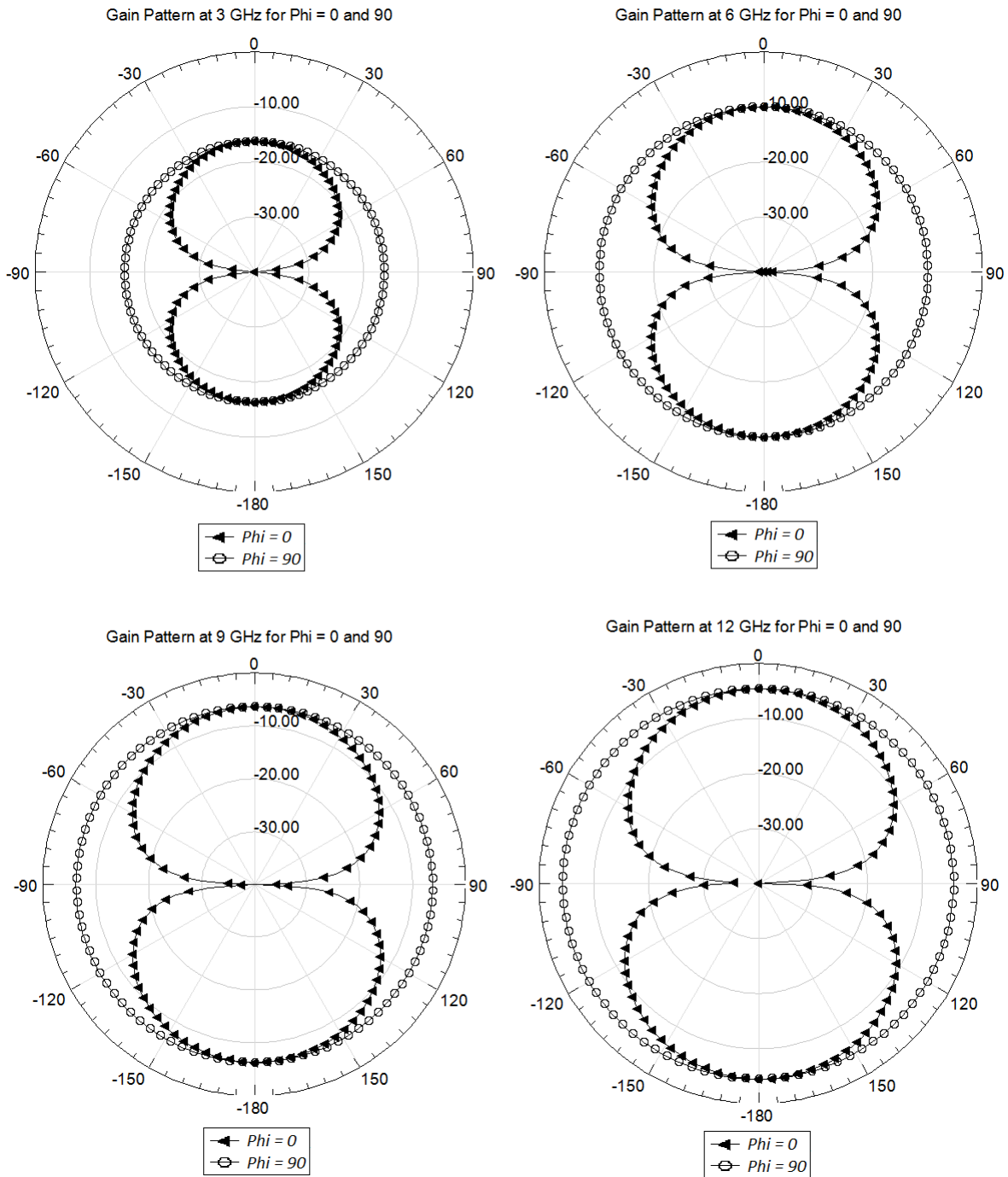Figure 4.4.4: Gain Patterns of the Optimized Teardrop Planar Inverted Cone Antenna on the G3 Antenna Platform in Monopole Configuration from 3 − 12 GHz

The Td-PICA on G3 antenna platform proved to work well. The theory that eliminating CPW bends should increase bandwidth was confirmed. The impedance bandwidth was found to be 3.84 ± .03, which represented a 148% increase over [1]. Alternately, the bandwidth was

centered at 7.6 GHz with a width of 8.2 GHz. The beam shape was a very stable monopole type omnidirectional pattern over the entire range of frequencies simulated.

Section 4.5 – Cylindrical Dielectric Resonator Antenna on G3 Platform

The usefulness of the G3 antenna platform was exploited by simulating and optimizing two more antenna designs. The new designs were both Dielectric Resonator Antennas (DRA) which were described in Section 2.2. Section 4.5 presents a typical planar cylindrical DRA (C-DRA) while Section 4.6 presents a novel teardrop shaped DRA (Td-DRA).

A limited optimization of the C-DRA was undertaken. The antenna was stub fed from a CPW that terminated under the dielectric. The diameter of the C-DRA was fixed at 4.0 mm. The two design variables that were optimized were the feeding stub length and the dielectric thickness. The stub length was swept from 100 – 900 μm with a 400 μm step size. The DRA thickness was swept from 100 – 300 μm with a 100 μm step size. A full factorial DOE was undertaken to see the effect of the two optimization variables. A scale rendering of the C- DRA on the G3 platform is shown in Figure 4.5.1. The return loss of the resulting antenna variations are shown in Figure 4.5.2. The DOE and the resulting bandwidths are shown in Table 4.5.1.
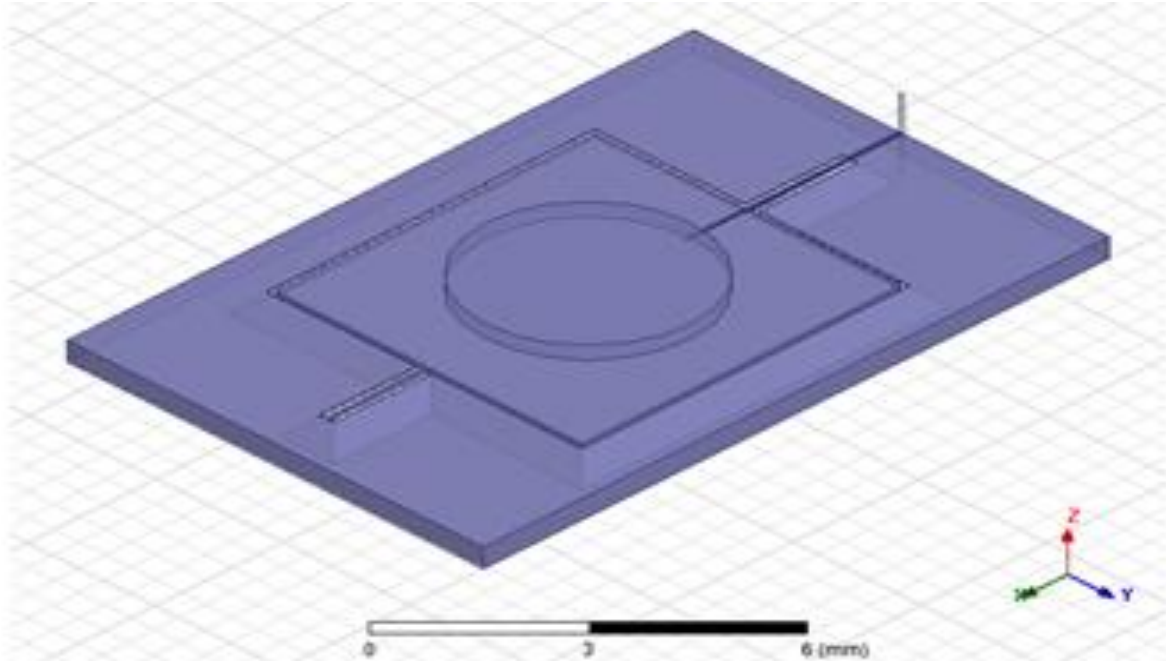
Figure 4.5.1: Rendering of the Optimized Cylindrical Dielectric Resonator Antenna on the G3 Antenna Platform
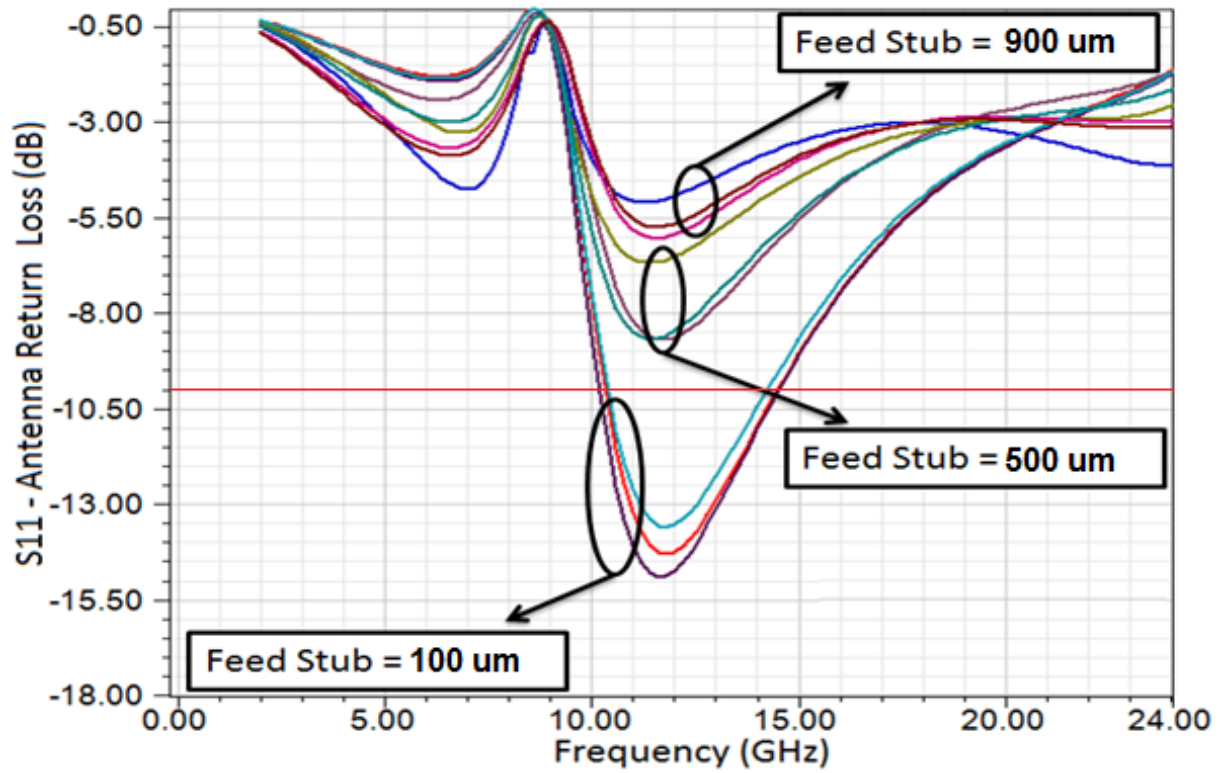
Figure 4.5.2: Return Loss of Cylindrical Dielectric Resonator Antennas on the G3 Platform for Full Factorial Design of Experiments

Expt.	Dielectric Thickness (µm)	Feed Stub (µm)	Bandwidth
1	100	100	1.40
2	200	100	1.43
3	300	100	1.37
4	100	500	N/A
5	200	500	N/A
6	300	500	N/A
7	100	900	N/A
8	200	900	N/A
9	300	900	N/A

Table 4.5.1: Design of Experiments for the Cylindrical DRA
on G3 Platform with Resulting Bandwidths

From the optimization it was clear that a short feeding stub should be used. The dielectric thickness did not show a strong effect on bandwidth. The thickest cases seemed to work slightly better than the thinner iterations. The best case simulated was the case when the dielectric thickness was 200 µm and the feeding stub length was 100 µm. A convergent model was run to determine the behavior of the best case cylindrical DRA. The converged real and imaginary impedances of the cylindrical DRA are shown in Figure 4.5.3, the converged return loss is shown in Figure 4.5.4, and the gain patterns are shown in Figure 4.5.5.
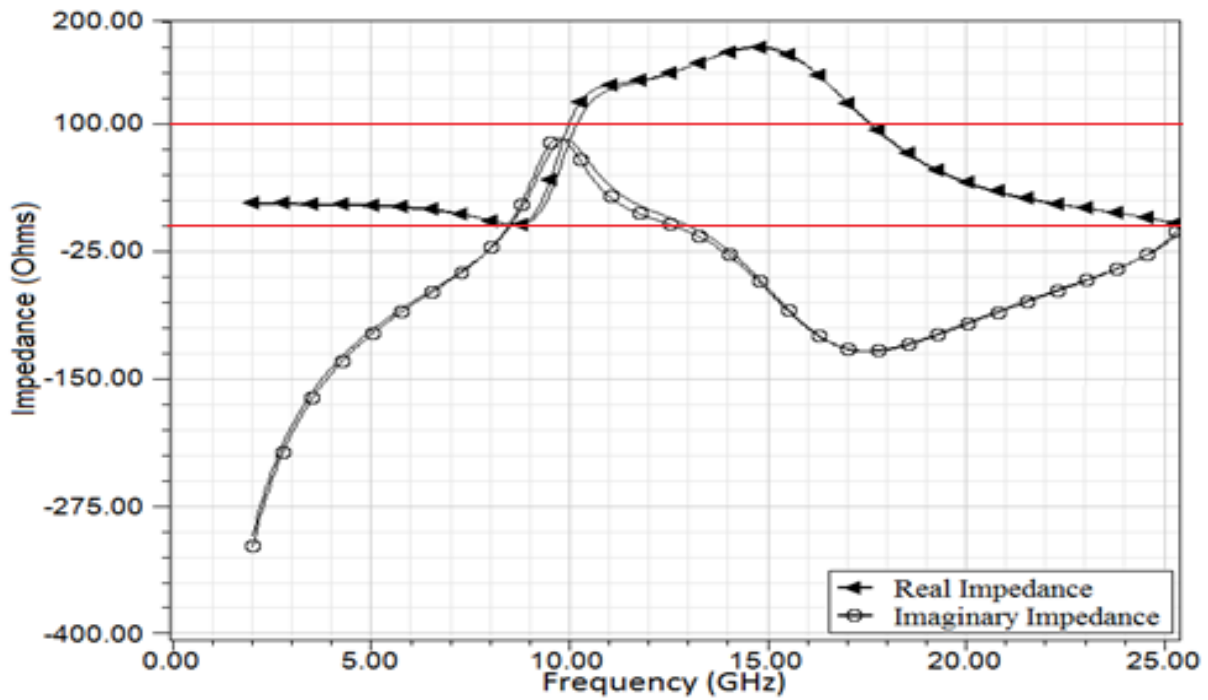
Figure 4.5.3: Real and Imaginary Impedance of the Optimized Cylindrical Dielectric Resonator Antenna on the G3 Antenna Platform
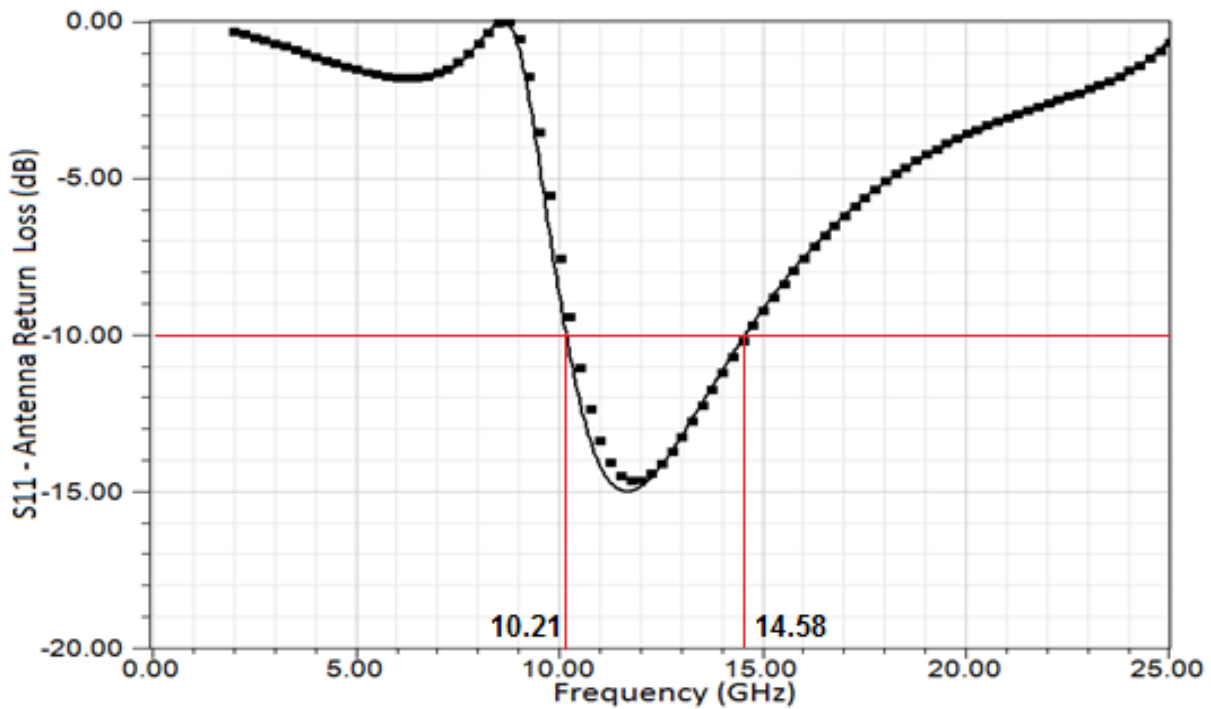
Figure 4.5.4: Return Loss of the Optimized Cylindrical Dielectric Resonator Antenna Referenced to 100 Ω on the G3 Antenna Platform

90
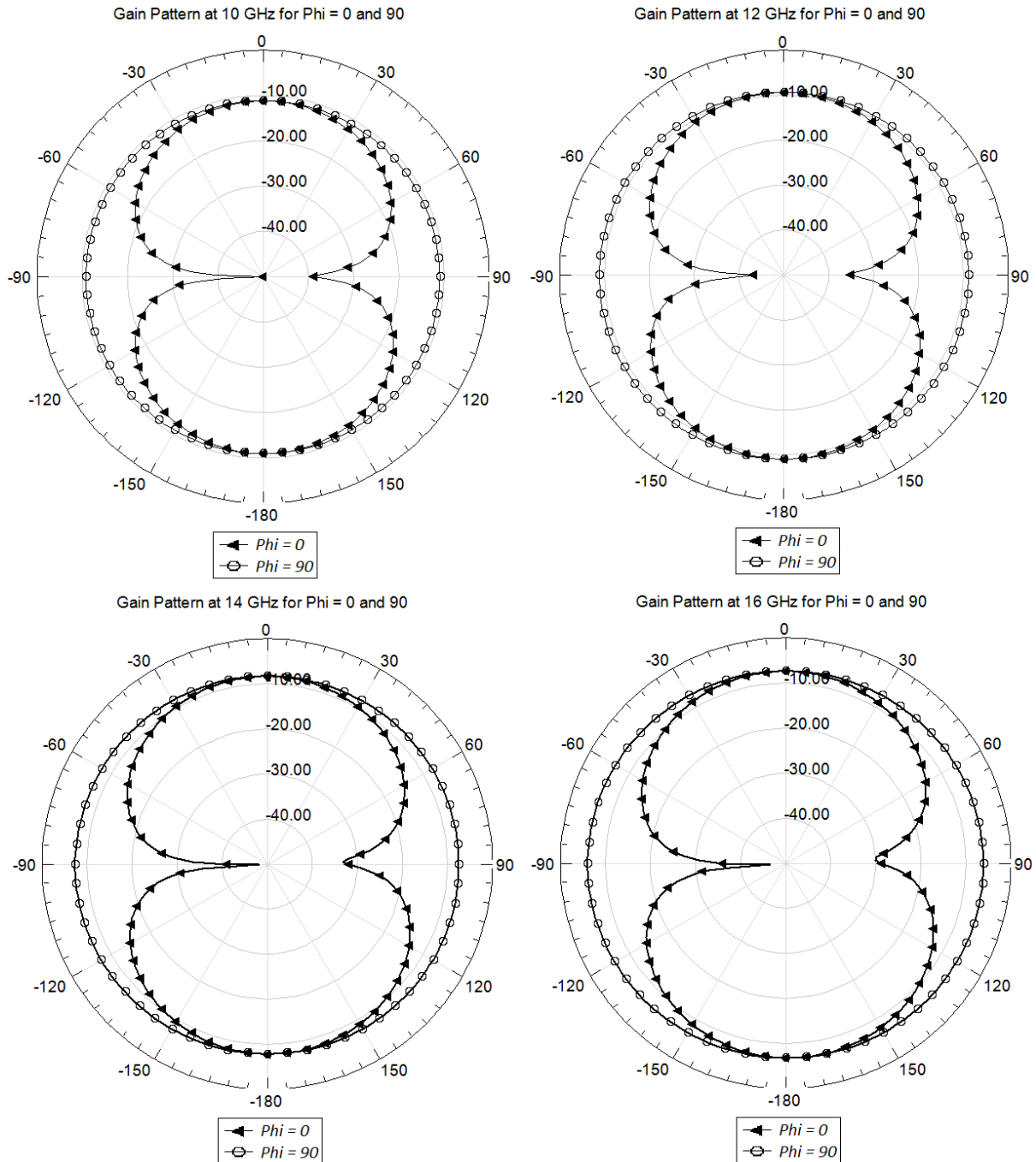
Figure 4.5.5: Gain Patterns of the Optimized Cylindrical Dielectric Resonator Antenna on the G3 Antenna Platform from 10 − 16 GHz

The impedance bandwidth cylindrical DRA was 1.43 ± 0.02 which represented a 8% loss

over [1]. Alternately, the bandwidth was centered at 12.4 GHz with a width of 4.4 GHz. The

beam shape was a very stable monopole type omnidirectional pattern over the entire range of frequencies simulated.

Section 4.6 – Teardrop Dielectric Resonator Antenna on G3 Platform

The final antenna presented in this thesis is a novel DRA shape on the G3 platform, the Teardrop DRA (Td-DRA). The shape used was the same as the optimized Td-PICA. The Td-DRA was fed in the same way as the cylindrical DRA with a similar dielectric thickness. An optimization of the teardrop shape was undertaken but simply confirmed that the shape used was already optimized.

A limited optimization of the Td-DRA was undertaken. The two design variables that were optimized were the feeding stub length and the DRA thickness. The stub length was swept from 100 – 900 µm with a 400 µm step size. The DRA thickness was swept from 100 – 300 µm with a 100 µm step size. A full factorial DOE was undertaken to see the effect of the two optimization variables. A scale rendering of cylindrical DRA on the G3 platform is shown in Figure 4.6.1. The return loss of the resulting antenna variations are shown in Figure 4.6.2. The DOE and the resulting bandwidths are shown in Table 4.6.1.
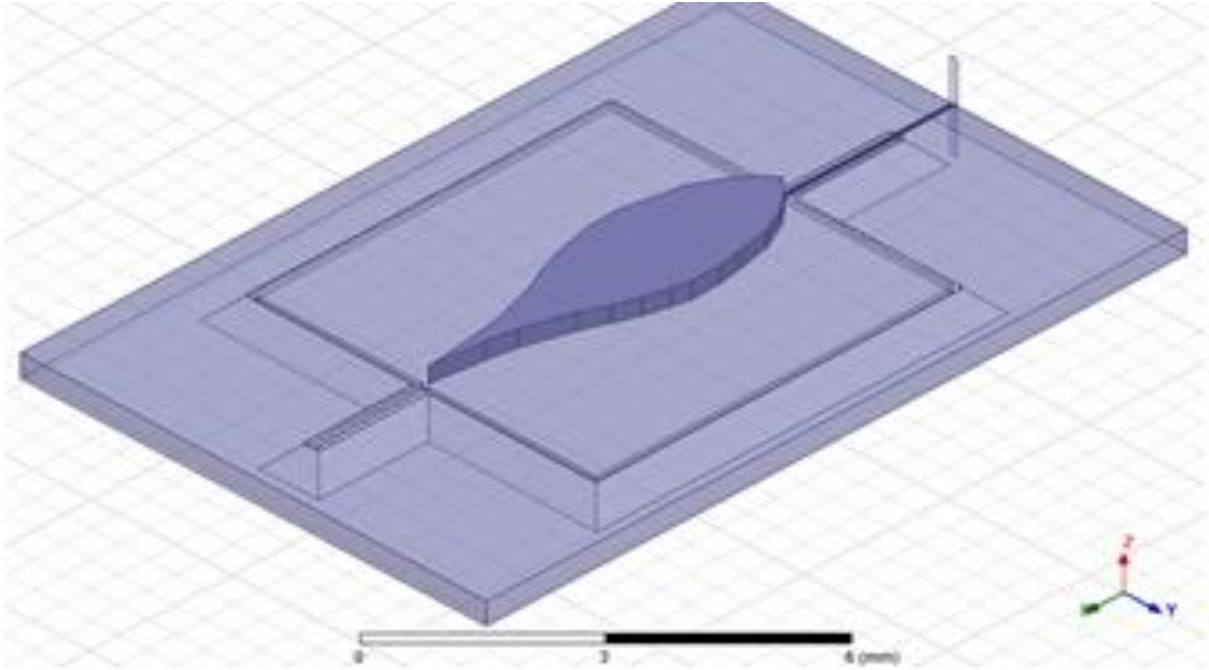
Figure 4.6.1: Rendering of the Teardrop Dielectric Resonator Antenna on the G3 Antenna Platform
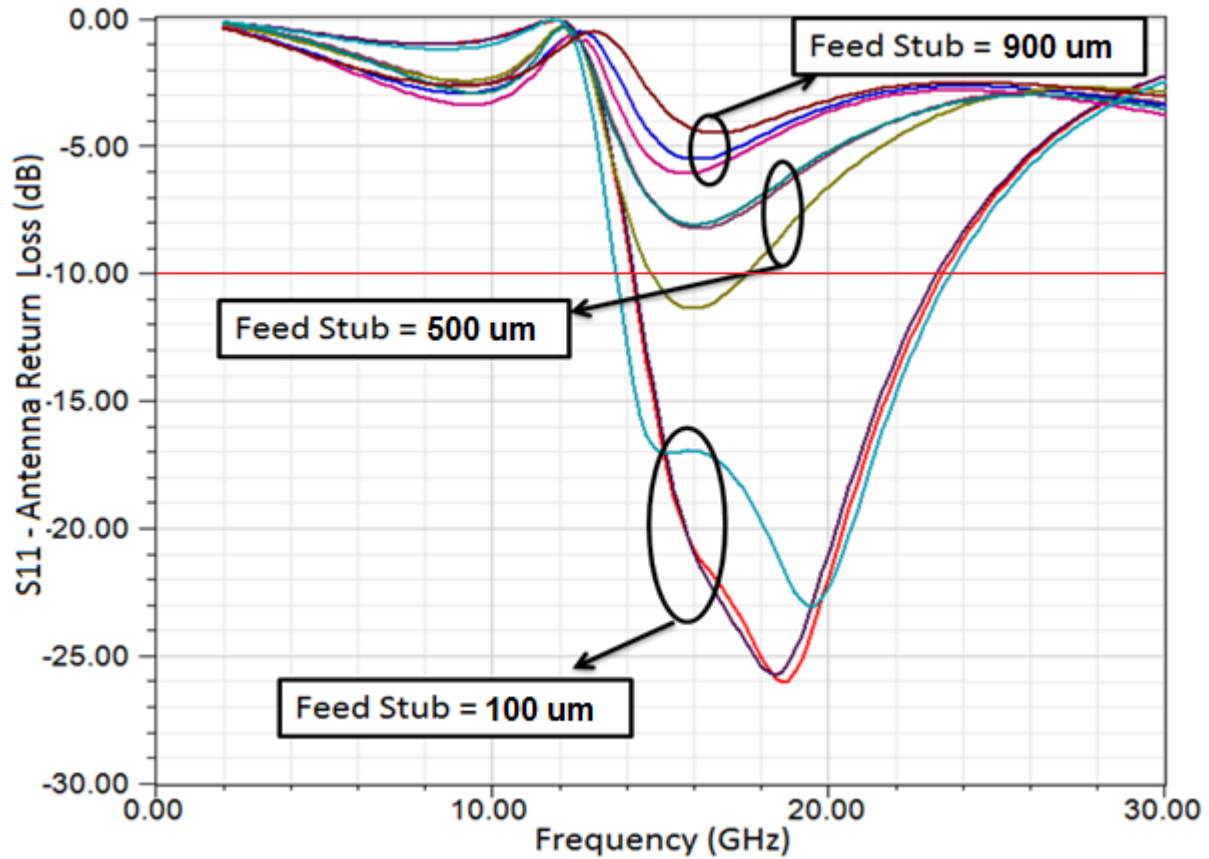
Figure 4.6.2: Return Loss of Teardrop Dielectric Resonator Antennas on the G3 Platform for Full Factorial Design of Experiments

Expt.	Dielectric Thickness (μm)	Feed Stub (μm)	Bandwidth
1	100	100	1.65
2	200	100	1.63
3	300	100	1.73
4	100	500	N/A
5	200	500	1.19
6	300	500	N/A
7	100	900	N/A
8	200	900	N/A
9	300	900	N/A

Table 4.6.1: Design of Experiments for the Teardrop Dielectric Resonator Antenna on G3 Platform with Resulting Bandwidths

From the optimization it was again clear that a short feeding stub should be used. This was the same conclusion found in Section 4.6. The dielectric thickness again did not show a strong effect on bandwidth. The thickest case seemed to work slightly better than the thinner iterations. The best case simulated was the case when the dielectric thickness was 300 μm and the feeding stub length was 100 μm. A convergent model was run to determine the behavior of the best case cylindrical DRA. The converged real and imaginary impedance of the cylindrical DRA is shown in Figure 4.6.3, the converged return loss is shown in Figure 4.6.4, and the gain patterns are shown in Figure 4.6.5
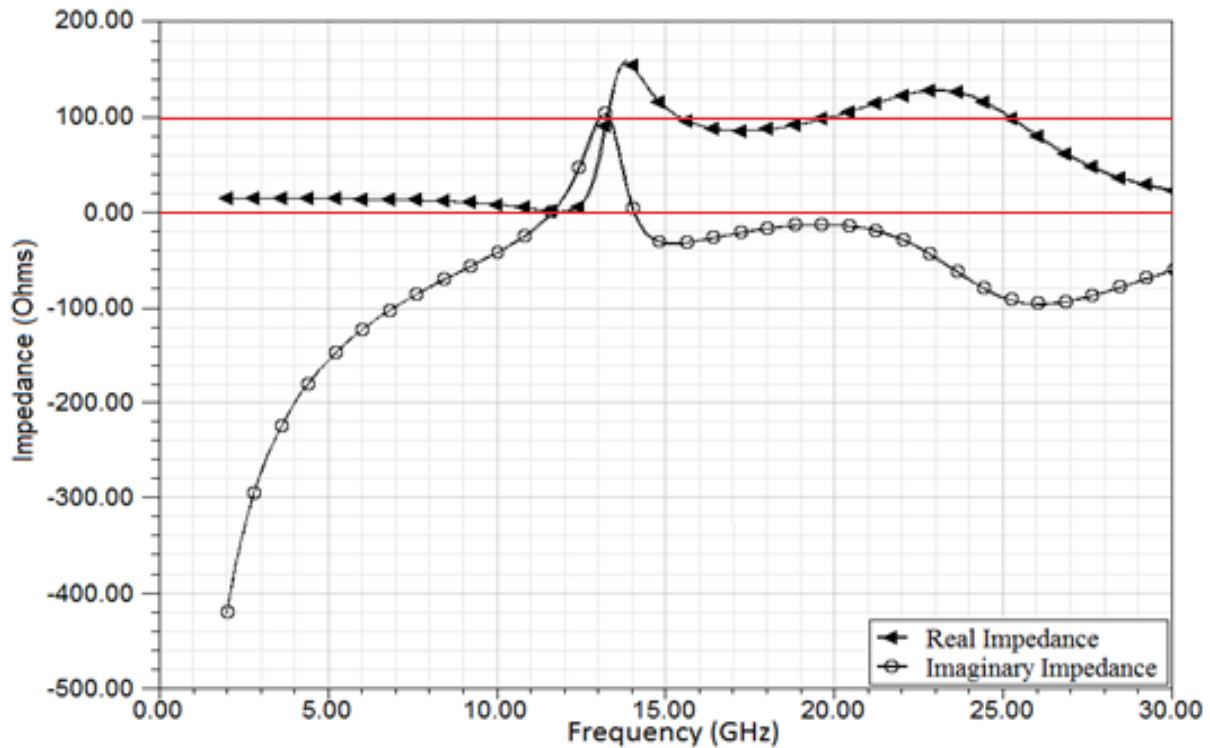
Figure 4.6.3: Real and Imaginary Impedance of the Teardrop Dielectric Resonator Antenna on the G3 Antenna Platform
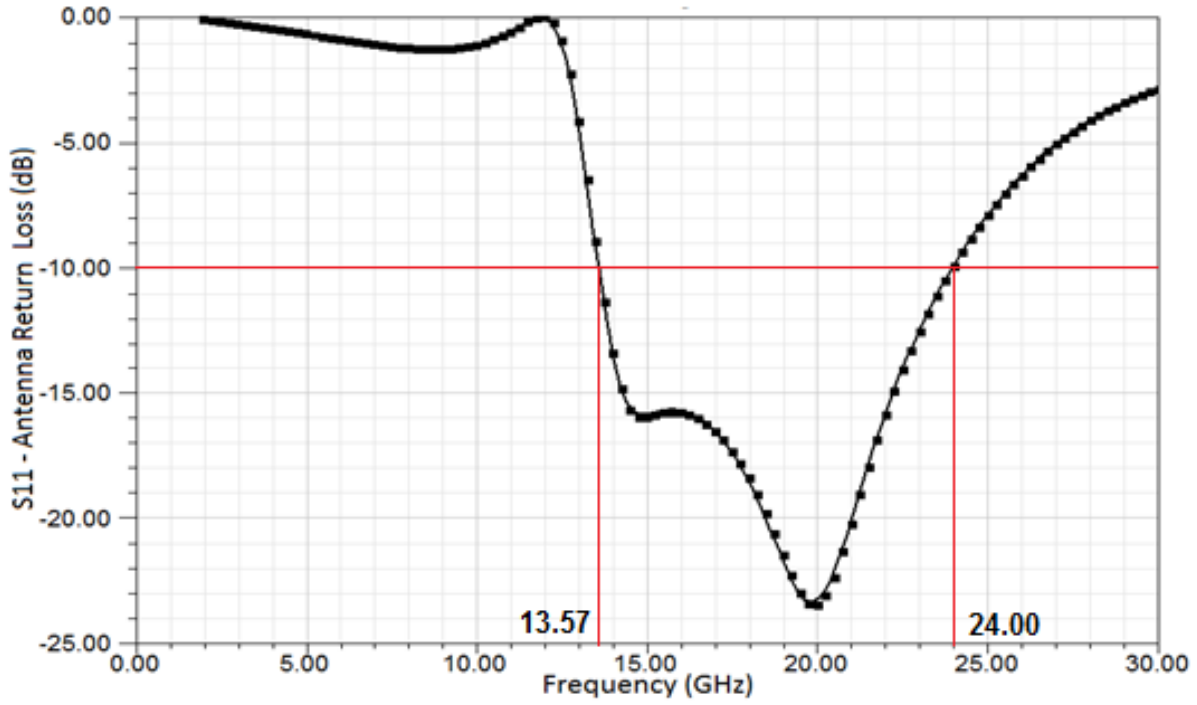
Figure 4.6.4: Return Loss of the Teardrop Dielectric Resonator Antenna Referenced to 100 Ω on the G3 Antenna Platform
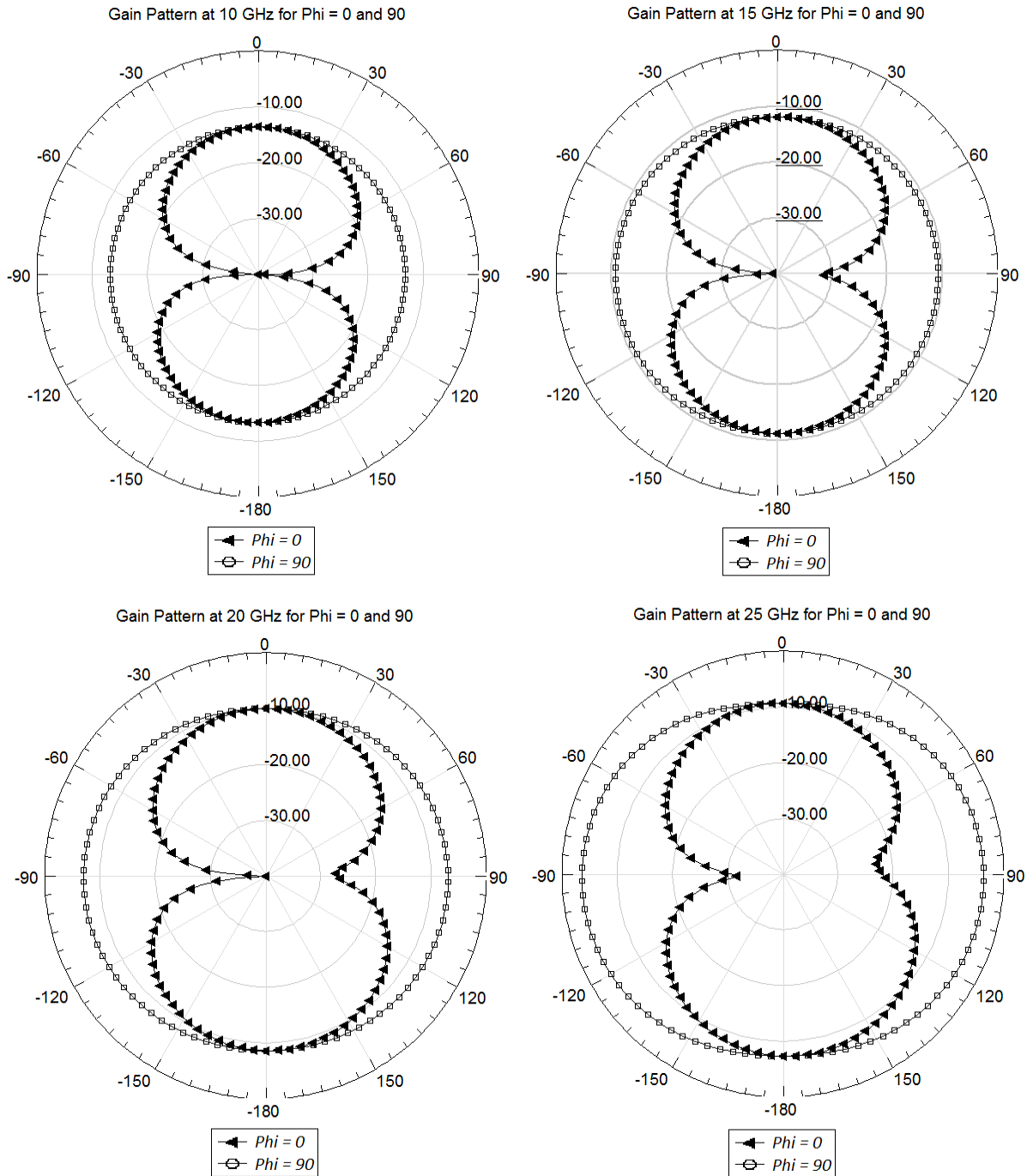
Figure 4.6.5: Gain Patterns of the Optimized Td-DRA on the G3 Antenna Platform from 10 – 25 GHz

The bandwidth was found to be $1.77 \pm .01$, which represented a 14% increase over [1]. Alternately, the bandwidth was centered at 18.8 GHz with a width of 10.4 GHz. The beam shape was a very stable monopole type omnidirectional pattern over the entire bandwidth.

Chapter 5: Results and Discussion

The prototype steerable MEMS antenna was analyzed and optimized. The original design was updated numerous times and simulated. The mechanical structure and electrical operation were studied concurrently. The G3 platform proved to have the best performance. Three different antennas were studied on the G3 platform. An integrated model of each antenna was studied on all 16 variations of the G3 platform and the results of the 48 variations were analyzed. In the end, a best case platform was selected for each antenna. The mechanical performance of each platform, the electrical performance of each antenna/platform combination, and the best results are presented in this chapter.

Section 5.1 – Mechanical Performance Summary

The steerable MEMS antenna platform was studied and optimized to reduce actuation voltage and increase the maximum angle of rotation. The prototype devices could achieve rotation in two dimensions but had low actuation angles and high actuation voltages. These were the two problems addressed in the mechanical optimization. Three variations of the platform were studied and denoted as Generations 1 − 3. Based on literature and reverse engineering of prototype devices, the maximum allowable stress in the design was determined 1.0 GPa. The Generation 3 platform proved to have the best overall combination of mechanical and electrical performance.

The Generation 1 antenna platform was the same design as presented by Dr. Hutchings in his dissertation. The approach taken to analyze the G1 platform consisted of changing dimensions of elements of the design but not changing the layout. The effect of lengthening the hinge length had the most significant effect to increase maximum platform rotation. This device proved to be unsuitable for integration with antenna designs for realizing the goal of a versatile

broadband antenna for imaging. For this reason, the full analysis of the G1 platform with an actuation model was not developed.

The Generation 2 antenna platform was based on the G1 design with several changes to improve mechanical and electrical performance. The most significant change was the thinning of the hinges with respect to the antenna platform. Studies showed that reducing hinge thickness had a significant effect to reduce critical voltage. The effect of increased maximum rotation for longer hinges was strongly observed in the G2 devices as well. The goal of reducing critical voltage and maximum rotation angle was achieved in the G2 design but there were unresolved issues with poor performance in the antenna feedline which had to traverse the hinge structure with multiple turns.

The G3 antenna platform was developed to address challenges with integrating an antenna with the steerable platform. The change from generations 2 to 3 was to eliminate one pair of hinges and the intermediate frame. The performance and behavior of the G3 platform was very similar to the G2 platform with one exception. The critical voltage of the G3 platform was slightly higher over previous designs. It had a smaller footprint which reduced the actuation area but could be placed closer to the actuation pad.

A summary of the performance and characteristics of the prototype and generations $1-3$ antenna platforms is shown in Table 5.1.1.

Platform	Prototype Device	Generation 1 Platform	Generation 2 Platform	Generation 3 Platform
Degrees of Freedom	2-D	2-D	2-D	1-D
Mask Layers	4	4	5	5
Actuation Paradigm	Electrostatic	Electrostatic	Electrostatic	Electrostatic
Hinge Thicknesses	30, 50, 80, 100 μm	100 μm	25, 50, 75, 100 μm	20, 40, 60, 80 μm
Hinge Lengths	100 μm	100 – 4000 μm	500, 1000, 1500, 2000 μm	500, 1000, 1500, 2000 μm
Maximum Actuation Angle	0.2 – 4.0° ± 0.2°	NA	2.3 – 13°	2.3 – 13°
Maximum Actuation Voltage	800 V	NA	160 – 3400 V	229 - 4800 V

Table 5.1.1: Summary of Antenna Platform Performance for Designs Investigated

Section 5.2 – Antenna Performance Summary

Electrical and Mechanical optimization of the steerable MEMS antenna were conducted concurrently. For this reason, multiple antennas were simulated on each generation of the antenna platform. The mechanical structure was continually updated and optimized until good electrical performance could be achieved. The G3 platform had the best electrical and mechanical performance.

The teardrop planar inverted cone antenna (Td-PICA) was selected for integration with the antenna platform for its monopole radiation pattern and broadband performance. This antenna was integrated with all three antenna platform designs in a monopole configuration. Due to the available space on the G2 platform, a dipole configuration of the Td-PICA was also studied. Two more antennas were also studied on the G3 platform after it was found to have the best performance upon antenna/platform integration. The cylindrical dielectric resonator antenna

(C-DRA) was selected for its well-known behavior. The teardrop dielectric resonator was a hybrid between the Td-PICA and C-DRA and was studied for two reasons. First the teardrop shape had undergone significant optimization and secondly, to the author's best knowledge, no such antenna has ever been studied.

The G1 platform with the Td-PICA had very poor broadband performance. The G2 platform designs were broadband but operated at frequencies that presented significant challenges. The equipment and technology to build and test antennas at theses frequencies is costly and incompatible with most test systems. These designs also had lobed radiation patterns which made them less suitable for imaging. The antennas on the G3 platform had the best performance with broadband radiation, monopole beam shape, and low frequency operation (< 26.5 GHz). A summary of the antenna performance for all cases examined are summarized in Table 5.2.1.

Antenna	Planar Teardrop	Planar Teardrop	Planar Teardrop	Planar Teardrop	Cylindrical DRA	Teardrop DRA
Platform	G1	G2	G2	G3	G3	G3
Configuration	Monopole	Monopole	Dipole	Monopole	Monopole	Monopole
Lower Cutoff (GHz)	6.37	26.53	29.80	3.15	10.21	13.57
Upper Cutoff (GHz)	6.85	55.95	51.30	12.09	14.58	24.00
Bandwidth	1.07	2.11	1.72	3.84	1.43	1.77
Center Frequency (GHz)	6.61	41.24	40.55	7.62	12.40	18.78
Frequency Range (GHz)	0.48	29.43	21.50	8.94	4.37	10.43
Beam Shape	Isotropic	Lobed	Lobed	Monopole	Monopole	Monopole

Table 5.2.1: Summary of Antenna Performance for Designs Investigated

Section 5.3 – Performance Evaluation

Three antennas were studied on the Generation 3 steerable MEMS platform. This platform had the drawback of only one degree of freedom for rotation but was deemed acceptable for achieving good antenna performance. Since electrical and mechanical optimization was completed concurrently, a final series of studies were undertaken that reflected the knowledge gained from each optimization. The G3 antenna platform had 16 design variations and three different antennas were simulated on each variation.

There was no specific application for this antenna other than for imaging in a very generic sense. For this reason, it was impossible to say in a concrete manner what variation of platform and antenna was 'best'. The design goals were to maximize bandwidth (BW) and fracture angle (AA). The performance of all design iterations in these categories were evaluated and tabulated.

A performance metric was developed to evaluate the value of all the design iterations and denoted as Sum of Normals. The metric was developed to have a perspective on which design was 'best'. The bandwidth and fracture angle were normalized. The best design in each of these categories had a normalized value of 1 with all other iterations having values less than 1. The critical voltage needed to be minimized so iterations' performance was inverted and then normalized. A weighted sum of the three normalized design performance areas were evaluated and normalized so that the best overall design would have a performance metric of 1. The bandwidth and fracture angle were weighted three times higher than the critical voltage because they were more important to the design. A mathematical description of the two performance evaluation metrics are shown below.

$$Sum\ of\ Normals = Norm\left[3 * Norm(BW) + 3 * Norm(FA) + Norm\left(\frac{1}{CV}\right)\right] \quad (5.1)$$

The tabulated performance and key design parameters for the integrated Td-PICA on G3 platform are shown in Table 5.3.1. The return loss of the best case Td-PICA on G3 is shown in Figure 5.3.1.

Iteration Number	Hinge Length (μm)	Hinge Thickness (μm)	Hinge Fracture Angle (°)	Critical Voltage (V)	Lower Cutoff (GHz)	Upper Cutoff (GHz)	Band-width	Center Frequency (GHz)	Frequency Range (GHz)	Sum of Norms
1	500	20	3.2 ± 0.4	229 ± 5	5.31	23.19	4.36	14.25	17.87	0.94
2	1000	20	6.4 ± 0.8	480 ± 10	4.94	18.33	3.71	11.64	13.39	0.90
3	1500	20	9.6 ± 1.3	760 ± 20	4.65	14.95	3.21	9.01	10.22	1.00
4	2000	20	12.9 ± 1.7	1120 ± 30	10.64	12.34	1.16	11.49	1.70	0.79
5	500	40	2.9 ± 0.4	560 ± 10	5.23	22.57	4.32	13.90	17.34	0.81
6	1000	40	5.9 ± 0.8	1160 ± 30	4.88	17.78	3.64	11.33	12.89	0.81
7	1500	40	8.8 ± 1.2	1840 ± 50	4.82	14.47	3.00	9.65	9.65	0.85
8	2000	40	11.8 ± 1.5	2700 ± 100	9.93	12.00	1.21	10.96	2.07	0.73
9	500	60	2.6 ± 0.3	860 ± 20	5.12	22.04	4.30	13.58	16.92	0.76
10	1000	60	5.2 ± 0.7	1770 ± 40	4.91	17.65	3.60	11.28	12.75	0.77
11	1500	60	7.8 ± 1.0	2800 ± 100	5.27	14.42	2.74	9.85	9.15	0.76
12	2000	60	10.4 ± 1.4	2900 ± 100	9.73	11.54	1.19	10.63	1.81	0.67
13	500	80	2.3 ± 0.3	1090 ± 20	5.09	21.33	4.19	13.21	16.24	0.72
14	1000	80	4.6 ± 0.6	2200 ± 100	4.97	17.61	3.54	11.29	12.64	0.70
15	1500	80	6.9 ± 0.9	3400 ± 100	7.19	14.29	1.99	10.74	7.10	0.62
16	2000	80	9.2 ± 1.2	4800 ± 100	9.29	11.89	1.28	10.59	2.61	0.63

Table 5.3.1: Design of Experiments and Results of the Planar Inverted Cone Antenna Integration with the G3 Antenna Platform
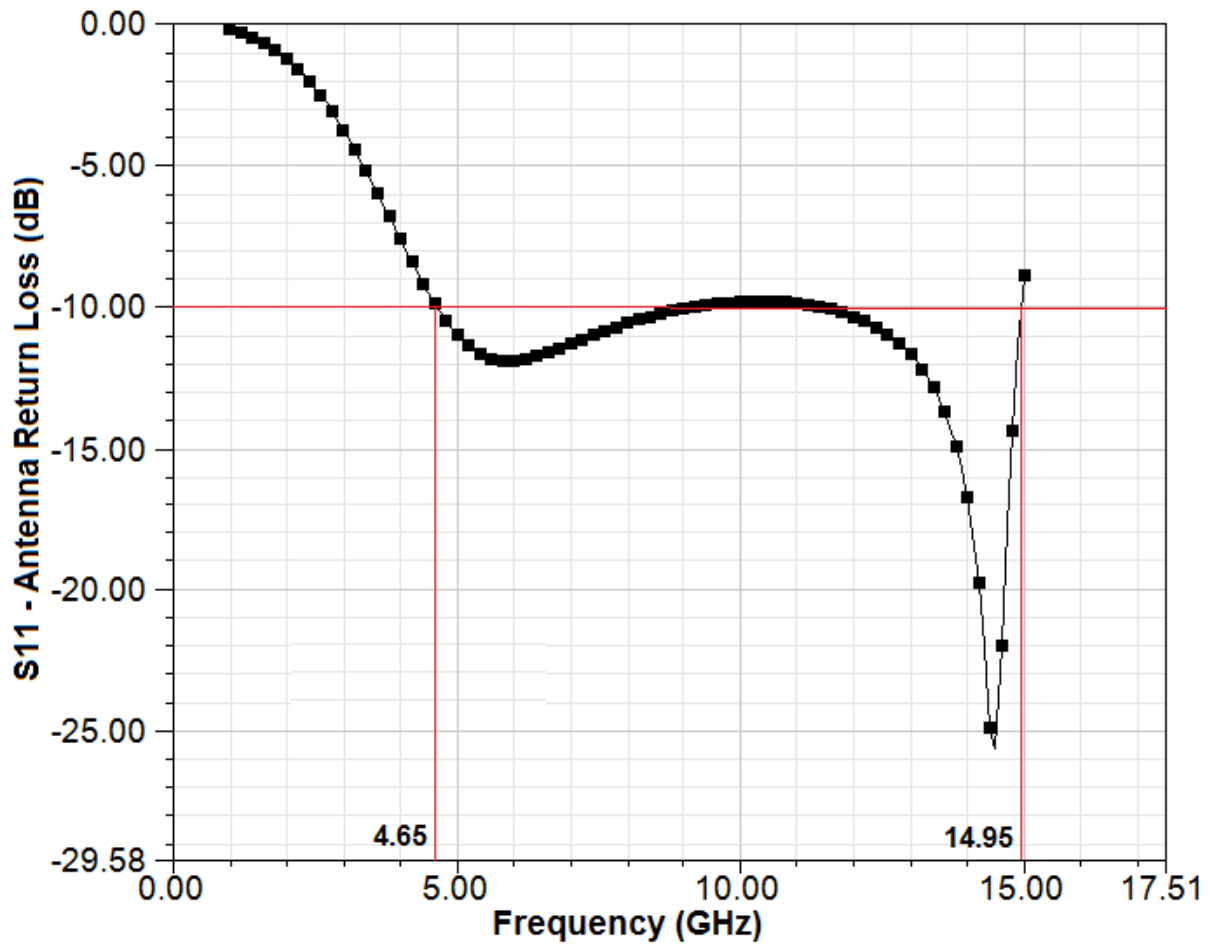
Figure 5.3.1: Return Loss of the Best Case Planar Inverted Cone Antenna Referenced to 100 Ω on the G3 Antenna Platform

The tabulated performance and key design parameters for the integrated C-DRA on G3 platform are shown in Table 5.3.2. The return loss of the best case C-DRA on G3 is shown in Figure 5.3.2.

Iteration Number	Hinge Length (μm)	Hinge Thickness (μm)	Hinge Fracture Angle (°)	Critical Voltage (V)	Lower Cutoff (GHz)	Upper Cutoff (GHz)	Band-width	Center Frequency (GHz)	Frequency Range (GHz)	Sum of Norms
1	500	20	3.2 ± 0.4	229 ± 5	14.75	27.79	1.88	21.27	13.04	0.80
2	1000	20	6.4 ± 0.8	480 ± 10	12.09	21.24	1.76	16.66	9.15	0.81
3	1500	20	9.6 ± 1.3	760 ± 20	10.67	18.33	1.72	14.50	7.66	0.89
4	2000	20	12.9 ± 1.7	1120 ± 30	9.47	16.09	1.70	12.78	6.62	1.00
5	500	40	2.9 ± 0.4	560 ± 10	14.66	25.94	1.77	20.30	11.28	0.66
6	1000	40	5.9 ± 0.8	1160 ± 30	12.37	21.45	1.73	16.91	9.08	0.74
7	1500	40	8.8 ± 1.2	1840 ± 50	10.68	16.88	1.58	13.78	6.20	0.80
8	2000	40	11.8 ± 1.5	2700 ± 100	9.40	15.95	1.70	12.67	6.55	0.94
9	500	60	2.6 ± 0.3	860 ± 20	17.63	21.95	1.25	19.79	4.32	0.49
10	1000	60	5.2 ± 0.7	1770 ± 40	13.53	18.17	1.34	15.85	4.64	0.60
11	1500	60	7.8 ± 1.0	2800 ± 100	11.55	15.62	1.35	13.58	4.07	0.70
12	2000	60	10.4 ± 1.4	2900 ± 100	10.06	13.67	1.36	11.86	3.61	0.80
13	500	80	2.3 ± 0.3	1090 ± 20	17.31	21.53	1.24	19.42	4.22	0.47
14	1000	80	4.6 ± 0.6	2200 ± 100	14.47	17.38	1.20	15.92	2.91	0.51
15	1500	80	6.9 ± 0.9	3400 ± 100	11.87	14.96	1.26	13.41	3.09	0.63
16	2000	80	9.2 ± 1.2	4800 ± 100	10.83	13.14	1.21	11.98	2.32	0.71

Table 5.3.2: Design of Experiments and Results of the Cylindrical Dielectric Resonator Antenna Integration with the G3 Antenna Platform
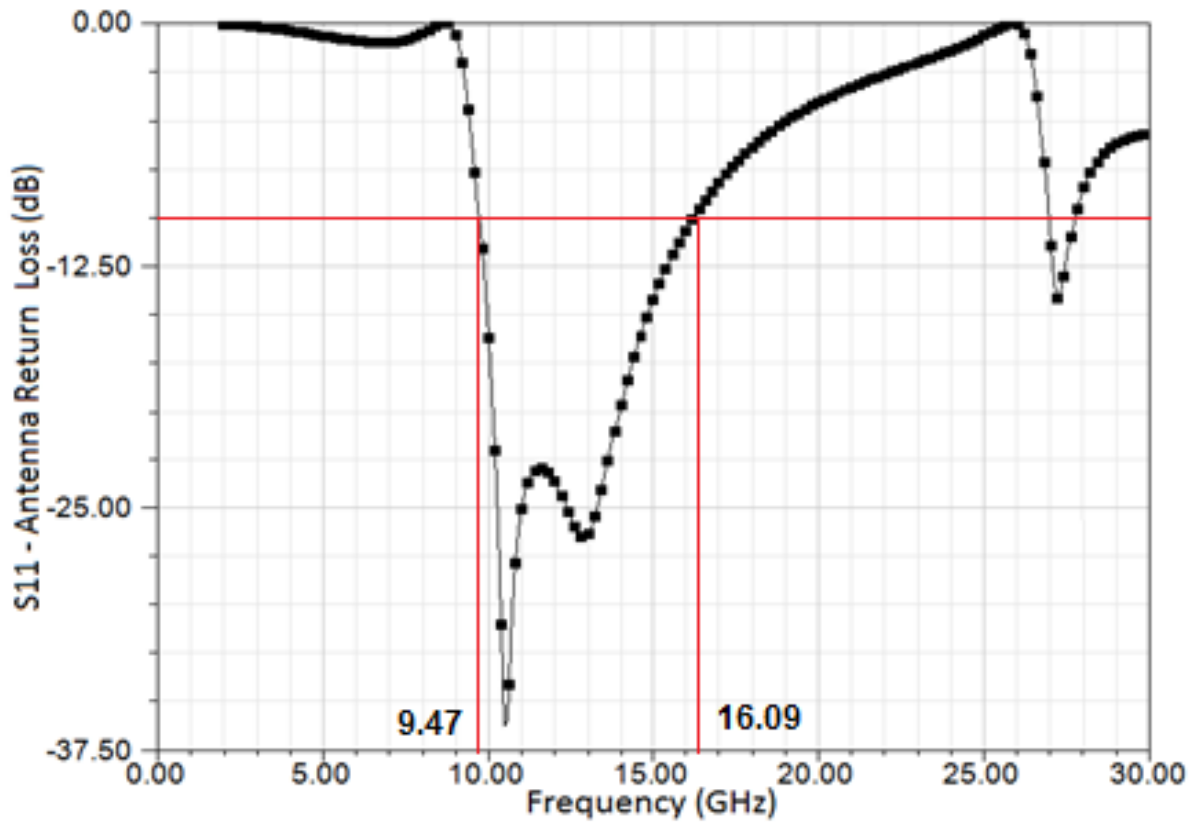
Figure 5.3.2: Return Loss of the Best Cylindrical Dielectric Resonator Antenna Referenced to 100 Ω on the G3 Antenna Platform

The tabulated performance and key design parameters for the integrated Td-DRA on G3 platform are shown in Table 5.3.3. The return loss of the best case Td-DRA on G3 is shown in Figure 5.3.3.

Iteration Number	Hinge Length (μm)	Hinge Thickness (μm)	Hinge Fracture Angle (°)	Critical Voltage (V)	Lower Cutoff (GHz)	Upper Cutoff (GHz)	Band-width	Center Frequency (GHz)	Frequency Range (GHz)	Sum of Norms
1	500	20	3.2 ± 0.4	229 ± 5	26.05	43.68	1.68	34.86	17.63	0.74
2	1000	20	6.4 ± 0.8	480 ± 10	20.85	35.17	1.69	28.01	14.32	0.78
3	1500	20	9.6 ± 1.3	760 ± 20	16.17	29.49	1.82	22.83	13.32	0.91
4	2000	20	12.9 ± 1.7	1120 ± 30	13.76	24.47	1.78	19.12	10.72	1.00
5	500	40	2.9 ± 0.4	560 ± 10	25.57	42.95	1.68	34.26	17.38	0.63
6	1000	40	5.9 ± 0.8	1160 ± 30	19.21	34.28	1.78	26.74	15.07	0.74
7	1500	40	8.8 ± 1.2	1840 ± 50	16.60	27.83	1.68	22.21	11.22	0.81
8	2000	40	11.8 ± 1.5	2700 ± 100	13.65	23.34	1.71	18.50	9.69	0.93
9	500	60	2.6 ± 0.3	860 ± 20	26.33	42.09	1.60	34.21	15.76	0.57
10	1000	60	5.2 ± 0.7	1770 ± 40	19.96	33.44	1.68	26.70	13.48	0.68
11	1500	60	7.8 ± 1.0	2800 ± 100	15.95	27.22	1.71	21.58	11.27	0.78
12	2000	60	10.4 ± 1.4	2900 ± 100	13.68	22.78	1.66	18.23	9.10	0.87
13	500	80	2.3 ± 0.3	1090 ± 20	26.40	41.38	1.57	33.89	14.98	0.55
14	1000	80	4.6 ± 0.6	2200 ± 100	19.39	33.14	1.71	26.26	13.75	0.64
15	1500	80	6.9 ± 0.9	3400 ± 100	15.55	26.69	1.72	21.12	11.14	0.74
16	2000	80	9.2 ± 1.2	4800 ± 100	13.49	22.01	1.63	17.75	8.52	0.81

Table 5.3.3: Design of Experiments and Results of the Teardrop Dielectric Resonator Antenna Integration with the G3 Antenna Platform
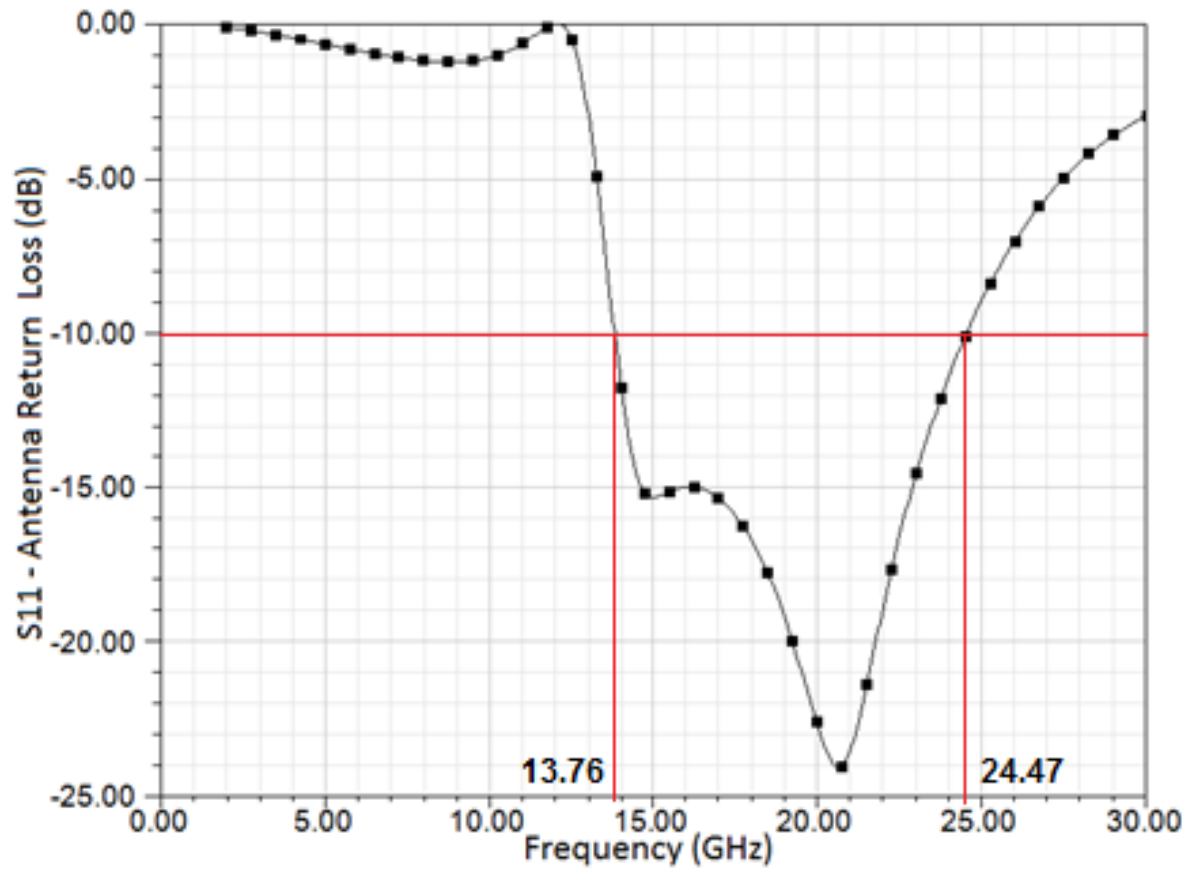
Figure 5.3.3: Return Loss of the Best Teardrop Dielectric Resonator Antenna Referenced to 100 Ω on the G3 Antenna Platform

Section 5.4 – Design Recommendations

The performance of the six steerable MEMS antenna variations presented in this thesis is summarized in Table 5.4.1.

No.	Antenna	Config.	MEMS Platform	Hinge Length (mm)	Hinge Thickness (μm)	Fracture Angle (°)	Critical Voltage (V)	Bandwidth	Center Frequency (GHz)	Max Gain (dB)
1	Planar Teardrop	Monopole	G1	0.9	20	22.5	N/A	1.08 ± 0.01	6.6	- 15
2	Planar Teardrop	Dipole	G2	1.0	20	6.4 ± 0.8	332 ± 1	1.72 ± 0.01	41.5	0
3	Planar Teardrop	Monopole	G2	1.0	20	6.4 ± 0.8	332 ± 1	2.11 ± 0.02	40.5	1
4	Planar Teardrop	Monopole	G3	1.5	20	9.6 ± 1.3	760 ± 20	3.62 ± 0.03	9.01	- 5
5	Cylindrical DRA	Monopole	G3	2.0	20	12.9 ± 1.7	1120 ± 30	1.70 ± 0.02	12.78	- 8
6	Teardrop DRA	Monopole	G3	2.0	20	12.9 ± 1.7	1120 ± 30	1.78 ± 0.01	19.12	- 4 d

Table 5.4.1: Summary of the All Antenna Designs Studied

Section 5.5 – Conclusions and Future Work

In conclusion, six different antenna/platform combinations were simulated. Mechanical and electrical performance was predicted for all variations. Multiple numerical experiments were undertaken to understand system behavior and to optimize device performance. Critical design parameters included hinge thickness and lengths, as well as antenna shape and feedline geometry. The effects of these design considerations have been presented in this thesis. Hinge length was an important factor to maximize within design constraints to achieve a large maximum antenna platform rotation. Hinge thickness was an important factor to reduce the required actuation voltage. One concern was that hinges that could rotate to greater angles will also have higher actuation voltages due to the large actuation pad offset distance. Antenna shape was important to achieve desired performance and should be optimized for integration with the antenna platform, as should the feedline. The work here presents a roadmap for optimizing the steerable MEMS antenna for applications in the future.

Future work to be done on this project would be to fabricate and test devices. The work presented in this thesis was all computational design work so it would be interesting to validate the designs presented herein.

An application for these designs must be identified before they can be optimized any further. The antennas presented herein were designed to have the best performance in a general sense but no design can be optimized until the designer knows exactly how they are to be used.

References

[1] – "Design, Testing, and Fabrication of a Broadband MEMS Antenna", D.A. Hutchings, Dissertation for Partial Fulfillment of the Requirements for Doctor of Philosophy, University of Arkansas, 2010

[2] – "Microsensors, MEMS, and Smart Devices", J.W. Gardner, V.K. Varadan, O.O. Awadelkarim, John Wiley & Sons, Inc 2001

[3] – "MMIC Design", I.D. Robinson, Institution of Electrical Engineers, 1995– ", Micromachined microwave actuator (MIMAC) technology

[4] – "Modern Millimeter-Wave Technologies", T. Teshirogi, T. Yoneyama, Ohmsha Press, 2001

[5] – "RF MEMS: Theory, Design, and Technology", G. M. Rebiez, John Wiley & Sons, Inc 2003

[6] – "A new tuning approach for microwave integrated circuits", L. E. Larson, R. H. Hackett, M. A. Melendes, and R. F. Lohr, Microwave and Millimeter-Wave Monolithic Circuits Symposium Digest, Boston, MA, June 1991, pp. 27–30

[7] – "The State of RF/Microwave Switches", P. Hindle, Microwave Journal, Nov. 2010

[8] – "Inductively-loaded RF MEMS Reconfigurable Filters", V. Sekar, K. Entesari, International Journal of RF and Microwave Computer-Aided Engineering, April, 2009

[9] – "Reconfigurable MEMS Antennas", N. Haridas, A.T. Erdogan, T. Arslan, A.J. Walton, S.Smith, T. Stevenson, C. Dunare, A. Gundlach, J. Terry, P. Argyrakis, K. Tierney, A. Ross, T. O'Hara, NASA/ESA Conference on Adaptive Hardware and Systems, 2008 IEEE, DOI 10.1109/AHS.2008.28

[10] – "Antenna Theory and Design", W.L. Stutzman, G.A. Thiele, John Wiley & Sons, Inc., 1998

[11] – "Antenna Theory: Design and Analysis", C.A. Balanis, John Wiley & Sons, Inc., 2005

[12] – "A large-scale study of the ultrawideband microwave dielectric properties of normal, benign, and malignant breast tissues obtained from cancer surgeries", M. Lazebnik, D. Popovic, L. McCartney, C.B. Watkins, M.J. Ogilvie, A. Magliocco, T.M. Breslin, W. Temple, D. Mew, J.H. Booske, M. Okoniewski, S.C.Hagness, Physics in Medicine and Biology, Vol. 52 (2007) 6093 – 6115

[13] – "Comparison of no-prior and soft-prior regularization in biomedical microwave imaging", A.H. Golnabi, P.M. Meaney, S.D. Geimer, K.D. Paulsen, Journal of Medical Physics, Vol. 36, No. 3, pp. 159 - 170

[14] – "Analysis of Female Human Breast Tissues at Microwave Frequencies", G. Bindu, K.T. Mathew, Microwave and Optical Technology Letters, Vol. 50, No. 3, March 2008

[15] – "Three-Dimensional FDTD Analysis of a Pulsed Microwave Confocal System for Breast Cancer Detection: Design of an Antenna-Array Element", S.C. Hagness, A. Taflove, J.E. Bridges, IEEE Trans. On Antennas and Propagation, Vol. 47, No. 5, May 1999

[16] – "Broadband Dual Linear Polarized Antenna for Statistical Detection of Breast Cancer", D.A. Wooten, M. El-Shenawee, IEEE Trans. On Antennas and Propagation, Vol. 56, No. 11, November 2008

[17] - "Terahertz pulsed spectroscopy of freshly excised human breast cancer", P.C. Ashworth, E. Pickwell-MacPherson, E. Provenzano, E.E. Pinder, A.D. Purushotham, M. Pepper, V.P. Wallace, Optics Express, 20 July, 2009, Vol. 17, No. 15

[18] – "Reconfigurable Scan-Beam Single-Arm Spiral Antenna Integrated With RF-MEMS Switches", C. won Jung, M.-J. Lee, G.P. Li, F. DeFlaviis, IEEE Trans. On Antennas and Propagation, Vol. 54, No.2 February 2006

[19] – "RF MEMS Sequentially Reconfigurable Serpinski Antenna on a Flexible Organic Substrate with Novel DC-Biasing Technique", N. Kingsley, D. Anagnostou, M. Tentzeris, J. Papapolymerou, Journal of Miecroelectromechanical Systems, Vol. 16, No. 5, October 2007

[20] – "A Comprehensive Investigation of New Planar Wideband Antennas", S.-Y. Suh, Dissertation for Partial Fulfillment of the Requirements for Doctor of Philosophy in Electrical and Computer Engineering, Virginia Polytechnic Institute and State University, 2002

[21] – "Fundamentals of Microfabrication", M. Madou, CRC Press, 1997

[22] – https://www.mems-exchange.org/catalog/P3724/, Accessed 9/5/12

[23] – "Review on the Modeling of Electrostatic MEMS", W.-C. Chuang, H.-L. Lee, P.-Z. Chang, Y.-C. Hu, Sensors, 2010, 10, 6149-6171

[24] – "A Methodology and Model for the Pull-In Parameters of Electrostatic Actuators", Y. Nemirovsky, O. Bochobza-Degani, Journal of Microelectromechanical Systems, Vol. 10, No. 4, December, 2001

[25] – "Multi-Directional Dual Comb-Drive Actuator for Optical Applications", W.T. Lin, J.C. Chiou, International Journal of Computational Engineering Science, Vol. 4, No. 2, (2003) 201-204

[26] – "A low-voltage three-axis electromagnetically actuated micromirror for fine alignment among optical devices", I.-J. Cho, E. Yoon, Journal of Micromechanics and Microengineering, 19 (2009), 085007 (8pp)

114

[27] – "Novel Printed Yagi-Uda Antenna With High Gain and Broadband", S. Lin, G.-L. Huang, R.-N. Cai, J.-X. Wang, Progress in Electromagnetics Research Letters, Vol. 20, 107-117, 2011

[28] – http://www.q-par.com/products/spiral-antennas/0.5-18-ghz-spiral-antennas, Accessed 10/2/12

[29] – "Tuning Fractal Antennas and Fractal Resonator", N. Cohen, US Patent # 61042349, August 15, 2000

[30] – "Multiband Triangular Fractal Antennas for Mobile Communications", R.L. Yadava, M. Ram, D. Das, International Journal of Engineering Science and Technology, Vol. 2(11), 2011, 6335-6348

[31] – "On the design of a CPW-fed square octal shaped fractal UWB antenna", IEE Applied Electromagnetics Conference, 2009

[32] – "The Resonant Cylindrical Dielectric Cavity Antenna", S.A. Long, M.W. McAllister, L.C. Shen, IEEE Trans. On Antennas and Propagation, Vol. AP-31, No. 3, May 1983

[33] – "CPW-Fed Dielectric Resonator Antenna for Ultra-Wideband Applications", Z.-B. Weng, X.-M. Wang, Y.-C. Jiao, F.-S. Zhang, Microwave and Technology Letters, Vol. 52, No. 12, December 2010

[34] – "Bandwidth Enhancement Techniques of Dielectric Resonator Antenna", A. Sharma, S.C. Shirvastava, International Journal of Engineering Science and Technology, No.7, Vol. 3, July 2011

[35] – "Micromachined 300-GHz Su-8-Based Slotted Waveguide Antenna", Y. Wang, M. Ke, M.J. Lancaster, J. Chen, IEE Antennas and Wireless Propagation Letters, Vol. 10, 2011

[36] – "Microstrip Lines and Slotlines", K.C. Gupta, R. Garg, I. Bahl, P. Bhartia, Second Edition, Artech House, Inc., 1996

[37] –"Why is (111) silicon a better mechanical material for MEMS" J. Kim, D. Cho, and R. Muller, in Proc. Transducer, Munich, Germany, June 2001, pp. 662–665.

[38] – "State of the Art in 60-GHz Integrated Circuits and Systems for Wireless Communications", T.S. Rappaport, J.N. Murdock, F. Gutierrez, Procedings of the IEEE, Vol. 99, No. 8, August 2011

[39] – "A 60-GHz Millimeter-Wave CPW-Fed Yagi Antenna Fabricated by Using 0.18-µm CMOS Technology", S.-S. Hsu, K.-C. Wei, C.-Y. Hsu, H. Ru-Chuang, IEEE Electron Device Letters, Vol. 29, No. 6, June 2008

[40] – "On-Chi Antennas for 60-GHz Radios in Silicon Technology", Y.P.Zhang, M. Sun, L.H. Guo, IEEE Transactions on Electron Devices,Vol. 52, No. 7, July 2005

[41] – "The Reflectarray Antenna" D. Berry, R. Malech, W. Kennedy, IEEE Transactions on Antenna Propagation 1963; Vol. 11, No, 6, pp. 645-651.

[42] – "Perforated Dielectric Resonator Antenna Reflectarray", S.H. Zainud-Deen, S.M. Gaber, A.M. Abd-Elhady, K.H. Awadalla, A.A. Kishk, ACES Journal, Vol. 26, No. 10, October 2011

[43] – "Terahertz antenna based on Graphene", M. Dragoman, A.A. Muller, D. Dragoman, F. Coccetti, R. Plana, Journal of Applied Physics 107, 104313 (2010)

[44] – "Novel Sheer Strength Evaluation of MEMS Materials Using Asymmetrical Four-Point Bending Technique", M. Ogawa, Y. Isono, 20th IEEE International Conference on MEMS, Kobe, Japan, January 2007

Appendix A: Description of Research for Popular Publication

How Supercomputers Help Engineers Design in the 21st Century

The 21st century brings an incredible array of tools for today's modern engineer. The computer has evolved from a novelty to a powerful problem solving tool with nearly limitless design capabilities. Many major technology companies such as Boeing, Lockheed Martin and Intel rely on sophisticated computer models and software to develop their products. Open source design software has allowed amateur designers to get in on the action as well.

Morgan Roddy, a graduate student at the University of Arkansas, working with Dr. Magda El-Shenawee, has been working on designing a special type of antenna with advanced simulation tools and techniques. The antenna is known as a 'Steerable MEMS Antenna'. 'Steerable' refers to the fact that the antenna can rotate which allows for its radiation to be 'steered'. 'MEMS' is an acronym that stands for Micro-ElectroMechanical Systems. Generally speaking, MEMS are machines built on computer chips and are fabricated using very sophisticated equipment and process originally developed to make integrated circuits and adapted for broader use. 'Antenna' means that the device is used to transmit and receive electromagnetic radiation.

The antenna is very special and took a massive amount of computational power to design; enter supercomputer. The antenna is special for several reasons. First, it is broadband which means it can work over a wide range of frequencies. This is important for having a versatile antenna that could have applications in communications or imaging. Second, the antenna is mounted a platform that with hinges so that it can rotate. By rotating the antenna, it is possible to change the direction it radiates without moving the antenna or having to use sophisticated equipment and techniques. Lastly, the antenna is special because it and its hinges are all built into the same computer chip. That's right; the hinges, antenna, and platform are made by 'micro-machining' a single silicon chip. This is very useful for reducing manufacturing costs as well as system complexity.

If this antenna sounds complicated, this is because it is in fact very complicated. To design such an antenna requires studying the mechanical behavior (how it moves) in conjunction with the electrical behavior (how it radiates and at what frequencies). The mechanical design has a major effect on electrical performance and electrical design has an effect on mechanical performance. Furthermore, the methods used to fabricate the antenna can also have a significant impact on its performance. For this reason, the device had to be studied and optimized with sophisticated computer models that were run on supercomputers. This approach is called computational design and is a very powerful technique to solve complex engineering problems.

The antenna was first developed to take measurements of biological tissues. The results of the measurements can be fed into a computer algorithm that is run on a supercomputer. The results of this technique are stunning. It is possible with this approach to detect cancerous tumors and map their shape, size and location without every performing a surgery or biopsy. Furthermore, the radiation from the antenna is harmless in contrast with traditional X-rays and

mammograms and has much clearer results. This process is known as statistical detection of cancer.

In the future, the antenna developed could be used to build affordable systems to detect and map cancerous tissues for intraoperative use. Today medicine is benefitting from technology originally developed for radar and communication in an unlikely but very valuable way. It is exciting how computers are being used the 21st century to further other technologies. Furthermore, technology originally developed for national defense is now being applied to more humanitarian problems. The coming decades will certainly continue to see tools like supercomputers being used to help solve society's biggest threats such as cancer.

Appendix B: Executive Summary of Newly Created Intellectual Property

The intellectual property generated in the writing of this thesis includes two novel antennas, the predicted performance of 16 variations of three different antennas, and a broadband planar antenna shape. The two novel antennas presented in this thesis are to the best of this author's knowledge are unique; the Cylindrical DRA and the Teardrop DRA, both on the G3 platform. In literature there are currently no examples of a steerable MEMS DRA, or a teardrop shaped DRA. The cylindrical DRA is only novel because of the platform it is placed on. The teardrop DRA is unique because nobody has ever made a DRA in this shape or on such a platform. These two antennas represent the most novel elements of this thesis. The predictions in the 16 variations include bandwidth, hinge fracture angle, and maximum actuation voltage at pull-in/fracture. These predictions are made for the three antennas on the G3 platform. A summary of the Intellectual property generated in this thesis is shown below.

1. The Optimized Teardrop Planar Inverted Cone Antenna

2. Teardrop Shaped Dielectric Resonator Antenna

3. Steerable MEMS Dielectric Resonator Antenna

4. Predicted performance of 16 Variations of the Teardrop Planar Inverted Cone Antenna on the G3 Steerable MEMS Platform

5. Predicted performance of 16 Variations of the Cylindrical Dielectric Resonator Antenna on the G3 Steerable MEMS Platform

6. Predicted performance of 16 Variations of the Teardrop Dielectric Resonator Antenna on the G3 Steerable MEMS Platform

Appendix C: Potential Patent and Commercialization Aspects of listed IP Items

The designs presented in this thesis show significant promise for application due to the design's versatility. However, the device was optimized without a specific application in mind. For this reason, the device is not yet ready for commercialization. Not until a specific application is selected can the antenna be truly finished.

C.1 Patentability of Intellectual Property

1. The Optimized Teardrop Planar Inverted Cone Antenna

The optimized antenna shape is based on a design that was first presented by [20]. The difference between the variation in this thesis and the original is how the antenna is fed and the width of the shape. [20] claimed that the antenna could be scaled in different ways to modify its performance. That is what this author did to achieve the broadband antenna shape used throughout this thesis. For this reason it could be argued that the teardrop antenna shape is an obvious variation of a previously presented design. This design could possibly be patented but would be unlikely to support broad claims about the shape.

2. Teardrop Shaped Dielectric Resonator Antenna

There are very few examples of dielectric resonator antennas in literature that are not shaped like rectangles, cylinders, and hemispheres. To the best of this author's knowledge, there has not been a teardrop shaped DRA or any organic shaped DRAs reported in literature. The shape is the same as the optimized Td-PICA and so its profile is based on [20]. However, [20] never claimed that the shape could be used for a DRA. It was the author of this thesis who came up with a teardrop shaped DRA. The Td-PICA was used because it was already optimized for the feedline and substrate material. This design could possibly be patented but would be unlikely to support broad claims about the shape.

3. MEMS Dielectric Resonator Antenna

To the best of this author's knowledge, there are no examples of MEMS dielectric resonator antennas. The DRA is very interesting because it can operate at very high frequencies due to low losses. Designs can scale to higher frequencies much more easily when MEMS fabrication is used. It is very simple to scale designs for MEMS devices while it is significantly more challenging to do with conventional antennas. The fact that the design is steerable adds to the novelty of the design as well. It is of the opinion of this author that this design could be patented.

4. Predicted performance of 16 Variations of the Teardrop Planar Inverted Cone Antenna on the G3 Steerable MEMS Platform

While the design predictions are intellectual property, they are not patentable by this author because too much of the design is based on the work of [1].

5. Predicted performance of 16 Variations of the Cylindrical Dielectric Resonator Antenna on the G3 Steerable MEMS Platform

While the design predictions are intellectual property, they are not patentable by this author because too much of the design is based on the work of [1].

6. Predicted performance of 16 Variations of the Teardrop Dielectric Resonator Antenna on the G3 Steerable MEMS Platform

While the design predictions are intellectual property, they are not patentable by this author because too much of the design is based on the work a previous author [1].

C.2 Commercialization Prospects

There were three aspects of the intellectual property generated in this thesis that could possibly be patented: the optimized teardrop shape, the teardrop shaped DRA and the MEMS DRA antenna.

1. Optimized Teardrop Shape

This shape is too specific to be able to make broad claims on a patent application. This makes it difficult to prevent others from tweaking the design to make it sufficiently different. For this reason, the optimized teardrop shape should not be patented.

2. Teardrop Shaped DRA

The teardrop shaped DRA is an interesting variation on a well-known kind of antenna, the DRA. The use of a novel shape is uncommon and the teardrop has never been used. However, this shape is too specific to be able to make broad claims on a patent application so this design however will not be considered for patent submission.

3. MEMS DRA

The MEMS DRA is interesting because of its scalable nature. Scaling metal antennas very small will result in high losses that will render the antenna useless. Scaling DRAs is easily accomplished with MEMS technology and has low losses at high frequencies. This design however will not be considered for patent submission because the integration is not novel.

C.3 Possible Prior Disclosure of IP

The original design set forth by [1] (Dr. Douglas Hutchings) was presented at the IEEE Antenna and Propagation Symposium in San Diego, CA, in July of 2008. His dissertation was published for conferment of his degree in 2009.

Appendix D: Broader Impact of Research

The broader impact of the research presented in this thesis is to broaden the field of microwave detection and of broadband antennas. The antenna that sparked this work had the goal of breast cancer detection but this research's application was generalized to be microwave imaging in general. A fundamental property of the steerable MEMS antenna is that it can be scaled to operate at a very wide range of frequencies. Different frequency ranges are useful in detection based on the target. Microwaves work well for breast cancer detection while explosives detection is achieved with terahertz radiation. The design presented is a versatile design that can be used for a very broad range of applications which makes it unique.

D.1 Applicability of Research Methods to Other Problems

The research method used in this thesis was computational design. This technique can be applied to virtually every field of engineering and design. The trick is to build models so that they yield valuable predictive design results. This can be described as 'virtual prototyping'. The usefulness of predicted performance from this approach is merely based on the sophistication and resolution of the model used. Commercial design software packages are particularly useful but are not necessary. The majority of the mechanical optimization and studies were undertaken with a spreadsheet program. Free software such as Java or C++ can also be used to do computational design. The author of this thesis believes the methods used in this thesis should be studied and understood by more engineers because of the breadth of its usefulness.

**D.2 Impact of Research Results on U.S. and Global Society**

The results of this work could have an impact on society if an application arises that could greatly benefit from a scalable broadband MEMS antenna. Further work is needed to

develop the designs presented in this thesis before commercialization or an impact can be made by these designs.

D.3 Impact of Research Results on the Environment

The results of this work are very unlikely to have any negative impact on the environment. The designs could possibly have a positive effect on the environment if the right application is developed.

Appendix E: Microsoft Project for MS MicroEP Degree Plan
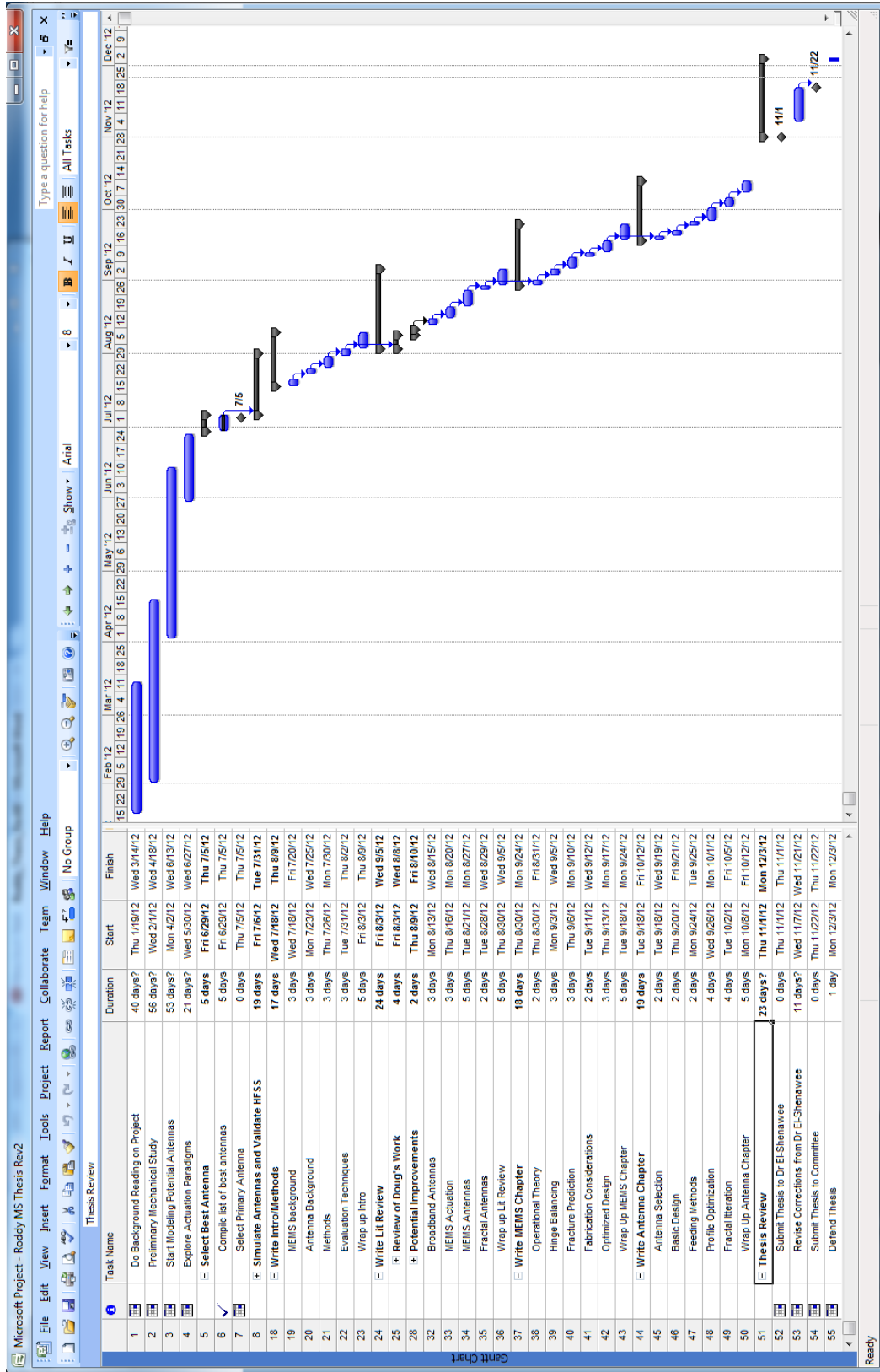
Appendix F: Identification of Software Used in Research and Thesis Generation

Computer #1:
        Model Number: Custom Desktop Computer built by ELEG Technicians
                Intel Core i5-2500 CPU
                Widows 7 Enterprise
        Serial Number: NA
        Location: ENRC 4906, 700 Research Blvd, Fayetteville, AR 72701
        Owner: University of Arkansas: Purchased and supervised by Dr. Magda El-Shenawee
Software #1:
        Name: Microsoft Office 2010
        Purchased by: University of Arkansas: Electrical Engineering Department
Software #2:
        Name: MATLAB R2011b
        Purchased by: University of Arkansas: Electrical Engineering Department
Software #3:
        Name: Adobe Acrobat Professional 10.0
        Purchased by: University of Arkansas Site License
Software #4:
        Name: Ansys High Frequency Selective Surfaces
        Purchased by: University of Arkansas: Dr. Magda El-Shenawee

Computer #2:
        Model Number: Dell Precision T5500
        Service Tag: DKW2BP1
        Location: PHYS 119
        Owner: University of Arkansas: Purchased and supervised by Dr. Jaili Li
Software #1:
        Name: COMSOL Multiphysics Version 4.2.0.150
        Purchased by: UA Microelectronics and Photonics Graduate Program and Dr. Jaili Li
        License #: 1033312

Computer #3:
        Model Number: Sun Ultra 40 Workstation
        Serial Number: SN0649FH100E
        Location: ENRC 4906, 700 Research Blvd, Fayetteville, AR 72701
        Owner: University of Arkansas: Purchased and supervised by Dr. Magda El-Shenawee
Software #4:
        Name: Ansys High Frequency Selective Surfaces
        Purchased by: University of Arkansas: Dr. Magda El-Shenawee

Computer #4:
    Model Number: Dell Latitude E5510
    Serial Number: 9707025205
    Location: 423 W Louise St, Fayetteville, AR 72701
    Owner: Morgan Roddy
Software #1:
    Name: Microsoft Office Suite 2007
    Purchased by: Morgan Roddy

Appendix G: All Publications Published, Submitted and Planned

A 4 page paper has been submitted to the 2013 Applied Computational Electromagnetics Society (ACES) Conference in Monterey, CA. The three different antennas on the Generation 3 antenna platform will be presented as well as an overview of their development and optimization.